

# Sheffield Hallam University

*Finite element modelling and image reconstruction in single and multi-frequency electrical impedance tomography.*

ABADI, Hamid Dehghani Mohammad.

Available from the Sheffield Hallam University Research Archive (SHURA) at:

<http://shura.shu.ac.uk/19182/>

## A Sheffield Hallam University thesis

This thesis is protected by copyright which belongs to the author.

The content must not be changed in any way or sold commercially in any format or medium without the formal permission of the author.

When referring to this work, full bibliographic details including the author, title, awarding institution and date of the thesis must be given.

Please visit <http://shura.shu.ac.uk/19182/> and <http://shura.shu.ac.uk/information.html> for further details about copyright and re-use permissions.

CITY CAMPUS, FORD STREET,  
SHEFFIELD, S1 1WB.

TELEPEN

100364212 8



**REFERENCE**

ProQuest Number: 10694062

All rights reserved

INFORMATION TO ALL USERS

The quality of this reproduction is dependent upon the quality of the copy submitted.

In the unlikely event that the author did not send a complete manuscript and there are missing pages, these will be noted. Also, if material had to be removed, a note will indicate the deletion.



ProQuest 10694062

Published by ProQuest LLC (2017). Copyright of the Dissertation is held by the Author.

All rights reserved.

This work is protected against unauthorized copying under Title 17, United States Code  
Microform Edition © ProQuest LLC.

ProQuest LLC.  
789 East Eisenhower Parkway  
P.O. Box 1346  
Ann Arbor, MI 48106 – 1346

**FINITE ELEMENT MODELLING AND IMAGE  
RECONSTRUCTION IN SINGLE AND MULTI-  
FREQUENCY ELECTRICAL IMPEDANCE  
TOMOGRAPHY**

**Hamid Dehghani Mohammad Abadi**

**B.Sc. (Hons), M.Sc.**

**A thesis submitted in partial fulfilment of the  
requirements of  
Sheffield Hallam University  
for the degree of Doctor of Philosophy**

**December 1998**



## Abstract

Electrical impedance tomography (EIT) is an imaging technique that aims to reconstruct the internal conductivity distribution of a body, based on the electrical measurements taken on its periphery. While relatively new it has received attention as a possible new medical imaging technique which offers non-hazardous applications and low-cost instrumentation.

To understand the full potential of this new mode of imaging, a numerical modelling method has been used in order to investigate the behaviour of an EIT system. Using this mode of analysis, it is possible to simulate many experiments that otherwise physically would be very time consuming and expensive. Such investigation will include the effect and quantification of various physical conditions which have effects on the obtained boundary voltages of an EIT system.

An aim of EIT is the ability to reconstruct accurate images of internal conductivity distributions from the measured boundary voltages. Image reconstruction in EIT using the sensitivity algorithm is generally based on the assumption that the initial conductivity distribution of the body being imaged is uniform. The technique of image reconstruction using the sensitivity algorithm is described and reconstructed images are presented. Improvements in image quality and accuracy are demonstrated when accurate *a-priori* 'anatomical' information, in the form of a model of the distribution of conductivity within the region to be imaged, are used. In practice correct *a-priori* information is not available, for example, the conductivity values within the various anatomical regions will not be known. An iterative algorithm is presented which allows the conductivity parameters of the *a-priori* model to be calculated during image reconstruction.

Multi-frequency EIT is a modified approach of the single frequency method by which tissue characterisation has been proposed by imaging the internal conductivity of region over a range of frequencies. However, due to instrumentation drawbacks, only the real parts of the boundary voltages are presently measured. These real only voltages have so

far (in practice) been used to reconstruct images of the changes in internal conductivity of a region with frequency. The penalty for ignoring the imaginary parts of the data are presented and results obtained show that to accurately image the internal conductivity of a region, not only complex data are needed, but also some *a-priori* information about the region may be necessary.

## Acknowledgements

I would like to express my enormous thanks to my supervisors, Dr. Ivan Basarab and Professor David Barber each for their support and advise throughout the duration of this project as well as the constant enthusiasm and driving force.

Secondly, I would like to thank my family and friends for their support and encouragement, in particular those whose unceasing love continued throughout.

Thirdly, I would like to thank the following researchers and staff at the School of Engineering, Sheffield Hallam University for their help, useful discussions and advise during numerous occasions: Professor Robert Green, Dr. Ken Dutton, Stuart Birchall, Jasbir Takhar and Marshall Booth. In particular I would like to express my gratitude to Dr. Peter Metherall of Department of Medical Physics and Clinical Engineering, University of Sheffield for his helpful and useful advise during the project and also in preparation of this thesis.

Finally, I would like to mention the University of Sheffield and Sheffield Hallam University joint studentship program, without which this research project would not have been possible.

# Contents

Abstract	i
Acknowledgements	iii
Contents	iv
Glossary	vii

## Chapter 1

1. Introduction	1
1.1 Medical imaging techniques	1
1.1.1 X-ray	1
1.1.2 Computerised Tomography CT	2
1.1.3 Gamma Camera	3
1.1.4 Ultrasound	4
1.1.5 Magnetic resonance imaging (MRI)	4
1.1.6 Summary of other medical imaging techniques	6
1.2 Electrical impedance tomography	6
1.2.1 The forward problem	7
1.3 Application of EIT in medicine	8
1.3.1 Pulmonary ventilation	8
1.3.2 Swallowing disorders	9
1.3.3 Stomach emptying	9
1.3.4 Perfusion changes	10
1.3.5 Monitoring hypothermia	10
1.3.6 Breast cancer screening	11
1.4 Electrical properties of biological tissue	11
1.5 Electrical model of physiological tissue impedance	12
1.6 Forward numerical modelling	13
1.7 Problems encountered in EIT	16
1.8 Aims and objectives	17
1.9 Chapter description	19

## Chapter 2

2. The solution of the forward problem	20
2.1 Introduction	20
2.2 The forward problem	21
2.3 The computational forward problem	22
2.4 Finite element analysis	25
2.4.1 Modelling stages in finite elements	27
2.4.2 Finite element software for Electromagnetic simulation	29
2.4.2.1 ELEKTRA by Vector Fields	29
2.4.2.2 Maxwell 2D Simulator by Ansoft	30
2.4.2.3 Maxwell 3D Eddy Current Field Simulator by Ansoft	31
2.4.2.4 Electromagnetic solver by Ansys	31
2.4.2.5 Three dimensional Electromagnetic Analysis by MEGA	32

**Chapter 3**

3. Modelling of the forward problem	33
3.1 Introduction	33
3.2 Modelling method and model construction	33
3.3 The 3D model	41
3.4 Discussions of model construction	42
3.5 Measures of performance	42
3.5.1 Introduction	42
3.5.2 Visibility	44
3.5.2.1 Frequency and permeability	50
3.5.2.2 Frequency and permittivity	53
3.5.2.3 Discussions of effects of visibility with frequency	56
3.5.3 Visibility and electrode width	57
3.5.3.1 Discussion	61
3.6 Visibility in a 3D model	61
3.7 Conclusions	62

**Chapter 4**

4. Single frequency EIT image reconstruction	64
4.1 Introduction	64
4.2 Theory	64
4.3 Single-step image reconstruction algorithms	65
4.3.1 Backprojection between equipotential lines	66
4.3.2 Sensitivity matrix method	66
4.3.3 Iterative image reconstruction algorithms	67
4.4 Image reconstruction using the sensitivity matrix	68
4.4.1 Discussions and conclusions	82
4.5 The calculation of conductivity using the reduced sensitivity matrix	83
4.5.1 Introduction	83
4.5.2 Method	83
4.5.3 Results	88
4.5.4 Discussion	89
4.6 Incorporation of a-priori information into image reconstruction	90
4.6.1 Introduction	90
4.6.2 Method	92
4.6.3 An iterative algorithm based on the sensitivity matrix	102
4.6.4 Discussion	107
4.6.5 Conclusion	108

**Chapter 5**

5. Multi-frequency EIT image reconstruction	110
5.1 Introduction	110
5.2 Method	112
5.2.1 Complex sensitivity matrix	113

5.2.2 Reconstructed images of complex conductivity	115
5.3 Frequency dependence of the complex sensitivity matrix	120
5.4 Complex boundary voltages: Importance of the imaginary part	123
5.4.1 Discussion	134
5.5 Image reconstructed and Cole-Cole model	134
5.5.1 Method	135
5.6 Conclusions	138

## **Chapter 6**

6. Conclusions	140
6.1 Introduction	140
6.2 Summary of key results	140
6.3 Suggestions for further developments	142
6.4 Conclusions	143

## **Appendix A**

A1. Full 3D electromagnetic field eddy current problem	144
A2. Electric scalar formulation with no eddy currents	145

## **Appendix B**

B1. Finite element modelling using MEGA: A brief guide	147
--	-----

## **Appendix C**

C1. List of Matlab files	154
--------------------------	-----

## **References**

References	166
------------	-----

## Glossary

Permittive	A relative electrical permittivity which is greater than 1.
Permeable	A relative magnetic permeability which is greater than 1.
Reciprocal conductivity	A conductivity that is given by $\sigma_{new} = \frac{1}{\sigma_{old}}$ , where $\sigma_{new}$ is the new conductivity and $\sigma_{old}$ is the original conductivity.

# Chapter 1

## 1. Introduction

### 1.1 Medical Imaging techniques

Electrical impedance tomography (EIT) is an imaging technique which enables the internal conductivity distribution within a region to be calculated on the basis of electrical measurements taken on the region's periphery. This imaging method has the great advantage of being non-invasive, inexpensive and free of the radiation hazards encountered with X-rays. It therefore has received attention in the field of medical imaging.

Several medical imaging techniques have been introduced and implemented over the last century. In medical imaging the aim is to obtain images that provide information about the internal anatomical or physiological condition of the region under investigation. Non-invasive methods are preferred over invasive imaging methods, which allow long-term monitoring of the patient as they present less risk. Of the many methods currently used in medicine, a few are discussed here.

#### 1.1.1 X-ray

This is the most common imaging technique in medicine. Photographic films are placed behind the body which will darken with intensity dependent on the amount of X-rays getting through from the source on the other side of the body. X-rays travel in a straight line; X-rays are said to be hard field since they will travel in a straight line independent of the medium they propagate through. The principle interactions causing attenuation of the X-rays are absorption and scattering. The primary photons absorbed by the photographic film form the final image. Most of the scattered photons are removed by the use of anti-scattering devices, which are placed between the patient and the photographic films. This anti-scatter device can simply be a grid formed from a series of parallel lead strips, which will transmit most of the primary radiation, but reject majority of the scatter.

X-rays travelling through the bones produce less darkening on the film because they are attenuated more by the bones, which have a higher attenuation factor than soft tissue. X-rays travelling through soft tissues are attenuated less and produce more darkening of the film. This contrast therefore makes this imaging technique very suitable for imaging and detecting broken bones.

The radiation energy range used in practice is typically 17 - 150 keV, with higher energies used to image thicker body sections. Also the amount of radiation used is a trade-off between suitable radiation dose and achievable image contrast. X-rays images have the advantage of having a good spatial resolution. However X-rays are hazardous and cause damage to tissues.

### **1.1.2 Computerised Tomography CT**

A problem with conventional X-ray imaging is the loss of depth information: a three-dimensional section of the body is collapsed into a two-dimensional image. With CT a two-dimensional planar slice of the body is defined and X-rays are passed through in all directions within that plane and detected on the other side. The transmitted X-rays encounter no part of the body outside the defined plane, and therefore no depth (out of plane) information is seen. CT images are as though a thin slice of the body has been removed and a conventional X-ray has been used to image the slice.

Using a rotating fan beam X-ray source with a continuous ring of detectors, X-rays are projected through the defined plane of the body at many angles and are detected by an array of receivers (about 1000 detectors in total), Figure 1.1. A two dimensional image of a plane can be reconstructed from the detection of these attenuated beams of X-rays.

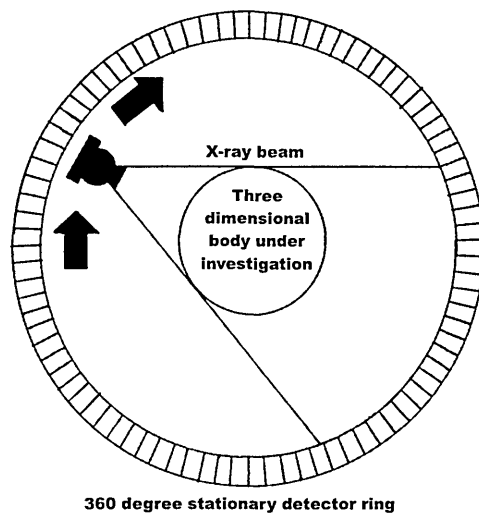


**Figure 1.1 Schematic representation of a CT scanner.**

Since its introduction in 1970s, several new improved generations have been developed. Scanning time has over the years improved from 4 - 5 minutes to 4 - 5 seconds. The reduced scanning time greatly reduced motion blur, since for example, the patient can hold his/her breath for a few seconds. More recently a new generation system is capable of acquiring data in no longer than a few milliseconds which makes this new mode of CT system very useful for cardiac imaging.

The reconstructed image has good spatial resolution but once again X-rays are damaging to biological tissues and also the imaging instrument is large and expensive.

### **1.1.3 Gamma Camera**

Medical imaging using a Gamma camera is based upon the detection of decaying radionuclides. Radiopharmaceuticals such as radioactive iodine are injected into the body as tracers and will be concentrated in the target organ (thyroid gland). As the radiopharmaceutical undergoes radioactive decay, it emits gamma-rays which are detected by scintillation crystals. These yield two-dimensional images of the concentration of the radiopharmaceuticals. Dosage is kept to a minimum amount to minimise damage to tissue and cells.

Gamma cameras are most routinely used for two-dimensional planar imaging, but they can also be used for tomographic reconstruction by rotating the gamma camera around the body over the region of interest. More recently positron emission tomography (PET)

has been developed, which makes use of isotopes where two gamma-rays (of 511 keV each) are emitted simultaneously when the radionuclide annihilates in the tissue.

By the right choice of radiopharmaceuticals, physiological images such as blood flow, blood volume as well as various metabolic processes are possible. Also other typical uses include the diagnosis and localisation of brain tumours, localisation of dead tissue as a result of strokes due to blood clots within the arteries and the monitoring of blood flow changes associated with local brain functions.

#### **1.1.4 Ultrasound**

A transducer is used to send ultrasonic waves of 1-15 MHz into the body. The transmitted waves are reflected by structures within the body and detected at the surface (usually using the same transducer) and the delay in the echoes of the ultrasound waves are used to reconstruct images of internal organ distribution.

The transducer which converts electrical signals to ultrasonic waves and the reflected waves to electrical signals is made of one or more piezo-electric crystals. In the area of transducer contact with the body a medium matching gel is used to ensure good transmission of waves.

Doppler frequency shift can also be used to investigate blood flow within arteries and veins. Moving red blood cells cause a Doppler shift in the reflected wave frequency and the degree and direction of this shift is proportional to the velocity of the red blood cells.

There are widespread clinical uses of diagnostic ultrasound and these mostly include abdominal imaging and in particular monitoring the unborn foetus. Ultrasound is considered to be of very low risk provided the applied intensity and frequencies are sufficiently low.

#### **1.1.5 Magnetic resonance imaging (MRI)**

MRI is concerned with the imaging the distribution of the hydrogen atom in the water within tissues. The patient is placed in a strong magnetic field (1.5 - 3 Tesla) and the response of a transmitted radio wave by the hydrogen atoms are measured and imaged.

A hydrogen atom in a medium placed within a strong magnetic field realigns its axis of rotation with the axis of the magnetic field it is under. The effect is to produce a resultant nuclear magnetisation along the direction of the applied field. This small nuclear magnetic field can be interrupted by applying a pulsed magnetic field perpendicular to the original field. This changes the direction of the nuclear magnetism through an angle dependent on the length of the applied pulse. Following the applied pulse, the interrupted nuclear magnetism slowly again realigns itself with the surrounding magnetic field. During this realignment period, energy is radiated from the nuclei in the form of radio waves of very high frequency. It is these signals that are detected from each small volumes of the body and used to form images.

The perpendicular magnetisation pulse is actually produced by applying radiofrequency (RF) to a coil. In fact the applied RF pulse is chosen so that it is equal to the frequency of the nuclei that are to be stimulated, so that resonant absorption of the RF pulse occurs. During the period following excitation the magnetic resonance signal decays with a time constant characteristic of the precise form of medium containing the nuclei. During this period the relaxation is characterised by two time constants  $T_1$  and  $T_2$ .  $T_1$  is the time constant representing restoration of the bulk magnetisation of a given pixel to its equilibrium state aligned with the axis of the applied field. This is also referred to as longitudinal relaxation time or the spin-lattice decay constant.  $T_2$  is usually faster than  $T_1$  and is due to a loss in phase coherence between neighbouring nuclei, caused by local variation in the magnetic field.

Spatially resolved anatomical data sets are acquired by applying magnetic field gradients across the body being imaged, resulting in measurable gradients in the resonant frequency of the nuclide. Two-dimensional Fourier transformation yields a slice image of the plane of interest.

Instrumentation is very large and very expensive. There is no reported harm to tissue and the produced image has excellent spatial resolution. MRI can be used for the non-invasive diagnosis and treatment planning of a wide range of diseases, including cancer.

### **1.1.6 Summary of other medical imaging techniques**

The medical imaging techniques described above have all been successfully implemented in clinical use. While three of the techniques mentioned here are hazardous and most require expensive instrumentation there is a strong need in medicine for a fast, reliable, non-hazardous and inexpensive imaging technique that can provide information about the internal structure and physiological state of tissue being imaged. It has been because of this need that electrical impedance tomography has been developed as a possibility for fulfilling such requirements.

### **1.2 Electrical impedance tomography**

The technique of electrical impedance tomography (EIT) has been developing for some years (Brown and Barber 1987). Electrodes are positioned with usually equal spacing around the body to be imaged thus defining a plane through a region within that body. A known constant current is injected into the region under investigation through a (drive) electrode pair. The resulting boundary voltages are measured as the differential voltages between two non-current carrying (receive) electrodes. Current flow through a region is a function of the conductivity distribution within that region. As well as the in-plane conductivity distribution, the off-plane conductivity distribution can effect the path of the conduction current. The driven current is therefore not confined to two-dimension (2D). However most images are reconstructed as if the data were from a 2D object as computational and instrumentation complexities involved with three-dimensional (3D) imaging is much greater than 2D.

Commonly 16 electrodes are placed around a region but the maximum number of possible electrodes depends on a number of factors which include the geometry of the body, electrode size, electrode pair configuration as well as the acceptable level of measurement signal to noise ratio. In the arrangement used by most workers, current is driven into the region through two adjacent (drive) electrodes. For each of the 16 drive-electrode pairs, 13 voltage differences between the remaining adjacent non-current carrying (receive) electrodes are recorded. EIT images using this technique have usually been made at a single frequency typically 50 kHz (Webster 1989).

More recently, the technique of electrical impedance tomographic spectroscopy (EITS) has been developed (Brown et al 1994a) in the view that tissue can be characterised in terms of how tissue conductivity varies with the applied frequency. This technique also uses an array of electrodes placed around the circumference of the body to produce an image of the frequency dependent changes in tissue resistivity within a region. These are produced from measurements made over a range of frequencies, typically 9.6 kHz to 1.2 MHz.

In a clinical environment, there are essentially two methods of imaging using EIT (Boone et al 1997):

1. Anatomical imaging. This is normally concerned with producing images of the distribution of different type of tissues within a body.
2. Physiological imaging. This imaging technique relies on the physiological state of the tissue within the region being imaged.

Of these two methods, the first can be used as an addition to other imaging techniques already available, such as X-rays, CT and MRI. This could provide information such as the internal conductivity distributions, which are not available from other imaging techniques. The second method may have applications which are not readily amenable to other imaging techniques, for example, imaging the physiological state of tissue with respect to the range of used excitation frequency. In some physiological conditions of tissue, some information seen at higher frequencies may reflect changes that are not seen at lower frequencies. EIT gives access to unique information which is related to the physiology of biological tissue.

### **1.2.1 The Forward problem**

Given a region to be imaged when a known current is injected through electrodes on the surface a potential distribution throughout the system is generated. This potential distribution is dependent on the complex conductivity variation within the region. This potential distribution can be calculated mathematically for a given complex conductivity distribution and a relatively simple geometry and from these potential

distributions one can readily calculate the potential at all points over the surface of the region.

These calculations are generally known as the Forward problem. But these calculations are difficult as either the internal distributions are unknown or the geometry of the region of interest is not simple.

### **1.3 Application of EIT in medicine**

EIT offers some advantages over other medical imaging techniques. As well as providing non-invasive measurements and non-hazardous imaging methods it allows the possibility of long-term monitoring, portability, rapid data acquisition plus cheap and robust instrumentation. There are several areas of clinical medicine where EIT has been suggested for implementation. These have been reviewed and discussed (Brown 1990 and Holder 1993).

#### **1.3.1 Pulmonary ventilation**

It has been shown that there is a high correlation between thoracic impedance change and volume of air breathed (Geddes and Baker 1989). EIT should therefore be an appropriate imaging technique for pulmonary ventilation since there is a large conductivity contrast between inflated and deflated lung tissue together with the fact that a large portion of the thorax is occupied by lung tissue. It has been demonstrated that there exist a strong correlation between inspired air and resistance change in some parts of an EIT reconstructed image for individual subjects (Harris et al 1987, Holder and Temple 1993). Also, Newell et al (1988) showed resistivity changes in the lung region during an induced oedema (accumulation of fluid within the extra-cellular region of tissue). It is therefore reasonable to expect that some lung disorders, such as pneumothorax (air in the pleural cavity) and pleural effusion, which compromise ventilation, may be detected and localised using EIT. This would be beneficial as it would provide an alternative to X-ray investigations.

However, although EIT shows a good measure of lung ventilation in a single individual, it does show large inter-subject variability. It is therefore concluded that EIT is only

practical at present for imaging the differences in ventilation over time on an individual basis (Boone et al 1997).

### **1.3.2 Swallowing disorders**

There are a number of neurological disorders, such as stroke and Parkinson's disease which may cause swallowing difficulties. The severity of disease may be monitored by the determination of the time taken for a bolus fluid to enter the oesophagus. Hughes et al (1994) compared the images of the neck obtained by EIT and X-ray videofluoroscopy during swallowing, and found that all images showed a decrease in impedance regardless of the swallowed fluid conductivity. They also found that at points where the anterior and posterior walls of the pharynx were in closest contact produced the highest changes in the EIT images. The authors did however propose that this feature of the EIT images was due to the expulsion of air from the pharynx rather than being directly related to the bolus of fluid.

### **1.3.3 Stomach emptying**

The rate of stomach emptying can be used to detect gastroesophageal reflux and pyloric stenosis. It can also be used for studying the influence of the component parts of various types of food on gastric emptying, such as the fat proportion (Murphy et al 1987). The present method of measuring stomach emptying are invasive, and therefore are not ideal for routine clinical use. They include: the Marker dilution technique and Scintigraphy (Gamma Camera). EIT can be used to image the profile of gastric emptying due to the change in resistivity which occurs as the food passes through the various stages of the stomach and the upper abdomen. Mangall et al (1987) showed that these changes can be imaged. They found that the profiles of stomach emptying were very similar to those found using the gamma camera and marker dilution technique.

As well as gastric emptying, it has been proposed that EIT can be used to measure gastro-intestinal motility (Smallwood et al 1993), gastric transport (Smallwood et al 1994, Kotre 1995) and oesophageal activity (Erol et al 1995). These studies have shown activity which correlates with other physiological measurements, but it is not clear that the technique is sufficiently accurate for clinical use.

### **1.3.4 Perfusion changes**

During the cardiac cycle there exists a change in thorax resistivity which is due to the redistribution of blood between the heart, great vessels and lungs. However these changes in resistivity are small compared to those due to ventilation and thus cardiac gating is used to separate the cardiac and ventilation information in the EIT recording.

McArdle et al (1993) showed that EIT could only resolve one atrial and one ventricular component in the region of the heart, and these may even overlap. If this was the case, the calculated conductivity would be underestimated, since an increase in one region may cancel a decrease in another. Also the heart movements during the respiratory cycle would cause a further blur in the reconstructed image.

### **1.3.5 Monitoring hyperthermia**

Tumorous growth in normal tissue can be treated by artificially increasing its temperature by the use of microwave radiation or lasers. It is essential to monitor tissue temperature so that normal tissue is not extensively heated and malignant tissue is heated to the desired temperature of about 43°C. The present techniques are invasive; thermocouples are implanted within the patient to obtain temperature profile within the body.

Conway et al (1992) imaged the temperature variation in a saline phantom and in abdomens of human volunteers whose stomachs were rapidly filled and emptied with warm solutions. They showed a good correlation between temperature and EIT image changes. There are however issues that must be taken into account before this becomes clinically acceptable. Tissue conductivity during hyperthermia maybe affected by factors other than temperature. Möller et al (1993) have reported that the resistance of tissue continued to change even after the temperature has been stabilised, and did not return to pre-therapy values after treatment. Also temperatures may need to be monitored for periods as long as an hour. During this time tissue temperature may increase by about 6°C. Baseline drift in the EIT image must therefore be as low as 3% to detect these changes of temperature over long periods (Boone et al 1997). This degree of stability is very difficult to achieve at present.

### 1.3.6 Breast cancer screening

The detection of soft tissue lesions such as cysts and tumours is of particular importance in tissue analysis, for the detection of malignancies in the breast. While X-ray mammography is a useful technique for the detection of these conditions, it is hazardous.

Jossinet and Risacher (1996) have showed that there is a significant difference in impedance between normal and diseased tissue. The procedure however needs static imaging (calculation of absolute values of conductivity, rather than a change from a given reference starting value), which may be possible by the use of multi-frequency EIT.

### 1.4 Electrical properties of biological tissue

The electrical conductivity of biological tissue has been under investigation for over a century. Along with the progress in the measurement technology, the usable frequency range for impedance measurements has been continuously extended.

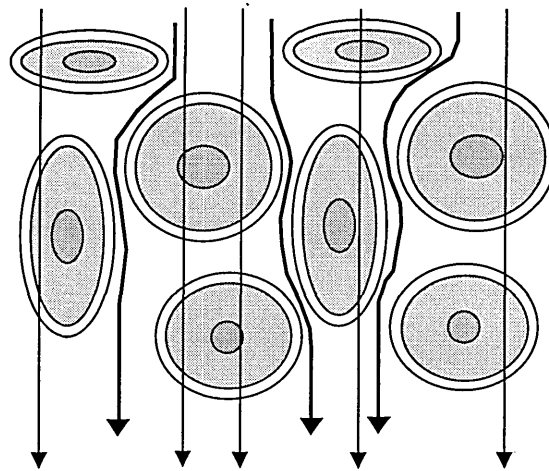


**Figure 1.2. At high frequency the current travels uniformly through the tissue (thin lines) and at low frequency, the current passes round the cell structures through extra-cellular fluid (bold lines).**

Kanai et al (1987) suggested that by using different frequencies the distribution of extracellular to intracellular fluids can be measured. Rigaud et al (1994) have also shown that using this method it is possible to distinguish between various kinds of tissue and to assess the physiological state of a tissue.

Figure 1.2 shows the basic structure of tissue, which consists of cells surrounded by extra-cellular fluid. Intra-cellular fluid is contained within the cells by cell membranes. At low frequency, due to the high resistance of cell membranes, current passes round the cells through the extra-cellular fluid. At high frequency, the capacitance of the cell membrane short circuits and current travels through the tissue structure. The overall impedance of tissue is therefore lower at higher frequencies than it is at lower frequencies.

### **1.5 Electrical model of physiological tissue impedance**

Tissue impedance is complex (it has both magnitude and phase) and the impedance measured over a range of frequencies has a frequency dependent phase and magnitude component. This (complex) impedance of biological tissue can be expressed as a simple electrical model (Kanai et al 1987) as shown in Figure 1.3

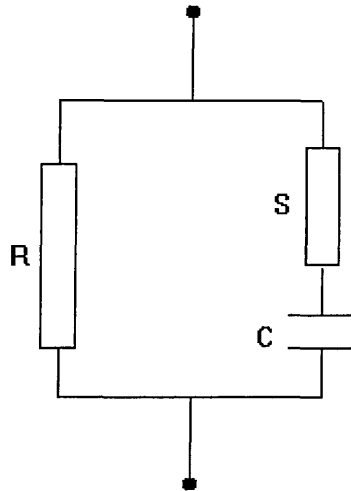


**Figure 1.3 A simple form of electrical equivalent circuit for tissue, where R is the extra-cellular fluid resistance, S is the intra-cellular fluid resistance and C is the cell capacitance.**

In this model Figure 1.3, R represents the resistance of the extracellular fluid, S the resistance of the intracellular fluid and C the capacitance of the cell membranes.

The model in Figure 1.3 can be represented mathematically as (Schwan 1957):

$$Z^* = R_\infty + \frac{R_0 - R_\infty}{(1 + (j \frac{f}{f_r})^{(1-\alpha)})} \quad (1.1)$$

where  $Z^*$  is the complex impedance,  $R_\infty$  is the very high frequency impedance,  $R_0$  is the low frequencies impedance,  $f$  is the measurement frequency,  $f_r$  is the relaxation frequency for the tissue and  $\alpha$  is a constant that is used to match the measured data to the model shown in Figure 1.3. For the diagram shown in Figure 1.3,  $R_\infty = RS/(R+S)$ ,  $R_0 = R$ ,  $f_r = 1/2\pi(R+S)C$  and for a pure capacitance  $C$ ,  $\alpha = 0$ .

As discussed biological tissue impedance is a complex impedance, and so both the magnitude and phase components of data are required for the determination of the total conductivity of tissue. However Brown et al (1994b) have found that due to cable capacitance and body capacitance to ground, the measurement of the quadrature component of the data is unreliable and so at present only the real part is measured over the range of applied frequencies. Some groups have however claimed to be able to measure both the real and imaginary parts of boundary data (Chauveau et al 1996).

### **1.6 Forward Numerical modelling**

It is often necessary to calculate the forward problem for the region under investigation in order to enable image reconstruction from measured data. Of the possible methods available, techniques such as finite element methods have been over the years developed to solve the forward model numerically.

The majority of the reported numerical modelling studies have been restricted to two-dimensions, such as a 2D circular model by Kytomaa and Weselake (1994) and the symmetrical 2D homogenous and isotropic model by Basarab-Horwath et al (1995). Some work has been carried out using three dimensional models by Shahidi et al (1995) who modelled a three dimensional cylindrical tank and also a three dimensional thorax model built from 43 CT scans at 1 cm intervals. Kim (1994) also used a three dimensional model of the thorax consisting of 658 elements and 29 layers.

Many researchers have used various methods in solving the forward problem. The most common method, to date, has been by applying the finite element method to solve Laplace's equation in the region of interest (Kytomaa and Weselake 1994, Meaney and Moskowitz 1993, Kim 1994, Basarab-Horwath et al 1995, Paulson et al 1992, Lin et al 1994). Other methods of numerical modelling includes the work of Griffiths (1995)

who has used a finite difference model to investigate the non-invasive characterisation of tissue.

The forward model can be given as

$$\nabla \cdot (\sigma \nabla V) = 0 \quad (1.2)$$

where  $\sigma$  and  $V$  are the conductivity and the electric potential distribution respectively where conductivity  $\sigma$  is known and

$$\sigma \nabla V \cdot \mathbf{n} + \mathbf{J}_n = 0 \quad (1.3)$$

where  $\mathbf{n}$  is a vector normal to the electric potential and  $\mathbf{J}_n$  is the normal current density for a given point on the boundary.

For a unique solution of equation (1.2) to exist, sufficient boundary conditions must be specified. These may be Dirichlet conditions in the form of potentials on the boundary or Neumann conditions in the form of current densities crossing the boundary or a mixture of both. The potential must be specified at a minimum of one point for a unique solution of equation (1.2) to exist.

In the methods utilised for solving the forward problem by most researchers it has been widely assumed that the injected current is at zero frequency (dc). Lin et al (1994) have however specified the current density in their work to be:

$$\mathbf{J} = -(\sigma - j\omega\epsilon_0\epsilon_r)\nabla V \quad (1.4)$$

where  $\omega$  is the angular frequency ( $\omega = 2\pi f$ , where  $f$  is the frequency),  $\epsilon_r$  is the relative permittivity of material within the region of interest and  $\epsilon_0$  is the permittivity of free space.

In equation (1.4) it is therefore possible to specify the current density as a function of frequency and permittivity as well as conductivity.

Other workers (Shahidi et al 1995) have used and solved a derivative of equation (1.2):

$$\nabla \sigma(\xi) \cdot \nabla \Phi(\xi) + \sigma(\xi) \nabla^2 \Phi(\xi) = 0 \quad (1.5)$$

where  $\sigma(\xi)$  is the conductivity,  $\Phi(\xi)$  is the electric potential distribution and  $\xi$  is the spatial co-ordinates within the volume of interest  $\Omega$ . In equation (1.5), conductivity and potential distribution are defined as a function of spatial co-ordinates.

The boundary condition in this case was (from equation (1.3)):

$$\sigma(\xi) \frac{\partial \Phi(\xi)}{\partial n} = \begin{cases} +J & \text{on the source electrode} \\ -J & \text{on the sink electrode} \\ 0 & \text{elsewhere on the surface} \end{cases} \quad (1.6)$$

where  $\frac{\partial \Phi(\xi)}{\partial n}$  is the normal component of the potential gradient and J is the current density.

Using this method and equations (1.5) and (1.6) the scalar potential was computed throughout the model by the authors.

The present trend is advancing towards multi-frequency EIT with frequencies ranging from 9.6 kHz to 1.2 MHz (Brown et al, 1994b). Zero frequency simulation does not take into account the effect of frequency (by definition) and will not accurately predict the behaviour of a multi-frequency system.

Three-dimensional analysis is becoming popular and straight forward in the field of numerical modelling, and it therefore presents no restrictions in building a model which includes the third dimension. The differential equations will still apply to a three dimensional model.

Future improvements in numerical modelling in EIT requires an extension from dc analysis to multi-frequency ac analysis. When a multi-frequency EIT system is used, varying tissue conductivity with frequency will have an effect on the measured data. To gain maximum advantage from such a system the varying tissue conductivity must be considered in any forward modelling.

## **1.7 Problems encountered in EIT**

Calculation of the absolute distribution of tissue conductivity is hindered by the fact that it is difficult to calculate with sufficient accuracy the distribution of surface voltages developed when a current is passed through the object (the forward problem) as well as the measurement noise embedded in the obtained data in practice. Since these distributions are needed for image reconstruction it has not been possible to produce stable and reliable solutions to the impedance distribution from in-vivo data. The group at University of Sheffield was the first to show that images of relative changes can be produced which do not require explicit solution of the forward problem. These images were produced assuming a linearised problem, i.e. any changes from a uniform reference conductivity was assumed to be small enough to be neglected. However since these images are images of normalised changes they are often difficult to interpret. The only well established quantitative use of these images has been in the measurement of temporal changes in impedance, such as those observed in gastric emptying (Erol et al 1995). In addition EIT is strictly a three-dimensional imaging technique, and qualitative accuracy could only be expected from images constructed from three-dimensional data. As most images to date have been two-dimensional there has been little incentive to try and improve the quantitative accuracy of EIT although there is little doubt that quantitative measurements of tissue electrical properties could provide useful clinical information.

Image reconstruction in EIT is a non-linear reconstruction problem because the forward problem in EIT is itself non-linear (Brown and Barber 1984). Over the last 15 years, multi-electrode systems have been developed to collect sets of impedance data enabling the reconstruction of images of the distribution of electrical resistivity within objects. More recently, systems have been developed to collect impedance data over a range of frequencies, and also systems which collect data to enable three dimensional image reconstruction. Techniques also have been developed for the modelling of biological tissue impedance as a function of frequency of the applied current (Brown et al, 1994b).

Tissue impedance is a complex parameter and measured data is complex (Rigaud et al, 1994). However, one key practical consideration with in-vivo data collection is that it is difficult to accurately measure the imaginary part of the signal because of the effects of

stray capacitance (Brown et al, 1994b). In practice therefore only the real part is easily available. This may lead to some loss of quantitative accuracy in the images.

Another problem encountered with EIT is that impedance image reconstruction is ill-posed (Kytömaa and Westlake 1994) and therefore efforts are needed to ensure that the algorithm produces a useful solution. This problem arises largely from the fact that current does not flow in a straight path between electrodes placed on the surface of an object. In EIT the electrical flow path is a function of the unknown internal conductivity distribution of the object under investigation, and the reconstruction problem is itself non-linear. Also because the current flow cannot be confined to a plane, the images therefore reflect changes in conductivity occurring in a broad region of the body.

### **1.8 Aims and objectives**

Numerical modelling has already been shown to be useful in EIT (Basarab-Horwath et al 1995, Basarab-Horwath and Dehghani 1998, Kytömaa and Westlake 1994, Meaney and Moskowitz 1993, Kim 1994, Paulson et al 1992, Lin et al 1994, Shahidi et al 1995, Griffiths 1995). The data generated using numerical methods is used to assess the accuracy of image reconstruction. The first aim of this study was to identify and successfully implement a commercially available finite element modelling software package. Once a suitable software package had been chosen, a number of problems encountered in electrical impedance tomography were investigated.

Physical phantoms of the human thorax are not available. That is to say that we can not presently image a human thorax and then observe what is contained within that thorax (we can not simply cut it up) to compare with the reconstructed image. Thus the accuracy of an EIT image of the human thorax is at present purely judgmental. A two-dimensional (2D) finite element model of the thorax is needed, to allow the simulation of an idealised human thorax. This can be used to assess the accuracy of presently available EIT systems, and particularly the image reconstruction method used.

At present the group at the University of Sheffield are able to collect data from objects using a range of applied frequencies (Brown et al 1994a) and they have shown that in principle reasonably accurate images of derived tissue electrical parameters can be produced. This group has also completed the construction of a data collection system

which can collect three-dimensional data (Metherall et al 1996). These developments offer the possibility of producing, for the first time, quantitatively accurate images. However accuracy will also be determined by other factors such as the reconstruction algorithm used and noise on the measured data and the effects of these need to be explored. Models of tissue impedance as a function of frequency of applied current are well established (Brown et al 1994b). Part of this thesis is concerned with the development of modelling techniques which can incorporate these models to generate complex data from a variety of idealised and realistic simulations.

Image reconstruction in multi-frequency EIT is investigated in this work when real only data is used and these are compared to images when complex (real and imaginary) data are used. The importance of ignoring the imaginary part of the data is explored.

The initial part of this project involved the construction of some simple numerical models, essentially one geometrically simple object of various sizes and impedance contrast in a 'uniform' background. In the first instance a two dimensional model was constructed to investigate EIT system performance. The visibility of the system was studied as a function of its conductivity, permittivity and permeability over a range of excitation frequencies. Also, the visibility of an anomaly within a three dimensional model was investigated to demonstrate the modelling capability in three dimensions. However most of this thesis, except section 3.5.2.1, will only concentrate on 2D.

At the second stage of the study, image reconstruction in single frequency EIT was investigated using the sensitivity algorithm. The accuracy of this method is studied, and improvements in image quality using *a-priori* information and implementation of an iterative method are also investigated. A finite element model of an idealised human thorax was therefore developed to allow simulation of realistic data. This model is used to solve the forward problem and generate boundary data.

Finally, the effect of frequency in multi-frequency EIT is studied. The importance of complex conductivity as well as complex data is highlighted and improvements are suggested. The already developed model will then represent tissue impedance as a function of the frequency of the applied current and will generate complex data from a

variety of idealised and realistic simulations. This will enable the assessment of the accuracy of present image reconstruction algorithms in multi-frequency EIT.

### **1.9 Chapter description**

Chapter 1 introduces the concept of medical imaging. Electrical impedance tomography is described and some applications to medicine are introduced. Previous work in numerical modelling is discussed and the problems encountered in EIT are also given.

Chapter 2 introduces and discusses the forward and inverse problem. Numerical methods are discussed in more detail together with the approach taken in this thesis.

Chapter 3 details the forward modelling together with initial findings for measures of performance in an ideal EIT system.

Chapter 4 introduces the concept of image reconstruction in single frequency EIT. Methods of image reconstruction are discussed together with problems encountered. Quality of reconstructed images are presented and a new iterative reconstruction algorithm is presented.

Chapter 5 discusses multi-frequency image reconstruction. Limitations in the present methods are shown and the effects of ignoring complexity of the data are presented. Full complex reconstructed images are presented.

In the last chapter, the overall results are discussed and a conclusion to the study is given together with suggestions for future work.

## Chapter 2

### 2. The solution of the Forward problem

#### 2.1 Introduction

In electrical impedance tomography, we are concerned with the calculation of the internal conductivity distribution from given boundary voltage measurements. Now consider the case where the calculation of the boundary voltages from a given internal conductivity distribution is required. That is

$$d = Gc \quad (2.1)$$

where  $d$  is a vector of the boundary voltages,  $c$  is a vector of the internal conductivity distribution and  $G$  is a transform function. This relationship is known as the Forward problem, Figure 2.1.

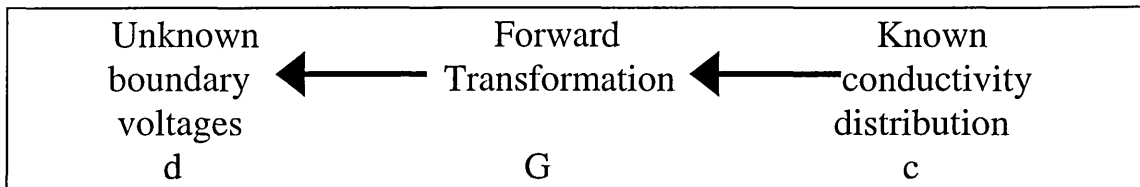


**Figure 2.1. The Forward problem in EIT. This corresponds to the calculation of boundary voltages from a given known internal conductivity distribution.**

The Forward problem involves the determination of the electric potential distribution throughout a region, given the conductivity distribution of the system. There are a number of methods available for the calculation of the Forward problem. These are discussed in the following sections of this chapter.

The Inverse problem is the determination of the internal conductivity distribution of a system given the boundary voltage measurements; this is shown in Figure 2.2. Here

$$c = G^{-1}d \quad (2.2)$$

where  $G^{-1}$  is the Inverse transform function.

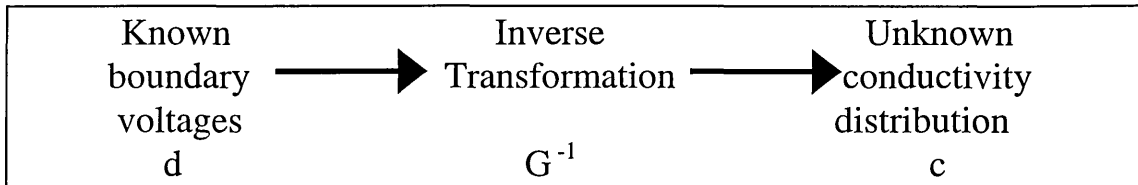


Figure 2.2. The inverse problem in EIT. This corresponds to the calculation of the internal conductivity distribution from a given known set of boundary voltages.

## 2.2 The Forward problem

In order to obtain the electric potential throughout a given region of known conductivity distribution and hence obtain the boundary voltages on the periphery, the Forward problem for the given conductivity distribution and shape must be solved. The Forward problem can be represented as a set of partial differential equations that can be solved to obtain the solutions for a given system.

There are two techniques available which can be utilised for the solution to the partial differential equations, numerical and analytical. In the analytical method, the solution takes the form of an algebraic function into which the values of parameters defining the particular system can be substituted. Generally speaking, analytical solutions are most likely to be successful in the case of fields which are, or can be treated, as two-dimensional (Binn et al, 1992). Otherwise, numerical solutions which take a set of values of the function describing the system, becomes appropriate.

For the purpose of this work, the numerical approach has been used for the calculation and the solution of the Forward problem. Numerical methods are a process whereby a model of a system or physical situation is described as a set of equations which are then solved numerically, usually with the use of a computer. A numerical method has many advantages: it allows the performance of experiments numerically, in situations where they are not otherwise physically possible or would not be cost effective. The advantage of numerical methods over analytical is simply that numerical solutions are possible where analytical solutions are not. As an example, no analytical solution has been published to date for the electric potential distribution within an EIT system containing multiple anomalies (Basarab-Horwath and Dehghani 1998). Analytical solutions do however exist for the electric potential distribution on the boundary of a uniform circular plane (Bland 1961, Seagar 1983) and throughout a uniform circular plane

(Pidcock et al 1995a, 1995b). Seagar (1983) has also produced the analytical solution for a single anomaly within a uniform region. He has also presented a solution for simple multi-anomaly system, but this takes the form of a combined numerical and analytical solution.

The Forward problem concerned in EIT is essentially an electromagnetic problem. That is to say, given a system of conductivity, permittivity and permeability distribution and the pattern of a given current injection at a point on the boundary, the solution is the resultant electric and magnetic field throughout the system, and from this the resulting current and voltage distribution. The problem is therefore best given as an electromagnetic problem, and using numerical methods, it hence becomes a computational problem.

### **2.3 The computational Forward problem**

For the computational Forward problem, the electromagnetic field for a given system is solved by the use of numerical methods. Numerical analysis is a particular approach for solving mathematical problems. In numerical analysis, the differential equations are converted to a set of algebraic equations by using certain mathematical techniques. The solution of the system of algebraic equations is a set of the values of physical variables on the nodes of the grid used to discretise the problem.

The development of the numerical computation of electromagnetic fields is assisted by modern computer technology. The most commonly used numerical methods are the finite element method (FEM), the finite difference method (FDM) and the boundary element method (BEM). Of these three methods, each has its advantages and disadvantages.

FDM has been widely used in fluid dynamics and semi-conductor modelling as well as a limited cases of EIT simulations (Griffiths 1995). It has however been replaced by FEM in many other branches of engineering modelling (Silvester and Ferrari 1990). The main drawbacks of FDM are (Hua and Woo 1990):

1. There are considerable difficulties in modelling problems of complex boundaries since the discretization scheme has a fixed topology.

2. FDM gives point wise approximation to the governing equation (1.2), whereas FEM gives a piecewise approximation to the solution.

Both of these problems are overcome by the FEM.

In BEM only the boundary surfaces must be discretised. Because the computational mesh is simpler in BEM, it requires less computation. In general FEM is preferred for problems where the region of interest is highly heterogeneous, whereas BEM method is preferred for highly homogenous regions.

The FEM has in recent years become by far the most popular technique in computational electromagnetic analysis. Many general purpose computer packages have been developed which provide the basis for computer aided design (CAD) systems. The technique is not suitable for hand calculations and the algorithm is somewhat complicated.

In FEM the solution domain can be discretised into a number of uniform or non-uniform finite elements that are connected via nodes. The change of the dependent variables with regard to location is approximated within each element by an interpolation function. The interpolation function can be of 1st or 2nd order polynomials (implying the existence 1st or 2nd order elements), however, a higher order polynomial provides a greater accuracy. The interpolation function is defined relative to the values of the variables at the nodes associated with each element. The original boundary value problem is then replaced with an equivalent integral formulation. The interpolation functions are then substituted into the original equation, integrated, and combined with the results from all other elements in the solution domain. The result of this procedure can be reformulated into a matrix equation of the form

$$aV = b \tag{2.3}$$

which is a re-written form of Laplace's equation with

$$a = \nabla \cdot \sigma \nabla \tag{2.4}$$

FEM is a powerful method of calculating the Forward solution by determining the field distribution based on the tissue properties. The element sizes and shapes can be

1. Designed to accurately model the contours of the body being studied.
2. Made relatively small in areas where the field varies rapidly and relatively large in areas where the field is relatively uniform.

In this manner the problem can be discretised with a minimum number of nodes which directly influences the size of the matrix that will have to be inverted and hence reduce computation time.

FEM also provides a fast, quick and reliable method for examining the various effects of EIT system construction and image reconstruction methods. Researchers have used this technique to validate their method, and to find solutions to problems which otherwise would have been difficult. Shahidi et al (1995) have for example used this method to examine the effect of electrode configurations, the sensitivity to off-plane objects and to noise in measured data. They have also used this method to validate the modelling procedures by comparison of numerical results with experimental data acquired from a similar physical model.

Kytomaa and Weselake (1994) have used an iterative finite element approach to look at accuracy and speed of image reconstruction using a combined choice of current projection and mesh geometry. Others have also used this method to look at various reconstruction algorithms (Shahidi et al 1995, Lin et al 1994, Ruan et al 1994).

More recently Kolehmainen et al (1997) used FEM to study the effect of boundary shape of an object, electrode size and localisation and electrode contact impedance in resulting reconstructed images. This study was however confined to 2D, and the problem was treated as a dc problem.

The modelling of current flow through a region being imaged is an essential component in EIT since frequent solution of the Forward problem is often required. In an iterative image reconstruction method for example, boundary voltages are calculated for an 'approximated' conductivity distribution and these calculated boundary voltages are compared to the actual measured voltages. The final image is a conductivity distribution

for which the difference between the measured boundary voltages and the calculated boundary voltages is at a minimum. Accurate Forward modelling is therefore a major component in such an iterative image reconstruction method. In general due to ill-conditioning of the problem, errors in the voltages measured on the electrodes are translated into large errors in the calculated conductivity distribution.

As shown majority of previous studies concerning the modelling of EIT have restricted themselves to dc analysis. It is assumed for this work that dc analysis of an EIT system will not be accurate since biological tissues have properties which will respond differently to different excitation frequencies. To further investigate this assumption full multi-frequency modelling and analysis will be needed.

FEM has been developed and improved over many years, and it is the numerical method which is utilised for this work.

#### **2.4 Finite element analysis**

There are several effects as a result of ac current which need to be considered in any multi-frequency analysis. Such effects are best described by Maxwell's equations:

$$\nabla \times \mathbf{H} = \mathbf{J} + \frac{\partial \mathbf{D}}{\partial t} \quad (2.5)$$

$$\nabla \times \mathbf{E} = -\frac{\partial \mathbf{B}}{\partial t} \quad (2.6)$$

$$\nabla \cdot \mathbf{D} = \rho \quad (2.7)$$

$$\nabla \cdot \mathbf{B} = 0 \quad (2.8)$$

$$\mathbf{D} = \epsilon \mathbf{E} \quad (2.9)$$

$$\mathbf{H} = \frac{1}{\mu} \mathbf{B} \quad (2.10)$$

where  $\mathbf{H}$  is the Magnetic field intensity vector ( $\text{Am}^{-1}$ ),  $\mathbf{B}$  is the Magnetic flux density vector (T, Tesla),  $\mathbf{E}$  is the Electric field intensity vector ( $\text{Vm}^{-1}$ ),  $\mathbf{D}$  is the Electric flux

density vector ( $\text{Cm}^{-2}$ ),  $\mathbf{J}$  is the electric current density vector ( $\text{Am}^{-2}$ ),  $\epsilon$  is the absolute permittivity,  $\mu$  is the absolute permeability, and  $\rho$  is the electric charge density ( $\text{Cm}^{-3}$ ).

In order to investigate the effect of varying frequency and its contribution to the resulting displacement and eddy currents, both the dielectric constant and permeability of the tissue must be incorporated into the model as well as tissue conductivity.

Equations (2.5) - (2.10) can be used in conjunction with Coulomb's gauge to produce a complete set of coupled equations that define the EIT model accurately (Appendix A).

It can be shown that the full set of coupled equations that represent a full 3D electromagnetic fields model can be given as (Appendix A):

$$\nabla \times \frac{1}{\mu} \nabla \times \mathbf{A} - \left\{ \nabla \frac{1}{\mu} \nabla \cdot \mathbf{A} \right\} + (\sigma + j\omega\epsilon) \left( \frac{\partial \mathbf{A}}{\partial t} + \nabla V \right) = 0 \quad (2.11)$$

$$\nabla \cdot (\sigma + j\omega\epsilon) \left( \frac{\partial \mathbf{A}}{\partial t} + \nabla V \right) = 0 \quad (2.12)$$

and in regions with zero conductivity

$$\mathbf{A} \cdot \mathbf{n} = 0 \quad (2.13)$$

is imposed on the external boundaries to all conductors, where  $\mathbf{A}$  is the vector potential and  $\mathbf{n}$  is a vector normal to  $\mathbf{A}$ . In addition, for ac problems which approach the dc limit, the gauge condition becomes weaker as the frequency decreases.

There are instances where in a model of interest both displacement current and conduction current are significant, whilst eddy currents are not. In this case the equation to be solved is (Appendix A):

$$\nabla \cdot (\sigma \nabla V + \epsilon \nabla \frac{\partial V}{\partial t}) = 0 \quad (2.14)$$

### **2.4.1 Modelling stages in finite elements**

There are essentially 5 stages in any given single modelling problem. These stages are discussed below and a flow chart showing a complete modelling procedure is shown in Figure 2.3.

#### **Level 1. The Physical Model:**

The physical model is defined. This includes physical geometry information, material identification and property and also charge density throughout the model.

#### **Level 2. The Mathematical Model:**

In this stage the partial differential equations to be solved are identified, boundary conditions and values are assigned (e.g. fixed boundary currents and voltages), and also the symmetry of the problem may be exploited (if the model is symmetrical, only part of the model may need to be solved as the solution may also be symmetrical).

#### **Level 3. The Finite Element Model:**

The physical model is divided into smaller sections (triangular or brick elements) and element matrices are formed using, for example, the Galerkin method (Silvester and Ferrari 1994).

#### **Level 4. The Algebraic Model:**

The Element matrices are merged together to obtain a banded symmetric system matrix with boundary conditions included.

#### **Level 5. The Computer Model:**

The system is solved by, for example, Gaussian Elimination (Mitchell and Griffiths 1977).

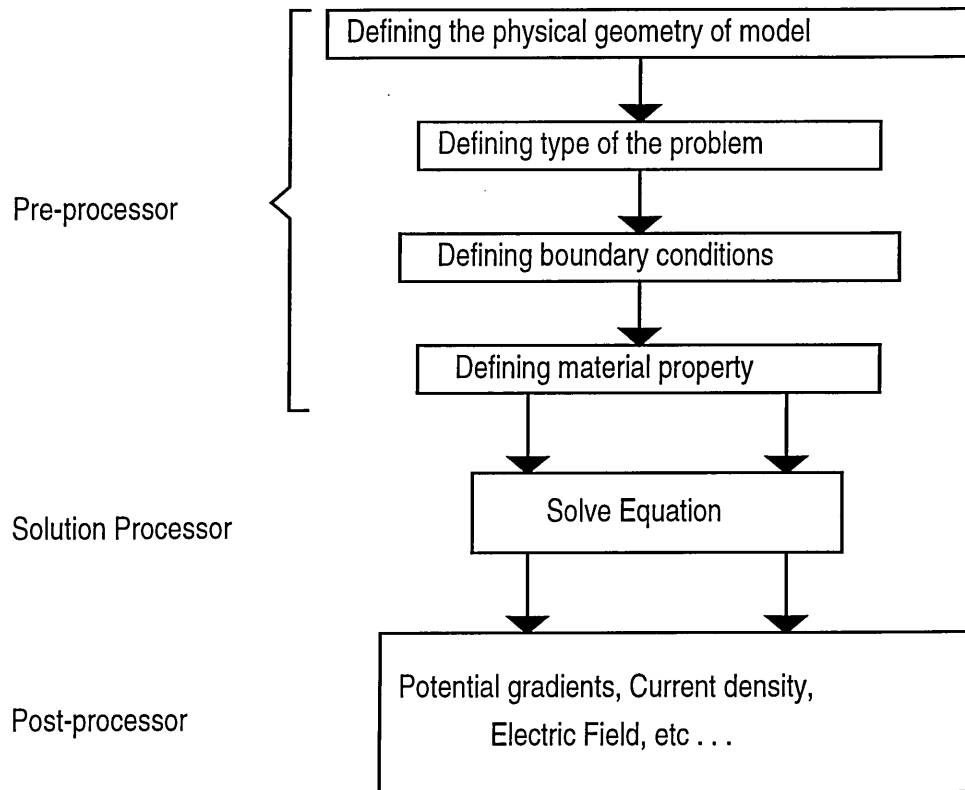


**Figure 2.3. FEM, A diagrammatic presentation**

In general there are three main sections in any single model. The first is the pre-processor stage for data and mesh, second is the solution processor stage and third the post-processor stage where solutions are extracted.

The physical, mathematical, finite element and the algebraic model are all defined in the pre-processor. The physical geometry, material property and identification, boundary conditions, symmetry identification, problem specification and element matrix formation are also defined at this stage. The model is then saved as a file or a combination of files, and solved using the software's solver. If any errors are encountered during this stage, it will be necessary to return to the pre-processor and re-inspect and redefine the model. Such errors would be errors encountered if the model has not been constructed accurately as discussed earlier in this section. Once the model has been successfully solved, numerical results can be viewed in the post-processor. It is at this stage that the user can define the desired output variables, in a chosen format i.e. graphical display and / or ASCII output file. Any required data processing can then be performed on the obtained results.

#### **2.4.2 Finite Element software for Electromagnetic simulation**

Various commercially available software packages for solving electromagnetic problems have been evaluated in order to seek the best software that matched the needs of finite element analysis in EIT. Some were found to meet only part of the requirements of EIT, and software that fully satisfies all requirements was found to be difficult to obtain. In this section, the evaluated software will be briefly discussed, and the limitations of each will be presented.

##### **2.4.2.1 ELEKTRA by Vector Fields (version 7)<sup>1</sup>**

ELEKTRA can use a combination of vector and scalar potentials to model time varying electromagnetic fields. Vector potentials have to be used in conducting media, and scalar potentials can be used in free space and zero conductivity media.

Various analyses were performed in order to determine the limitations of the package. An important limitation is that the software does not allow the specification of a

---

<sup>1</sup> Vector Fields Ltd, 24 Bankside, Kidlington, Oxon, OX5 1JE, UK

constant current as a boundary condition. This meant that a constant potential had to be defined instead, and the current flowing through the model had then to be measured to enable the re-scaling of the potential to provide the required value of constant current.

Another limitation of the software is that an analogy had to be used between the electrical problem at hand and the magnetic problem that the software is designed to analyse. This can lead to complications.

The main limitation of the software is that it does not allow for displacement currents within the model. For the purpose of this study displacement currents are thought to be of importance in EIT, and hence should not be ignored. Biological tissue have a very high dielectric constant, and at high frequencies, displacement currents will become significant. As the software does not solve for the full set of Maxwell's equations, it would not allow for the effects of eddy currents.

ELEKTRA from Vector Fields is a reliable FEM software for electromagnetic problems. It is not however very user friendly and it was found that ELEKTRA was not a suitable FE analysis package for finite element modelling of EIT.

#### **2.4.2.2 Maxwell 2D Field Simulator by Ansoft (version 3.0.12)<sup>2</sup>**

Maxwell's field simulator comes with various solvers, including the 2D eddy current solver, and 2D ac conduction solver.

The ac conduction field simulator solves for the current flow due to a boundary potential value, but it does not, however, solve for the magnetic and electric field effects due to the displacement current. The effects of eddy currents in conductors and time-varying currents is simulated by the Eddy Current 2D Field Simulator.

The Eddy current 2D field simulator assumes a current flowing into the plane of the geometry, which is not the case in EIT, where the current is flowing through the plane. Therefore the 2D simulator was found not to be suitable for EIT.

---

<sup>2</sup> Ansoft Europe, Regal House, 9th Floor, 70 London Road, Twickenham, Middlesex, TW1 3QS, UK

### **2.4.2.3 Maxwell 3D Eddy Current Field Simulator by Ansoft (version 3.0.12)**<sup>3</sup>

The eddy current field simulator computes time varying magnetic fields that arise from either ac currents and/or External time-varying magnetic fields.

The solver, however, ignores all effects of displacement current. Another restriction is that the solver only looks at effects caused by the eddy current (Ansoft manuals). This is to say that the ac current flow can not be simulated using this solver. Also the solver does not calculate voltages, rather, it deals only with currents.

### **2.4.2.4 Electromagnetic solver by Ansys (version 5.0a)**<sup>4</sup>

The electromagnetic solver by Ansys implements the Vector potential method both for 2D and 3D electromagnetic fields.

The displacement current is again ignored. In this solver, only the eddy currents are investigated, and effects from conduction currents are ignored. Again the solver does not calculate voltages, it only deals with current.

Ansys also provides a steady state current analysis, which is used to determine the current density and electric potential distribution due to direct current (dc) or potential drop. If this solver had been for ac current conduction, it would have provided an adequate tool for the analysis to be carried out in this project. The two solvers (electromagnetic and AC current conduction) then could have been coupled for the following purpose: the time varying current can be calculated using the steady state ac conduction solver, and its results can be used to stimulate eddy current effects using the electromagnetic solver. The effects of the Eddy currents can be therefore compensated using the ac conduction solver, once they are known (providing the displacement current effects could have been allowed for). So it becomes apparent that to solve for all of Maxwell's equations, to obtain the ac conduction solution which would include the effects of eddy currents, and hence skin effect, it is necessary to solve for ac conduction and eddy currents simultaneously.

---

<sup>3</sup> Ansoft Europe, Regal House, 9th Floor, 70 London Road, Twickenham, Middlesex, TW1 3QS, UK

<sup>4</sup> ANSYS Europe, Wyvols Court, Swallowfield, Reading RG7 1PY, UK

However, this was not found to be possible since the required ac conduction current solver was not available and hence further investigations using Ansys were abandoned.

#### **2.4.2.5 Three dimensional Electromagnetic Analysis by MEGA (version 6.24)**<sup>5</sup>

MEGA is a fully integrated software package for solving 2D and 3D electromagnetic problems using the FEM. It solves for steady-state ac with eddy currents.

MEGA can solve for equations (2.11) - (2.13) and therefore does not ignore eddy currents or displacement currents. It is capable of both 2D and 3D modelling. A constant current can be set at an electrode face, and boundary voltages can be obtained throughout the system. If eddy currents can be neglected, it is possible to solve only for conduction and displacement current, equation (2.14).

### **2.5 Conclusion**

The idea of the Forward modelling to solve for the potential distribution within a given region has been presented. The underlying equations that describe such a system are given and from the number of numerical methods available for solving these equations, FEM has been discussed and chosen.

The underlying method for finite element analysis is discussed and basic modelling stages using this method are also stated. A number of FEM software packages have been reviewed for the purpose of solving the Forward model in EIT and MEGA was chosen as it solved the equations that best described an EIT system.

---

<sup>5</sup> Applied Electromagnetics Research Centre, University of Bath, Bath, BA2 7AY, UK

## Chapter 3

### 3. Modelling of the Forward problem

#### 3.1 Introduction

To obtain the solution of the Forward problem, that is the electric potential distribution within an EIT model for a given system, the numerical method based on FEM has been chosen. The FEM software is a commercially available software package, MEGA, and in this section basic modelling stages are described for this software. A detailed description of modelling procedures can be found in Appendix B.

#### 3.2 Modelling method and model construction

The procedures described here are the basic steps taken to construct an EIT model using the available FEM package, MEGA.

Initially, the physical geometry of the problem is defined. For the work described here (except where stated for eddy current formulations where the model needs to be 3D), the modelled phantom is a 2D circular disk of radius 5 cm, Figure 3.1. A total of 16 electrodes are also modelled and are constructed on the outermost circumference of the circular phantom. The electrodes are placed equidistant from each other. A total of 2048 brick and triangular elements are used, with 1920 elements making up the circular phantom and 8 elements for each of the 16 electrodes on the periphery.

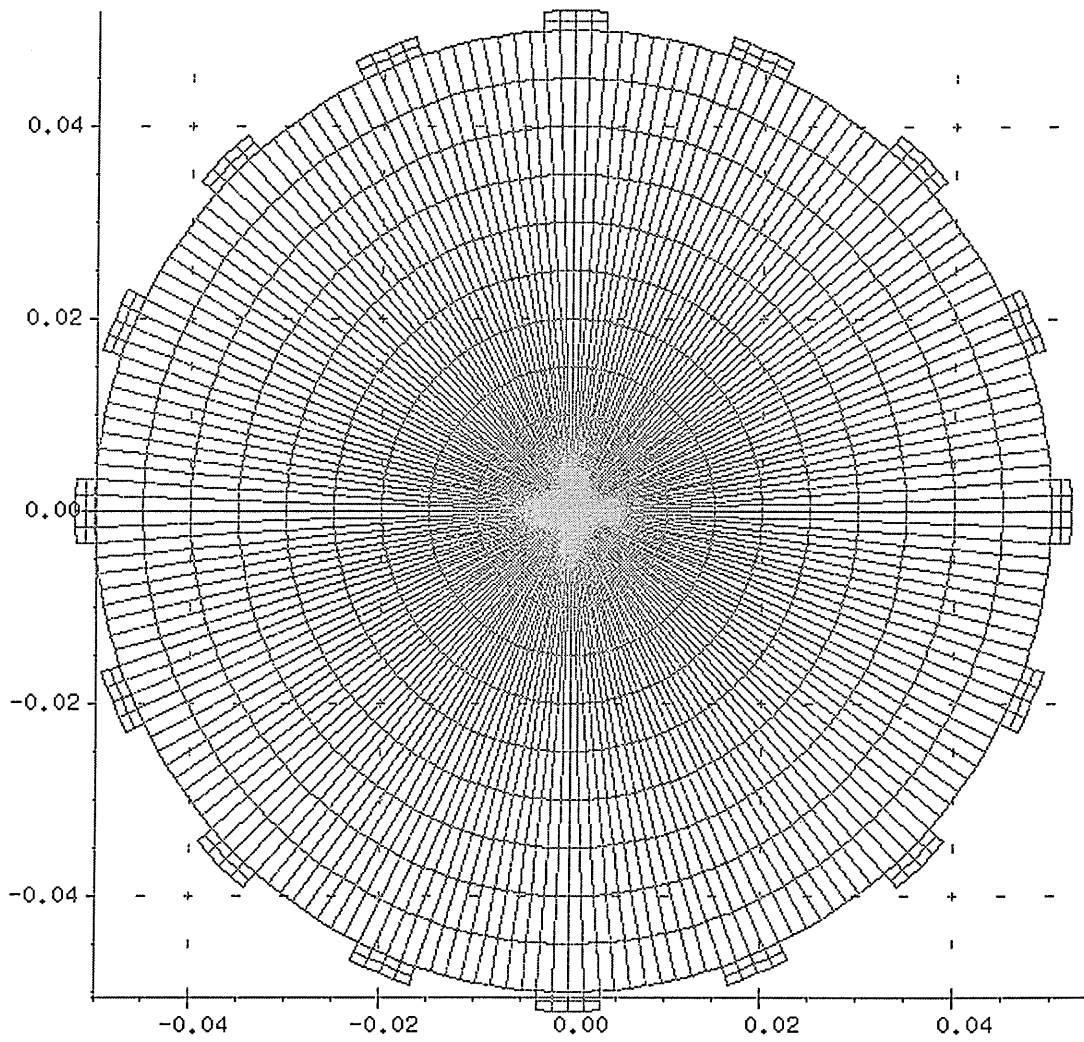


**Figure 3.1. The FEM of the circular phantom.**

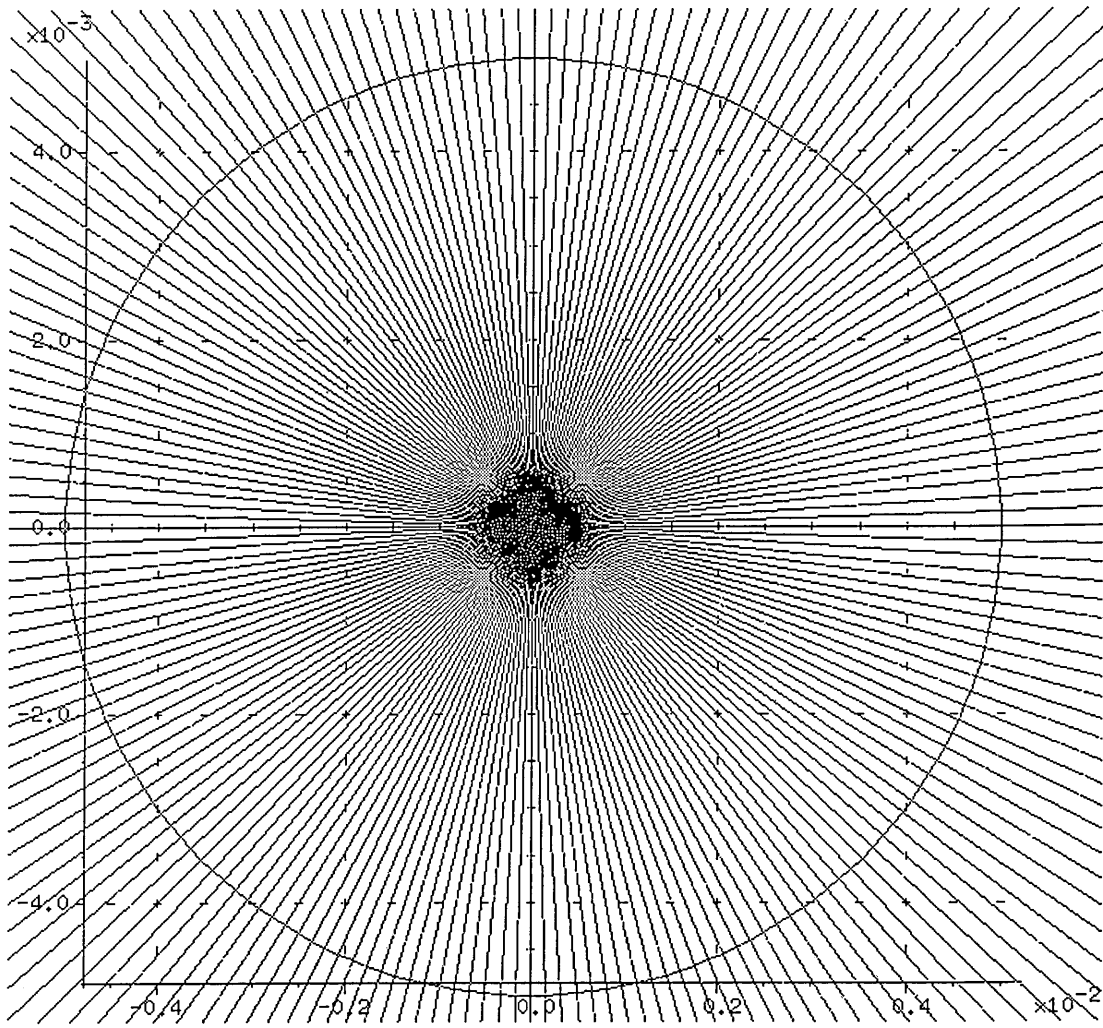


**Figure 3.2. Central radius of Figure 3.1 enlarged to display the small triangular elements placed at the centre.**

The elements used in this model are second order elements which allows for a more accurate solution. First order elements may be used for a coarse approximation to the solutions, after which the user has the option of either increasing the number of elements used, or increasing the order of elements for a more accurate solution. The latter option is more desirable, since it only involves the setting of a flag in the software for the same distribution of the elements, rather than having to re-define the element distribution to increase element number.

The central elements shown in Figure 3.1 are of small sizes, and these are magnified and shown in Figure 3.2. Generally, such a large number of elements are not crucial and it is preferred to use large regular elements within central regions. However, the software package only allowed semi-auto mesh generation and a limited freedom was available for mesh alterations. However for the work described here and in the following sections, this large number of elements within the mesh presented no disadvantage and all proposed methods will be applicable to any mesh definition.

The material properties are next assigned, the values of which are shown in Table 3.1. The modelled phantom was considered to contain a uniform distribution of saline, into which objects of various electrical properties and sizes would be placed. The electrodes are considered to be much more conductive than the saline.

**Table 3.1. Electrical properties of material in modelled phantom**

	Conductivity ( $\text{Sm}^{-1}$ )
Saline	1
Electrodes	10000

The material property used for the uniform model are considered to be neither magnetic nor capacitive. The permeability and permittivity value were therefore not defined.

The problem type chosen for this model is the formulation needed where conduction current and displacement current both have significant effects and no eddy currents are present Equations (2.14). Where permeable material are present, eddy currents will also

be significant. For such studies the formulation needs to be adjusted to account for this effect.

The geometry of the physical model has so far been designed and a finite element model constructed. The material property has been specified and the type of problem has been set. Next, a current source must be specified at the face of one electrode and a ground reference point at face of another electrode. In this study an adjacent drive / receive electrode combination was used. That is, the current is injected through one electrode and extracted through the neighbouring electrode, Figure 3.3.

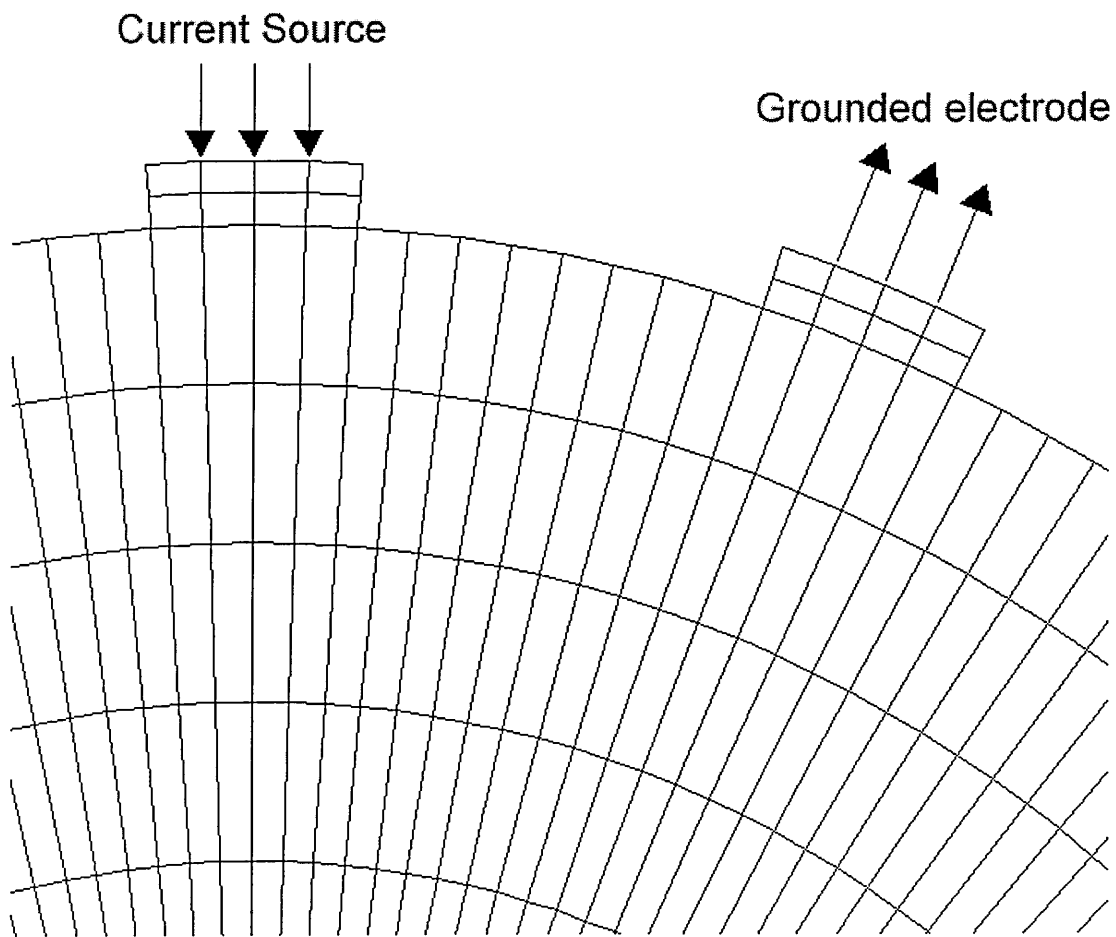


**Figure 3.3. Diagram showing points along two adjacent electrodes where current is injected and extracted.**

The frequency of excitation can also be set. For the purpose of this particular model, the excitation frequency was set at zero Hertz. If displacement current analysis is to be performed a non-zero excitation frequency must be specified.

The constructed model is now complete. Once the solution to the model has been calculated a number of variables can be extracted from this solution. The simplest extractable parameter, and also the most useful for our studies is the electric potential distribution throughout the model. Figure 3.4 shows the equipotential for the modelled uniform phantom.

Electric potential throughout the model, at each nodal positions of all elements are available. We are concerned with calculating voltages underneath or at the electrode / main body contact region, where in practice, this voltage would be measured using instrumentation. These values can be extracted from the model, and an example of such is shown in Figure 3.5. This plot shows the boundary voltage distribution for a uniform model solved as described above.

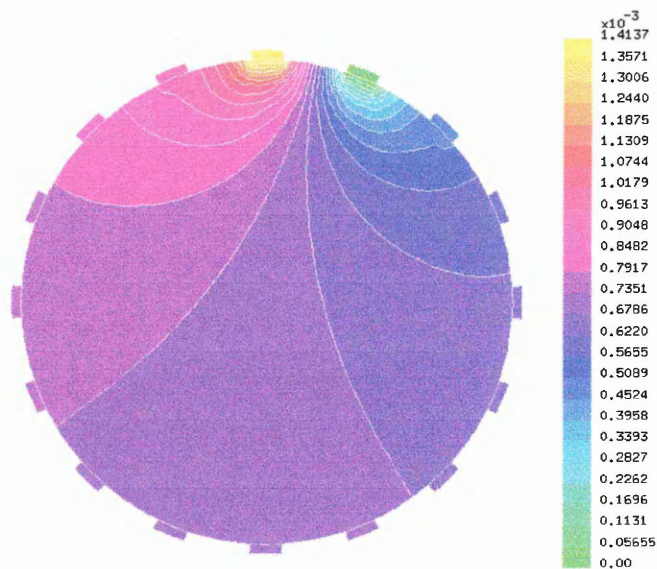


**Figure 3.4. Equipotential plots for a uniform model.**

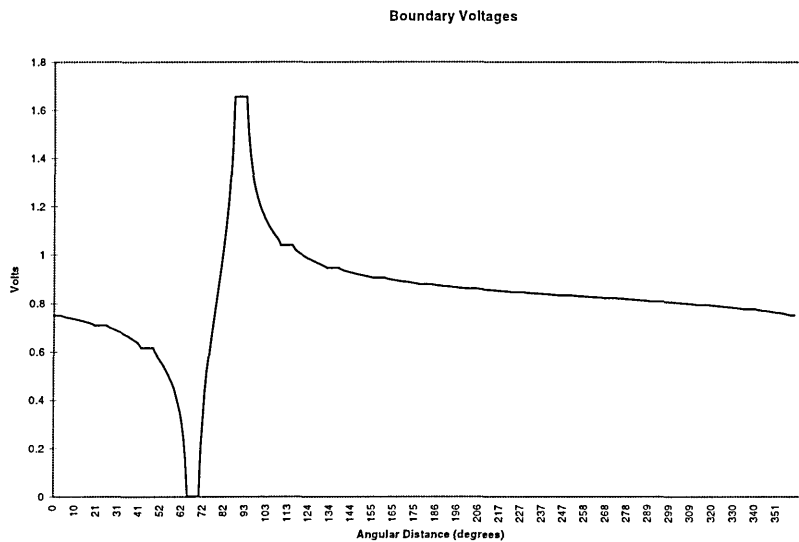


**Figure 3.5. Boundary voltage distribution for a uniform model.**

The minimum voltage value corresponds to the ground electrode, Figure 3.3, and the maximum voltage corresponds to the source electrode. Since a constant current source is used, the voltage value at the source electrode depends on the total conductivity of the system. For a higher conductivity, a smaller voltage would be developed and for a smaller total conductivity, a larger potential will be seen at the source electrode.

As well as the voltages that are obtained, other variables that are useful can be extracted. Current density throughout the model is useful, as it generates and displays the current pattern and paths within the model. The current density of the uniform model is shown in Figure 3.6. Information can be seen visually at this stage, in particular, the shorting effects that the electrodes have on the current flow. Such effects are discussed later. The second is the electric field distribution, Figure 3.7. It is also useful in understanding the effects that various anomalies of different electrical properties have on an EIT system. All vector quantities are given at the Gaussian (central) point within the element.

Plots shown in Figure 3.6 and 3.7 are for two quantities that are proportionally related. Current density is equal to the electric field multiplied by the conductivity for a given pixel. Therefore the two plots shown are virtually the same, except for the variable

scaling depending on the conductivity of the element. For example, the electrodes have a very high conductivity, and the current density within them are seen as more significant than the electric field.

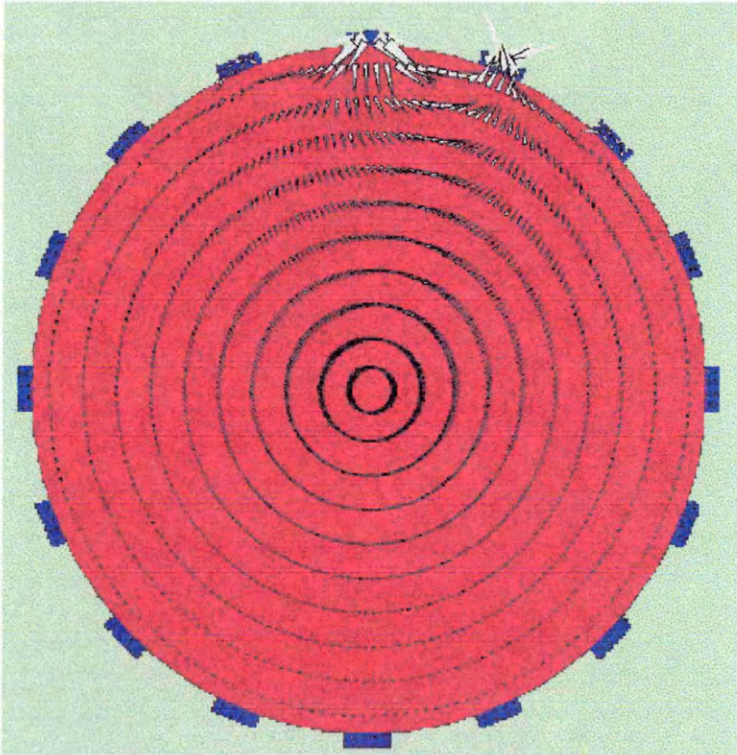


Figure 3.6. Current density plot for a uniform phantom

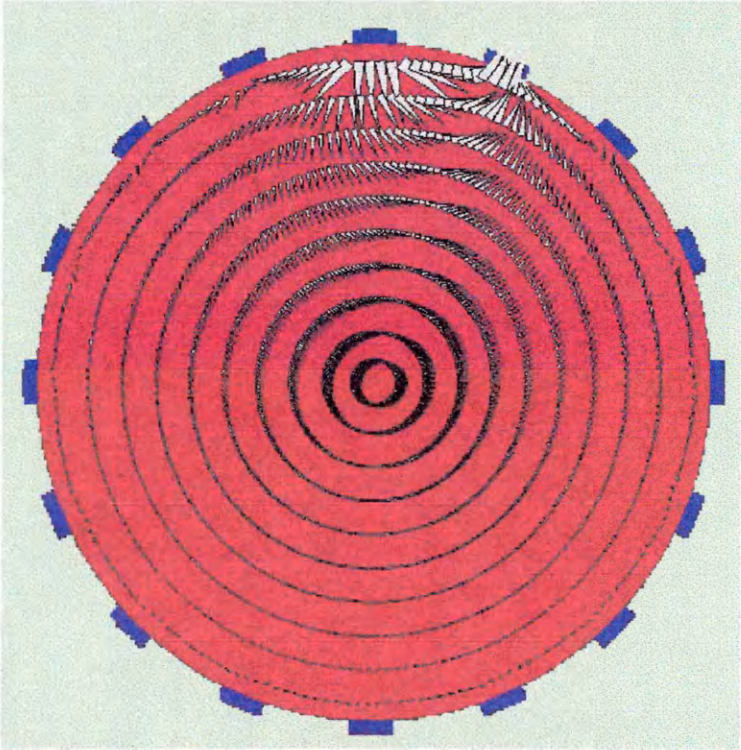
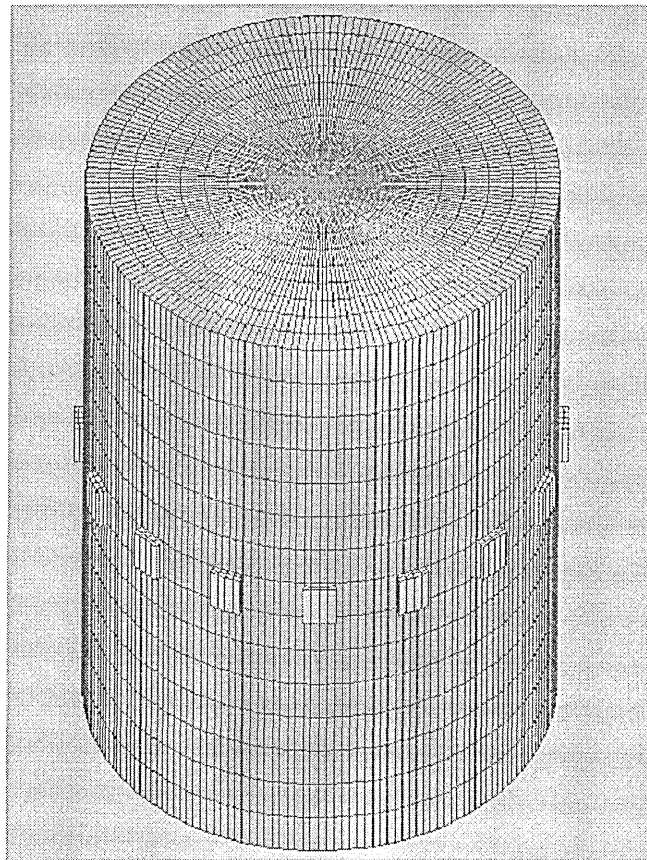


Figure 3.7. Electric field plot for a uniform phantom

### 3.3 The 3D model

The model shown so far has been a 2D model, describing a slice through a 3D object. For the purpose of any 3D model analysis, the same model can be extruded in the 3<sup>rd</sup> dimension, so that analysis can be more accurately defined. An example is shown in Figure 3.8. The dimensions of this 3D model are as for the 2D model, but the model now contains a 3<sup>rd</sup> dimension, its length. The length in this example has been set to twice its diameter.

After solving of the 3D model, the extractable variables are as they were discussed for the 2D model, with the addition that now, there are many planes to investigate, rather than just the previous single plane.



**Figure 3.8. A 3D cylindrical model of phantom**

### **3.4 Discussions of model construction**

Modelling stages using the FEM software have been described. Extractable solutions of an EIT model have been presented and these solutions will next be used for analysis of the performance of an EIT system.

### **3.5 Measures of Performance**

#### **3.5.1 Introduction**

In EIT we aim to visualise the internal regions of a system, the human body in case of medical EIT, by means of non-invasive external measurements. Current passes through the body in a path determined by the varying conductivity of internal organs, and this results in voltage changes measured on the surface. The performance of a single frequency EIT system can be measured in terms of spatial resolution, conductivity resolution and conductivity contrast. In this section, the concept of conductivity contrast and resolution will be defined and calculated for a given model.

In EIT we also aim to maximise the boundary voltage change due to a change in the internal conductivity distribution of a region within the body being imaged (for example an anomaly placed within a uniform region). This enables the conductivity change to be detected more easily in relation to its background. There are factors that a user can change to achieve this maximisation, for example the injected current pattern and the electrode configuration. There are however, three variables outside the users control that can influence this change in boundary voltages, the first being the actual change in conductivity (anomaly conductivity) the second being the size of the anomaly and the third being the actual position of the anomaly within the region of interest. The first two variables are compared to the size and conductivity of the uniform un-perturbed region to give an indication of their influence.

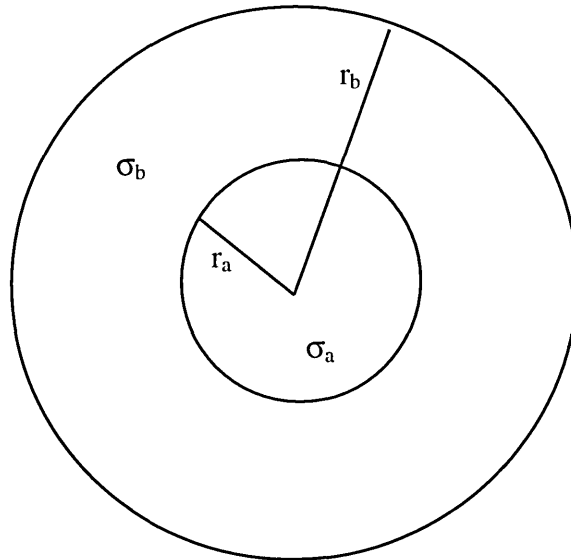


**Figure 3.9. Circular object with co-central circular anomaly**

Seagar et al (1987) defined three parameters. From Figure 3.9:

1. The spatial resolution is defined as the smallest region of a medium in which the conductivity can be independently determined, equation (3.1).

$$\text{Spatial resolution} = \frac{r_a}{r_b} \quad (3.1)$$

2. The conductivity contrast is the ratio between the conductivity of an anomaly to that of its surrounding (background) region, equation (3.2).

$$\text{Conductivity contrast} = \alpha = \frac{\sigma_a}{\sigma_b} \quad (3.2)$$

3. The conductivity resolution is defined as the fractional change in conductivity contrast, equation (3.3).

$$\text{Conductivity resolution} = \frac{\delta\sigma_a}{\alpha} \quad (3.3)$$

Limits of the spatial and conductivity resolution are mainly determined by measurement errors such as movement artefacts and electrode location errors as well as instrumentation noise.

### **3.5.2 Visibility**

The visibility of an anomaly is a measure of the departure of the boundary voltages from those of a uniform body. If a region is uniform, visibility is zero. Visibility  $Q$  for a single projection is defined by Seagar et al (1987) and Basarab-Horwath et al (1995) as:

$$Q = \frac{1}{N} \sum_{i=1}^N q_i \quad (3.4)$$

where:

$$q_i = \frac{[dV_i - dV_{ui}]}{[dV_i + dV_{ui}]} \quad (3.5)$$

$dV_i$  is the  $i^{\text{th}}$  differential voltage between adjacent electrodes of the model with an anomaly present,  $dV_{ui}$  is the corresponding differential voltage for a uniform phantom or model and  $N$  is the number of differential voltages for a given voltage profile.

In order to investigate the visibility in an EIT system, from equations (3.4) and (3.5), the differential boundary voltages for an un-perturbed uniform phantom, and the differential boundary voltages with the presence of an anomaly, (a perturbation in conductivity in a given region within a phantom) are needed. A numerical model, using FEM method already discussed, was used to calculate these voltages. The advantage of such method is that the results are free of measurement noise and error, however they may contain small computational errors dependent on the model used. This will therefore result in values which closely represent an ideal EIT system.

The FEM model already described, a uniform circular model with a diameter of 10 cm consisting of saline, was solved and boundary voltages were calculated for this uniform model, Figure 3.10(a). From this  $dV_{Uj}$ , the differential voltage for a uniform model in equation (3.5) was calculated for the adjacent electrode configuration. Then circular anomalies of radius  $R_a = 1.5, 3.5,$  and  $4.5$  cm were modelled co-centrally in the uniform phantom, and they were each solved for conductivity ranging from  $100 \text{ Sm}^{-1}$  to  $0.01 \text{ Sm}^{-1}$ . Figure 3.10(b) - (d) shows the geometrical properties of these models that were then used to calculate the  $dV_i$ , the  $i^{\text{th}}$  differential voltage of the model with an anomaly present for equation (3.5).

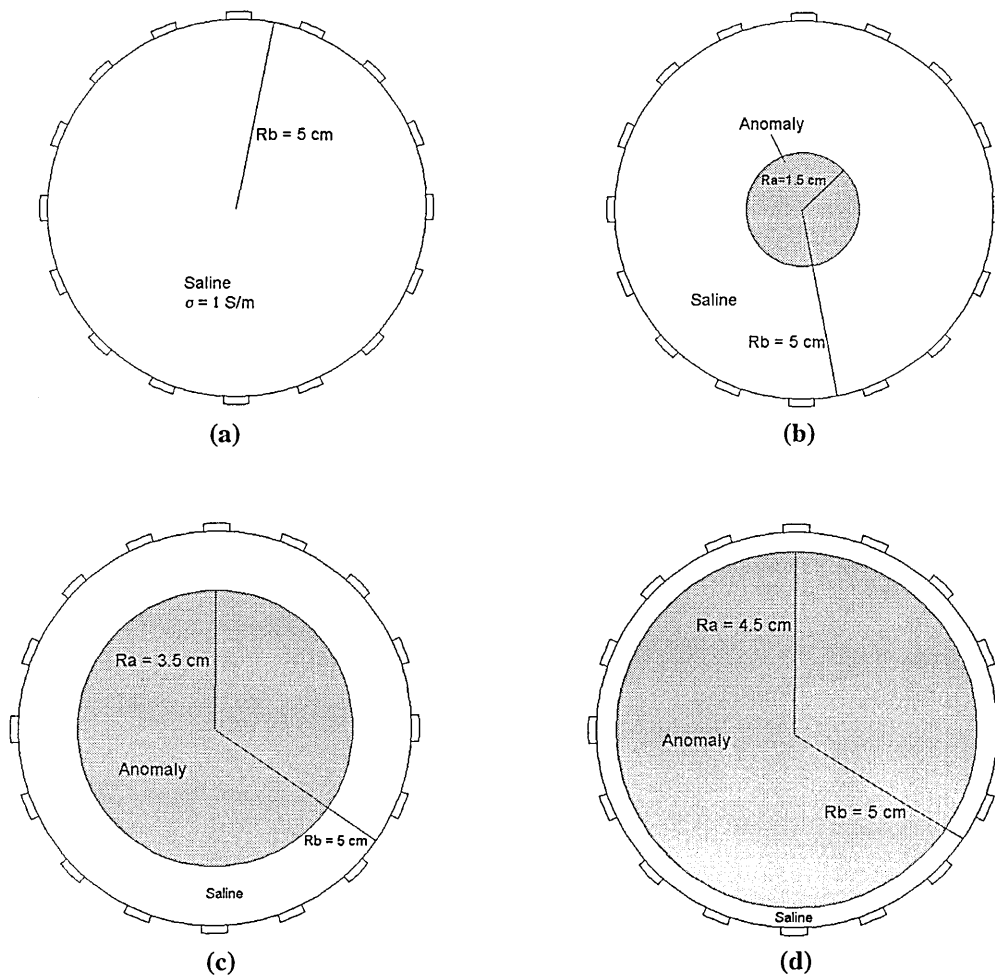


**Figure 3.10.** (a) A uniform phantom together with 3 different sized centrally placed anomalies, (b)  $R_a = 1.5$  cm, (c)  $R_a = 3.5$  cm, (d)  $R_a = 4.5$  cm.

Figure 3.11, shows visibility,  $Q$ , calculated for these anomalies. These results are as expected and confirm the previous findings of Seagar et al (1987) and Basarab-Horwath et al (1995).

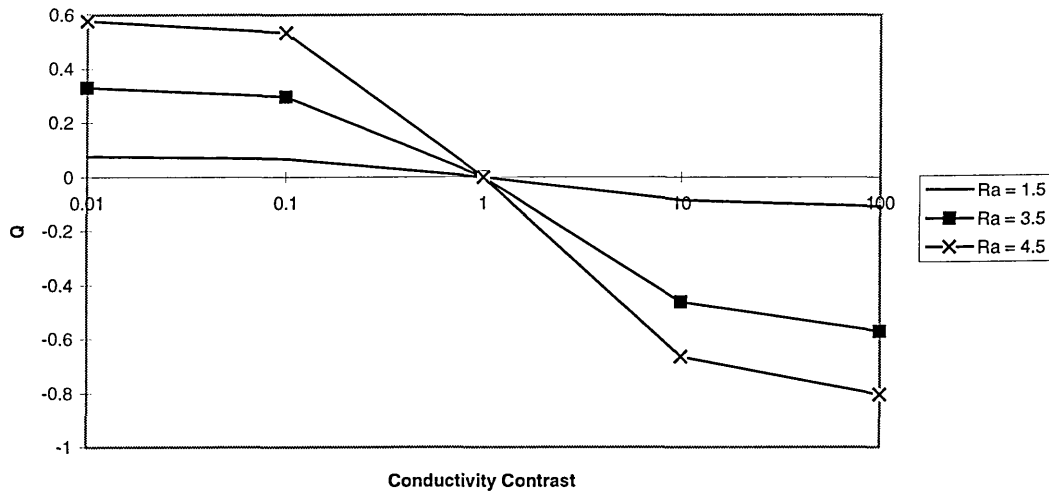


**Figure 3.11.** The visibility  $Q$  for anomalies of  $R_a = 1.5, 3.5, 4.5$  cm, and  $\sigma = 100, 10, 1, 0.1$ , and  $0.01 \text{ Sm}^{-1}$ .

From Figure 3.11 several features are evident. First, when an anomaly of any size, has a conductivity that is equal to that of its background, its visibility is zero. This is expected, as when an anomaly's conductivity is the same as background it would be as if no anomaly is present. Second, a conductive anomaly has negative visibility where as an insulating anomaly has a positive visibility. This is advantageous, since it is possible to determine from  $Q$  values, whether an anomaly is conductive or insulative, by just considering the sign of  $Q$ . Third, it is evident that a conductive anomaly of a given radius, is more visible than one of exactly the same radius but with reciprocal conductivity. Table 3.2 shows the visibility values that were calculated for the above models, which were also used in Figure 3.11.

**Table 3.2. Visibility values Q for three anomalies of various conductivity values.**

	$R_a = 1.5 \text{ cm}$	$R_a = 3.5 \text{ cm}$	$R_a = 4.5 \text{ cm}$
Conductivity = $0.01 \text{ Sm}^{-1}$	$Q = 0.076208$	$Q = 0.330354$	$Q = 0.577969$
Conductivity = $0.1 \text{ Sm}^{-1}$	$Q = 0.065278$	$Q = 0.296133$	$Q = 0.532179$
Conductivity = $1 \text{ Sm}^{-1}$	$Q = 0$	$Q = 0$	$Q = 0$
Conductivity = $10 \text{ Sm}^{-1}$	$Q = -0.08711$	$Q = -0.46094$	$Q = -0.66443$
Conductivity = $100 \text{ Sm}^{-1}$	$Q = -0.1078$	$Q = -0.57102$	$Q = -0.80461$

As an example, for an anomaly of radius  $R_a = 4.5 \text{ cm}$ , of conductivity value of  $\sigma = 100 \text{ Sm}^{-1}$ , placed in a phantom of radius  $R_b = 5 \text{ cm}$  filled with saline of conductivity  $\sigma = 1 \text{ Sm}^{-1}$ ,  $Q = -0.80461$ , compared with an anomaly of the same size but with conductivity value of  $\sigma = 0.01 \text{ Sm}^{-1}$ , where  $Q = 0.577969$ . This has been previously reported by Basarab-Horwath et al (1995) and Basarab-Horwath and Dehghani (1998).

Consider equation (3.5). If at a given boundary measurement point, the differential voltages are such that the term  $q_i$  is negative, while at another measurement point it is found to be positive, there will be some effects of cancellation when the calculated  $q_i$  is summed for all points in equation (3.4) for the calculation of  $Q$ . It is for this reason that a new measure of visibility  $G$  is proposed (Basarab-Horwath and Dehghani 1998), where  $G$  is given by:

$$G^2 = \frac{1}{N} \sum_{i=1}^N g_i^2 \quad (3.6)$$

where:

$$g_i = \frac{[dV_i - dV_{ui}]}{dV_{ui}} \quad (3.7)$$

the  $i^{\text{th}}$  fractional change in boundary voltage.  $G$  is the RMS value of the fractional change in differential voltage due to an anomaly and therefore has more physical significance than  $Q$ .

Table 3.3 shows the corresponding calculated G values which are also plotted in Figure 3.12. It is observed now that all values of visibility G are positive. Also as with previous visibility factor, anomalies of any size with a conductivity same as background are found to have zero visibility. The major difference is now however, the insulative anomalies are found to be more visible than anomalies of same size, but with reciprocal conductivity. Larger anomalies are more visible than smaller anomalies.

**Table 3.3. Visibility values G for three anomalies of various conductivity values.**

	$R_a = 1.5 \text{ cm}$	$R_a = 3.5 \text{ cm}$	$R_a = 4.5 \text{ cm}$
Conductivity = $0.01 \text{ Sm}^{-1}$	$G = 0.041146$	$G = 0.324938$	$G = 1.193291$
Conductivity = $0.1 \text{ Sm}^{-1}$	$G = 0.033865$	$G = 0.233996$	$G = 0.638507$
Conductivity = $1 \text{ Sm}^{-1}$	$G = 0$	$G = 0$	$G = 0$
Conductivity = $10 \text{ Sm}^{-1}$	$G = 0.029681$	$G = 0.102159$	$G = 0.158305$
Conductivity = $100 \text{ Sm}^{-1}$	$G = 0.035131$	$G = 0.116452$	$G = 0.176545$

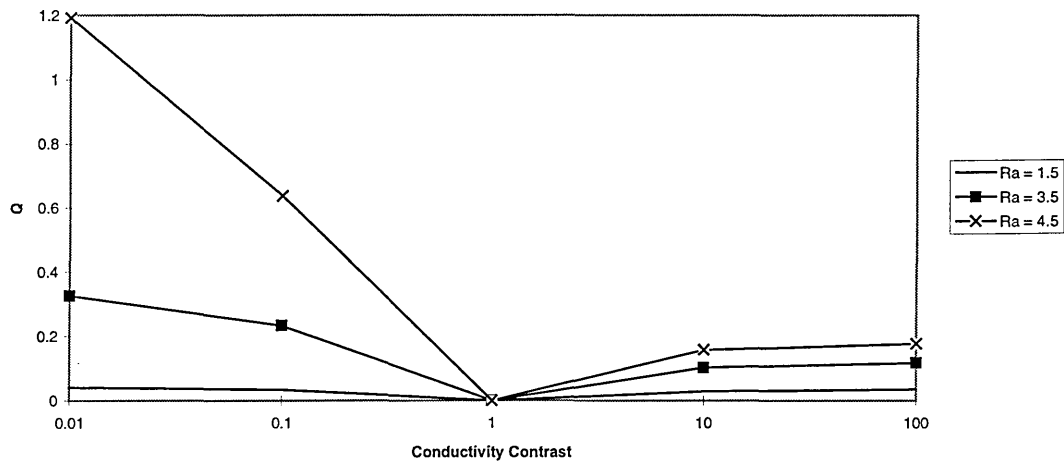


**Figure 3.12. The visibility G for anomalies of  $R_a = 1.5 \text{ cm}$ ,  $3.5 \text{ cm}$ ,  $4.5 \text{ cm}$ , and  $\sigma = 100, 10, 1, 0.1$ , and  $0.01 \text{ Sm}^{-1}$ .**

This new measure of visibility, G, is an RMS value and has a more physical meaning than the previously defined measure, Q. These results show, that at a single frequency, for a purely conductive anomaly, i.e. not permittive or permeable, an anomaly with a conductivity less than background is more visible than one with same geometry, but with reciprocal conductivity. Furthermore, it confirms previously findings that larger anomalies are more visible than smaller anomalies. However, some information is lost

in this new measure. From the calculated  $Q$  values, it is possible to decide whether an anomaly is resistive or conductive, by just considering the sign of  $Q$ . Since  $G$  is an RMS value, and always positive, this information is lost.

It is not usually important to obtain information to see whether an anomaly is conductive or insulative, since in forward modelling these known anomalies are either physically placed in a phantom for measurement collection, or are modelled numerically as done here. It is more important to understand the behaviour of the system. It must be considered which measure of visibility is more accurate, since  $Q$  shows that a conductive anomaly is more visible than one with same size but with reciprocal conductivity  $G$  shows the opposite case.

There are possible situations where the presence of a conductive anomaly will produce differential boundary measurements which when used to calculate  $Q$  will produce zero visibility. This will be due to addition of equal but positive and negative in magnitude measurements. The same data used to calculate  $G$ , will however produce a non-zero visibility values. It is to this effect that  $Q$  is considered inaccurate, and the new proposed visibility  $G$  is considered as a more suitable replacement.

So far only the effect of conductivity on the visibility of anomalies within a single frequency has been studied. For purely conductive materials, frequency has no effect on the total impedance seen. The total voltage seen at the face of an electrode will depend on the total current applied, regardless of its frequency. Most materials however, are not purely conductive. In process tomography, there maybe a situation where permeable metals are under investigation. In medical tomography, biological tissue have a very high permittivity. It is generally known that impedance of biological tissue decreases as frequency increases (Blad 1994, Osypka and Gersing 1995). This is due to the permittivity of biological tissue, as frequency increases more current penetrate intracellular fluids of the cells and hence reduce impedance. At higher frequencies, displacement currents become significant. In a situation where metallic conductors are under investigation, eddy currents are present, which give rise to skin effect (Hammond

and Sykulski 1994). The skin effect will cause the total impedance of a conductor to increase, by confining the current only to the outer skin of the conductor.

In order to investigate these effects, the numerical method must be able to account for both displacement current and eddy current as well as conduction current. As discussed earlier, the FEM software used for this work is capable of such requirements. In the following sections the effect of frequency on visibility of permittive and permeable material is investigated.

### **3.5.2.1 Frequency and permeability**

Eddy currents are generated in a plane perpendicular to the plane of the conduction current. In order to study the effects due to eddy currents the use of a 3D model is necessary to allow for their consideration. In order to investigate the effect of frequency on the visibility of an EIT system, a 3D uniform model with a radius of 5 cm and thickness of 1 cm was constructed as shown in Figure 3.13. The material property within the uniform model were set as  $\sigma_1 = 1 \text{ Sm}^{-1}$  and  $\mu_1 = 10$  where  $\sigma_1$  is the conductivity and  $\mu_1$  is the relative permeability. A constant current of 1 mA was used in a adjacent drive/receive combination.

The equations set to be solved for this problem are now as discussed previously, equations (2.11) - (2.13) of section 2.4.

Boundary voltages were calculated over a range of frequencies, from 1 Hz to 1 MHz. Absolute amplitude of differential boundary voltages were obtained using FEM and visibility Q and G were calculated for each frequency with reference to the lowest frequency measurement, i.e. in equations (3.5) and (3.7) the term  $dV_{\text{uij}}$  is the differential boundary voltage for a uniform phantom at 1 Hz.

Table 3.4 shows the calculated visibility values and a plot of these values are shown in Figure 3.14.

**Table 3.4. Visibility values Q and G for a uniform model over a range of frequency**

	Visibility Q	Visibility G
1 Hz	0	0
1 kHz	5.74E-09	6.34E-08
10 kHz	5.03E-07	1.15E-06
20 kHz	2E-06	4.57E-06
40 kHz	7.92E-06	1.81E-05
80 kHz	3.06E-05	6.98E-05
160 kHz	0.000108	0.000248
320 kHz	0.000321	0.000738
640 kHz	0.000788	0.001834
1 MHz	0.001324	0.003128

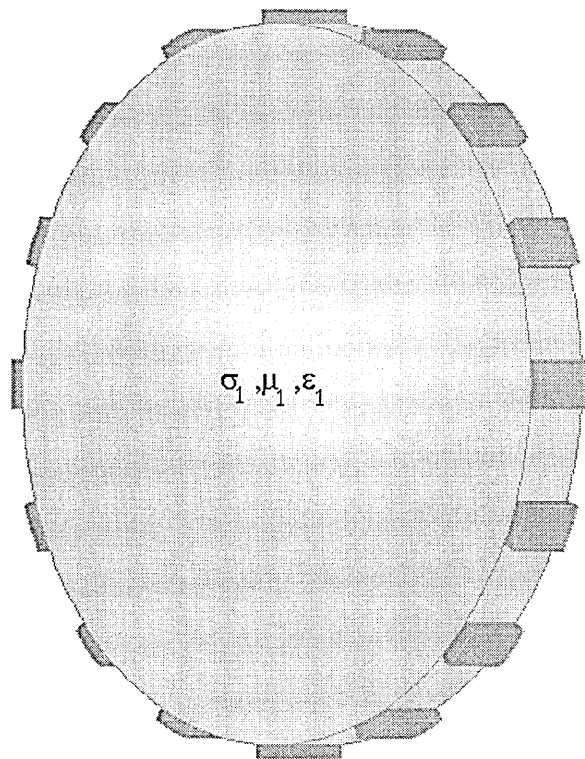


**Figure 3.13. Uniform model containing conductive, permittive permeable uniform material.**

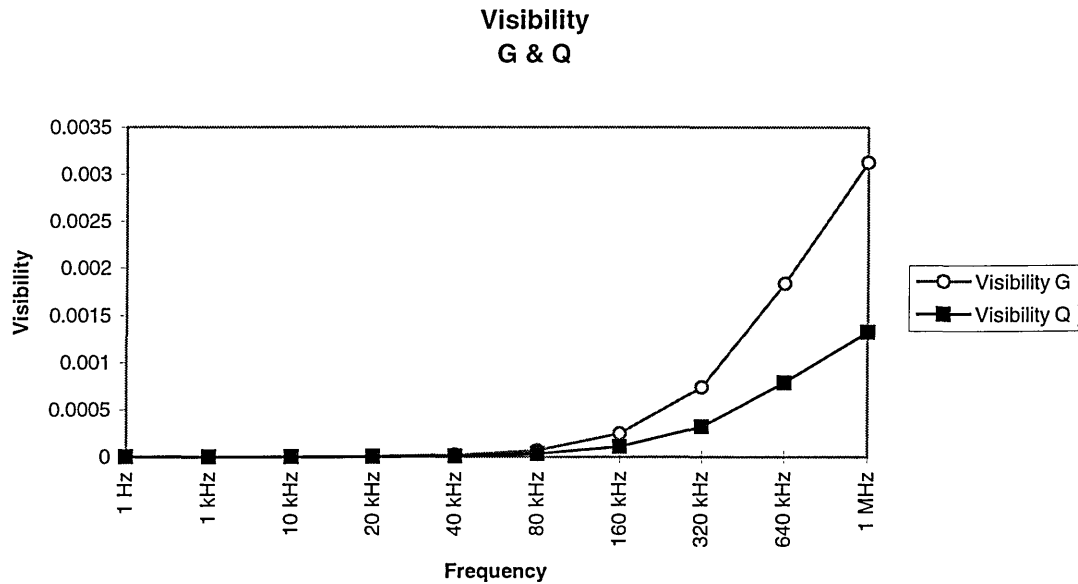


**Figure 3.14.** Plot of visibility Q and G as a function of frequency for a permeable uniform model.

From Table 3.4 and Figure 3.14 it can be observed that, the visibility of the EIT system appears to increase with frequency, with effect seen initially at a frequency of 40 kHz. From values of Q it is evident that the system is appearing more insulative than it actually is. This is due to the skin effect mentioned earlier.

Induced eddy currents within a region are effected by the object's conductivity, magnetic permeability and the applied frequency. When eddy currents are present the electric field will only penetrate a certain distance into the object, known as skin depth ( $\delta$ ). The conduction current will be at a maximum in this skin depth  $\delta$  which is given by

$$\delta = \sqrt{\frac{2}{\mu\omega\sigma}} \tag{3.8}$$

Equation (3.8) expresses that, as frequency increases for a material with high conductivity and permeability, the skin depth decreases and conduction current penetrates less into the material. This would cause the material to appear more resistive.

Using equation (3.8) at a frequency of 20 kHz, the skin depth of the uniform model is given by:

$$\delta = \sqrt{\frac{2}{1.2566 \times 10^{-6} \times 10 \times 2 \times \pi \times 20000 \times 1}} = 1.125m \quad (3.9)$$

and at a frequency of 1 MHz:

$$\delta = \sqrt{\frac{2}{1.2566 \times 10^{-6} \times 10 \times 2 \times \pi \times 1 \times 10^6 \times 1}} = 0.159m \quad (3.10)$$

It can be observed that at a higher frequency, the skin depth has decreased to approximately 16 cm. The phantom has only a radius of 5 cm, but clearly the effect of skin depth can be seen. It is also evident from results in Table 3.4 that the visibility values are very small, compared to the values seen in pure conductors, Table 3.2 and 3.3. It must be mentioned that the visibility values calculated here are not strictly comparable to those in earlier sections. Visibility values are those usually defined for anomalies within uniform phantoms. Here, we are comparing uniform phantom at one frequency with a like phantom at another frequency. The calculated visibility is therefore not for a given anomaly, but for the entire system. In differential imaging the changes seen here would result in a distributed ‘bowl’ shaped image of conductivity where the central region will appear more insulative.

The permeability values used here are smaller than that of anomalies which can be seen in a process tomography system, for example steel, but this thesis will concentrate on medical tomography applications only.

### **3.5.2.2 Frequency and permittivity**

In order to investigate the effects of permittivity on visibility, a 2D uniform model of radius  $R_b = 5$  cm was constructed with a central anomaly of radius  $R_a = 0.5$  cm, as shown in Figure 3.15. The property of the material within the uniform model were set as  $\sigma_2 = 1 \text{ Sm}^{-1}$ ,  $\mu_2 = 10$ , and  $\epsilon_2 = 200$ , where  $\sigma$  is the conductivity,  $\mu$  is the relative permeability and  $\epsilon$  is the relative permittivity.

The equations to be solved for the solution of this problem are as previously stated for conduction and displacement currents, equations (2.14) in section 2.4.

For the anomaly, the material property were set equal to the background, except the permittivity value  $\epsilon_1$  was changed so that the permittivity contrast given as:

$$\text{Permittivity contrast} = \frac{\epsilon_1}{\epsilon_2} \quad (3.11)$$

was varied from 10 to 160, at 4 different frequencies of dc, 100 kHz, 500 kHz and 1 MHz.

Boundary voltage measurements were obtained and from these visibility G and Q were calculated.

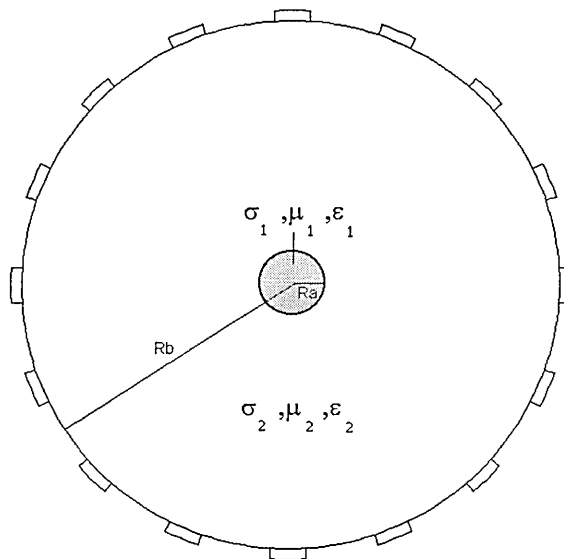


**Figure 3.15. Model used to investigate effects of frequency and permittivity on visibility**

Visibility Q and G were calculated with a uniform model at DC being used to calculate the term the term  $dV_{ui}$  in equations (3.5) and (3.7). The calculated visibility is shown in Figure 3.16 and a Table 3.5.

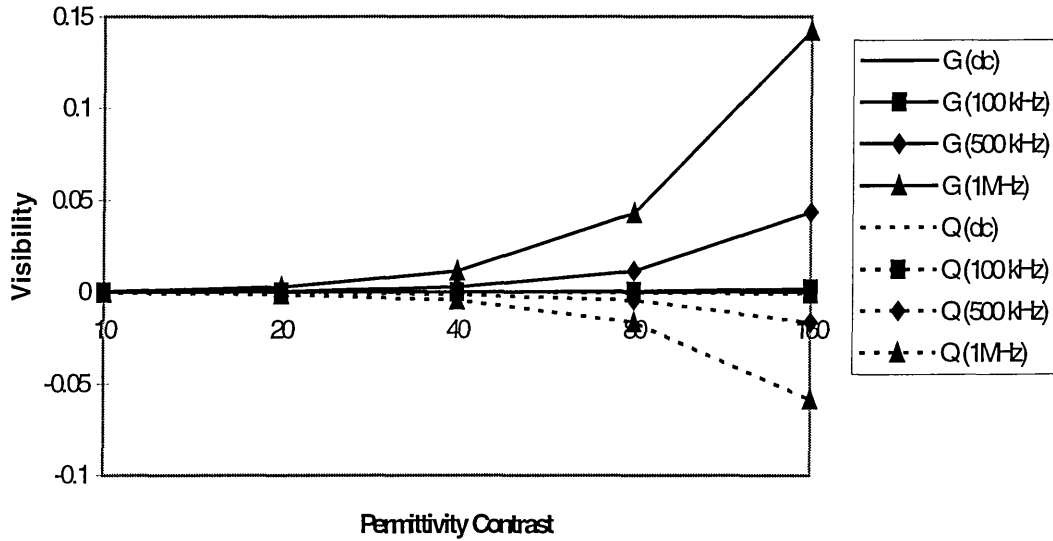


Figure 3.16. Visibility as a function of permittivity and frequency.

Table 3.5. Values of visibility Q and G as a function of frequency and permittivity

	Visibility Q				DC	Visibility G		
	DC	100 kHz	500 kHz	1 MHz		100kHz	500kHz	1MHz
Permittivity contrast = 10	0	-2.6E-06	-6.5E-05	-0.00026	0	6.98E-06	0.00017	0.00070
Permittivity contrast = 20	0	-1.1E-05	-0.0003	-0.00105	0	2.86E-05	0.00071	0.00284
Permittivity contrast = 40	0	-4.3E-05	-0.0011	-0.00422	0	0.000116	0.00288	0.01133
Permittivity contrast = 80	0	-0.0002	-0.0043	-0.01645	0	0.000464	0.01140	0.04310
Permittivity contrast = 160	0	-0.0007	-0.0165	-0.05865	0	0.001858	0.04323	0.14210

It is observed from the results shown in Figure 3.16 and Table 3.5 that as the permittivity contrast increases, for any given frequency, the visibility also increases. The exceptional case is dc, where at zero frequency, no displacement currents are present, and hence no effects due to material permittivity are seen. From Q values it can be noted that the more permittive the material is, the higher its conductivity appears. This is due to the large displacement currents present. Also, for a given permittivity

contrast, as frequency increases, the visibility increases, showing a more 'conducting' behaviour.

### **3.5.2.3 Discussions of effects of visibility with frequency**

FEM has been used to investigate a measure of performance, visibility, in an EIT system. The FEM method used, has allowed for the first time the effects of displacement and eddy currents to be modelled as well as the conduction current. The initial study confirmed previous studies of visibility of conductive anomalies, but it has potential for misinterpretation. A new measure of visibility,  $G$ , has been proposed, where  $G$  is an RMS value, rather than the mean, and has therefore a more significant physical meaning. It was shown that unlike previous findings, an insulator is in fact more visible than a conductor of same size and reciprocal conductivity. One disadvantage of the new visibility measure,  $G$ , is the fact that insulators and conductors can no longer be separated by the calculated visibility value.  $Q$  is positive for all insulators, and negative for all conductors, where as  $G$  is always positive.

In medical EIT, biological tissues have a much higher permittivity than permeability (Weast 1989). Further experiments performed investigated the effect of permeability of a uniform model over a range of frequencies on the visibility of an EIT system. It was found that visibility  $G$  increased with frequency, and visibility  $Q$  indicated that this increase in visibility as showing the saline to appear more insulative than it actually is. This increase in visibility can be explained by the phenomenon known as the skin-effect, where at high frequencies in permeable material, the conducting current is confined to the outermost layer of the conductor, whose depth is given by equation (3.8). This skin-effect is a direct result of the eddy currents generated in the permeable material (Hammond and Sykulski 1994).

In the final study, the effect of permittivity of an anomaly over a range of frequency was investigated. An anomaly whose conductivity was equal to the background, but with varied permittivity was used over a range of frequencies. Calculated measures of visibility showed that the anomaly at higher frequencies appeared to be more

conductive than the background. This change in visibility is due to the presence of displacement currents in permittive material at high frequencies.

Since biological tissues have a larger permittivity than permeability, and the change in visibility in permittive material is more significant than the change in permeable materials, it is therefore concluded that in medical tomography, the modelling of displacement currents is more significant than the modelling of eddy currents. Displacement currents have been taken into consideration, and have been shown here to be of importance. Modelling of eddy currents in an EIT system is therefore found to be non-essential, where as the modelling of displacement currents is shown to be necessary.

### **3.5.3 Visibility and electrode width**

In EIT, boundary voltages are measured from the surface of an object by the use of electrodes. The electrodes usually are the conventional ECG electrodes used for monitoring the electrical activity of the heart. The size of the electrodes used is determined by the geometry of the region being imaged. If the region has a small circumference, small electrodes may needed. The effect of the size of the electrodes used will be discussed here, together with their effects on the visibility of an EIT system.

A uniform model containing saline of conductivity  $1 \text{ Sm}^{-1}$  was used. The modelled electrodes were of conductivity  $10000 \text{ Sm}^{-1}$  and for each simulation their width was varied, from 1.875 degrees to 18.75 degrees of the outermost circumference of the circular model. The electrodes had a thickness of 2 mm, and the analysis was at zero frequency. A constant current of 1 mA was used.

Visibility (G) was calculated for each electrode width, Figure 3.17. The differential boundary voltages from the smallest electrode width (1.875 degrees) were used as the reference ( $dV_{ui}$ ) for these calculations.

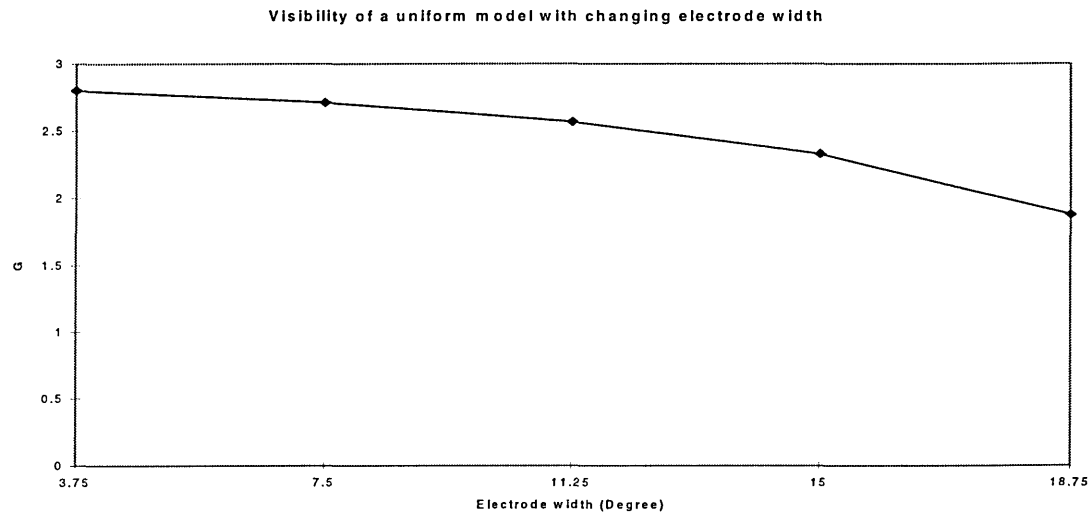
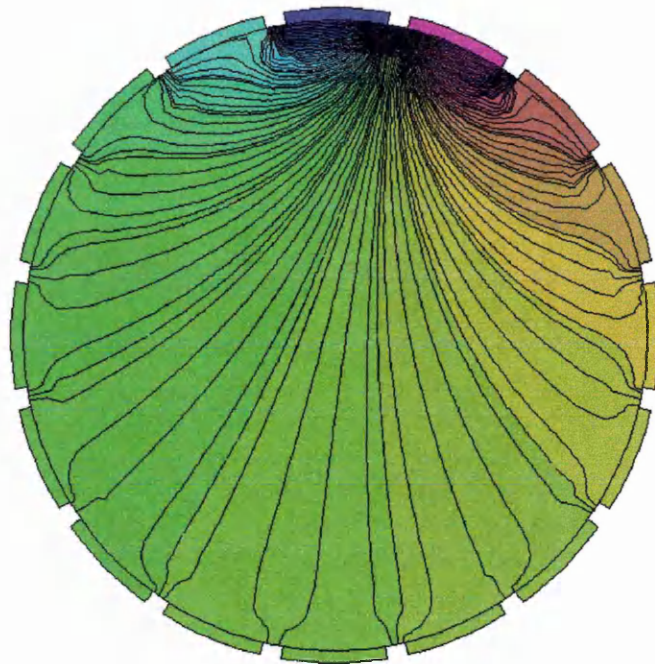


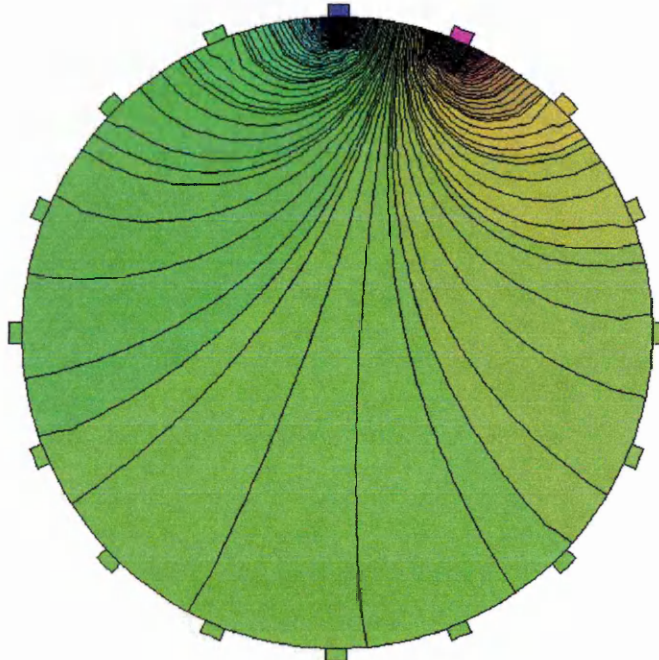
**Figure 3.17. Visibility of a uniform model with changing electrode width**

Visibility is normally used to describe the behaviour due an anomaly. Here again, visibility is used to define the behaviour of a model with uniformly distributed conductivity. This again will not be strictly comparable to the case where visibility is calculated in the presence of an anomaly within the uniform conductivity distribution.

It is seen that with increasing electrode width, the visibility of the system is reduced. A simple explanation can be provided by Figure 3.18 and 3.19. In Figure 3.18, the equipotential plots of two uniform models with different electrode width are shown. The model with largest electrodes shows distorted equipotentials, whereas the model with smaller electrodes does not.



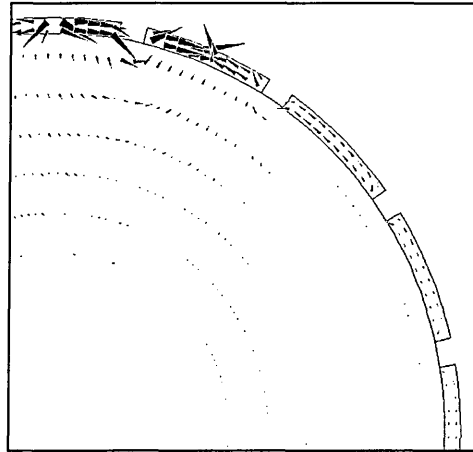
(a)



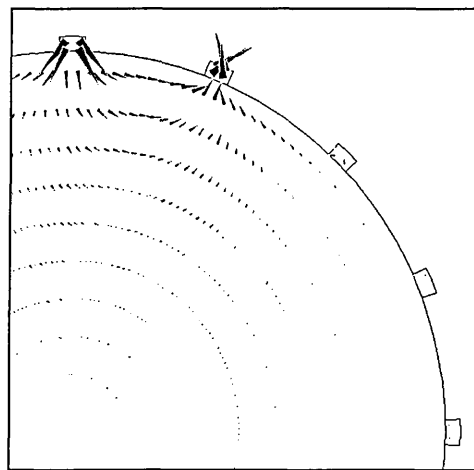
(b)

Figure 3.18. Equipotential plots for two uniform models, with (a) electrodes of 18.75 degrees width, and (b) electrodes of 3.75 degrees width.

In Figure 3.19, the current density of a portion of the models seen in Figure 3.18 are shown. What can be seen here, is that the larger electrodes due to their high conductivity are shunting the current in the model. The larger the electrode width, the higher the shunting effect. For smaller electrodes, the shunting is much smaller, hence the calculated visibility is larger.



(a)



(b)

**Figure 3.19. Current density plots for two uniform models, with (a) electrodes of 18.75 degrees width, and (b) electrodes of 3.75 degrees width.**

### 3.5.3.1 Discussion

Smaller electrodes provide a better performance in EIT than larger electrodes because of higher current density in area of electrode / body contact, lower contact impedance and less current shunting. This has been shown by the current shunting visible from current density plots of the models. It therefore, stresses the importance of modelling of electrodes in an EIT system.

### 3.6 Visibility in a 3D model

A 3D cylindrical model as shown in Figure 3.20, was constructed which consisted of a uniform region containing saline of conductivity  $1 \text{ Sm}^{-1}$ . The model dimensions are as before, i.e. radius = 5 cm, and now the model has a length = 15 cm. An anomaly of radius = 2.5 cm and thickness of 1 cm was modelled co-centrally within the cylindrical tank and had a conductivity of  $0.1 \text{ Sm}^{-1}$ .

Visibility was calculated, at each step, as the anomaly was displaced along the length of the cylinder. A plot of the calculated visibility,  $G$ , is shown in Figure 3.21.

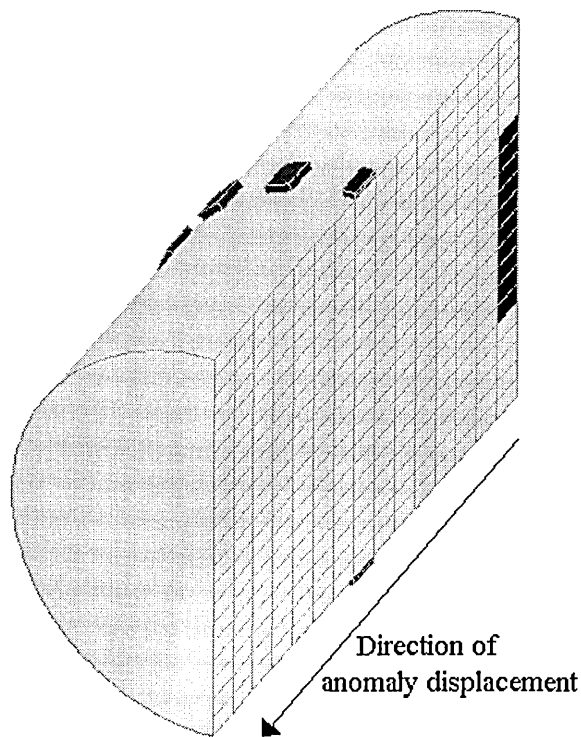


**Figure 3.20. A 3D model showing the direction of anomaly displacement. This figure does not show the actual mesh used in the modelling.**

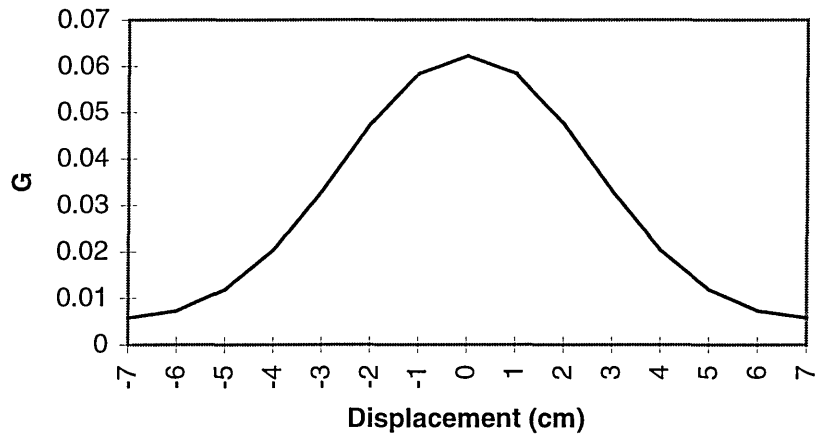


**Figure 3.21 Plot of the calculated visibility for an anomaly as it is displaced through the length of a modelled cylinder.**

From the results shown in Figure 3.21, it can be seen that the off-plane object clearly has an effect on the measured boundary voltages using a set of coplanar electrodes placed around a 3D body. Also it clearly indicates that an anomaly has a larger calculated visibility when it is placed under the measurement electrodes, than when it is in an off plane region. Similar results have been previously published by Metherall et al (1996).

### **3.7 Conclusions**

EIT model construction using FEM has been described for the forward model analysis of a system. Usefulness of solutions of the forward model have been presented in terms of the variables accessible using FEM analysis of an EIT system. Measures of performance in terms of visibility have been presented. Initial results of visibility show good comparison with previous published findings. New measures of visibility has been defined. Visibility due to conductivity, permeability and permittivity of anomalies have been investigated.

The use of an ac simulation, for the first time has demonstrated the effects of permeability and permittivity of materials on the calculated visibility of an EIT system.

Permeable material at high frequency have a skin depth which is dependent on the applied frequency, material permeability and conductivity. It has been shown that permeable material appear more visible and more resistive at higher frequencies. Materials which are permittive, appear more visible and more conductive at higher frequencies, due to the generated displacement currents. However, the effect of permeable materials on visibility is much smaller than that of materials which are permittive. Also since permeable materials are unlikely to be encountered in medical applications of EIT, any such effects are considered insignificant. This will simplify the governing equations that are need to be solved for the system, and hence reduce computation time.

Also the effects of electrode width on the calculated visibility has been demonstrated. A higher visibility is calculated when electrodes with smaller width are used. This is due to the great current shunting effect that has been seen with larger electrodes.

The effect of an off-plane anomaly is shown when data are measured for a 3D model. Off-plane objects clearly can be detected when data are collected using electrodes placed around another section. Also, an anomaly is best detected when the electrodes are placed directly over the region that contains the plane with that anomaly.

The capability of numerical modelling using FEM has been demonstrated. Previous results have been confirmed using the available software package MEGA, and its capability in producing new results is demonstrated.

Finally it must be noted that only centrally placed anomalies were considered in these studies. EIT is point spread variant, i.e. an anomaly of the same size but in an other position within the system will have a different response to measures, and the resolution of the technique improves for increasing radially offset objects.

## Chapter 4

### 4. Single frequency EIT image reconstruction

#### 4.1 Introduction

A typical single frequency EIT system will acquire voltage measurements from the boundary of an object. Although these boundary voltage measurements contain information regarding the internal conductivity distribution under investigation, they are more useful when converted to visual images. A reconstructed image can illustrate either the conductivity distribution within an object being imaged or the normalised conductivity changes from a known reference conductivity.

In this work 16 electrodes have been placed around a circular object. Current is driven into the object through two adjacent (drive) electrodes. For each of the 16 drive-electrode pairs, 13 voltage differences between the remaining adjacent non-current carrying (receive) electrodes are recorded. Within each drive electrode pair combination the current carrying electrode pair are not used for boundary voltage measurements because of the unknown contact impedance, hence allowing only 13 voltage difference measurements rather than the possible 15. In practice objects are three-dimensional (3D); current cannot be confined to one plane. However, the reconstruction algorithm usually assumes that the object is 2D. This work will only deal with proper 2D reconstruction as the processing time is much faster; the principles can be extended to full 3D imaging providing that the third dimension is taken into consideration.

The process of producing images from measured boundary voltage is referred to as image reconstruction. Many methods have been introduced, used and utilised for the purpose of image reconstruction in single frequency EIT. A number of these reconstruction methods will be discussed here.

#### 4.2 Theory

It is reasonable to assume that there exists a relationship between the measured boundary voltages and internal conductivity distribution of the region being imaged since the boundary voltages are a function of the internal conductivity distribution. The

calculation of the boundary voltages from the known conductivity distribution when a known current is injected at a given point in the boundary is known as a forward problem. The calculation of the conductivity distribution from the measured boundary voltages is referred to as an inverse problem. However, there is a non-linear relationship between these two physical quantities and also the problem is ill-posed.

The ill-posed problem arises in *static* imaging where it involves producing an image of the distribution of absolute resistivity. This form of imaging may also be referred to as anatomical imaging since we are differentiating different tissues by their conductivities. The term ill-posed or ill-conditioned means that the reconstructed images are very sensitive to the measured boundary voltage data. A small variation in boundary data may lead to very large changes in the reconstructed conductivity images. If the problem is constrained to dealing with imaging the changes in conductivity, calculated from a change in measured boundary voltage, the effects of geometric discrepancies and electrode placement can be reduced by normalisation of the data (Barber 1990). This form of imaging is known as *dynamic* or *differential* imaging. In differential imaging it is possible to reconstruct images of changes in conductivity, with respect to time or condition, for example, inspiration and expiration, or to image the changes in conductivity over a range of frequencies with reference to another frequency.

In practice there are two types of image reconstruction algorithms utilised in EIT. The first type of reconstruction algorithms are known as *single-step techniques* where images are reconstructed using a single set of mathematical operations. The second type are *iterative techniques* where by the use of repeated operations an estimate of the internal conductivity is made to closely match the true internal conductivity.

#### **4.3 Single-step image reconstruction algorithms**

Single-step methods provide a fast and robust image reconstruction technique in EIT but are only useful in differential imaging where conductivity changes are imaged rather than absolute conductivity. This is because the relationship described by this method only deals with changes with reference to a starting conductivity distribution. Single-step methods calculate internal conductivity changes from a change in the measured boundary voltages by the use of a set of mathematical expressions. If the change in the

measured boundary voltage is represented as a vector,  $\Delta g$ , the multiplication of this vector with a matrix,  $\mathbf{G}^{-1}$ , which represents the reconstruction operator (the set of mathematical equations) will produce a vector containing the changes of conductivity within the model,  $\Delta c$ , equation (4.1).

$$\Delta c = \mathbf{G}^{-1} \Delta g \quad (4.1)$$

Equation (4.1) has previously been discussed as the inverse solution in section 2.1.

### **4.3.1 Backprojection between equipotential lines**

Backprojection between equipotential lines is so called because the normalised change in potential difference between two adjacent electrodes is backprojected along the equipotential lines over the surface of the body to display the conductivity value within that body between those equipotential lines. Blurred images are produced when this step is repeated for all electrode pairs. This method is the basis of image reconstruction in CT and was first described by Barber et al (1983).

Backprojection in EIT is far more complicated than that of CT because:

- (1) The projection paths are not actually parallel or straight, which in turn complicates the design of a filter.
- (2) The projection paths depend on the actual conductivity distribution (soft-field effect).

### **4.3.2 Sensitivity matrix method**

The sensitivity matrix is a matrix of coefficients by which the change in conductivity values of discretised pixels or elements of a region or model can be multiplied to give an approximation of the differential boundary voltages. Referring back to Chapter 2, this idea was originally described as the solution to the forward model and from equation (2.1) is given as equation (4.2):

$$\Delta g = \mathbf{S} \Delta c \quad (4.2)$$

where  $\Delta c$  is a vector of changes in the conductivity values of pixels in the model or region,  $\Delta g$  is a vector containing the corresponding changes in the differential boundary voltages and  $\mathbf{S}$  is a matrix of sensitivity coefficients.

The inverse problem needs to be solved in order to produce images of changes in conductivity from changes in differential boundary voltages; this means that the inverse of matrix  $\mathbf{S}$  needs to be calculated to give:

$$\Delta c = \mathbf{S}^{-1} \Delta g \quad (4.3)$$

The calculation of the inverse of the sensitivity matrix is conceptually very simple but has proved to be very difficult in practice. This technique of image reconstruction is the method utilised for this thesis and will be discussed in detail later in this chapter.

### **4.3.3 Iterative image reconstruction algorithms**

Iterative techniques have been used to try and solve the static reconstruction problem, that is, images of the true conductivity are sought rather than images of change in conductivity from a given reference distribution.

The Newton-Raphson algorithm is an iterative reconstruction algorithm specifically developed for non-linear problems: Yorkey (1986) provide a good description.

The algorithm is best described by the flow chart shown in Figure 4.1. An initial estimate for the conductivity distribution within the region to be imaged is chosen. The forward model is solved for this initial guess of conductivity distribution and the differential boundary voltages are calculated. These boundary voltages are compared to the boundary voltages measured on the object and the error difference is calculated. The aim of this method is to iterate by adjusting the conductivity values in the forward model to minimise the error difference between the measured and the calculated boundary voltages.

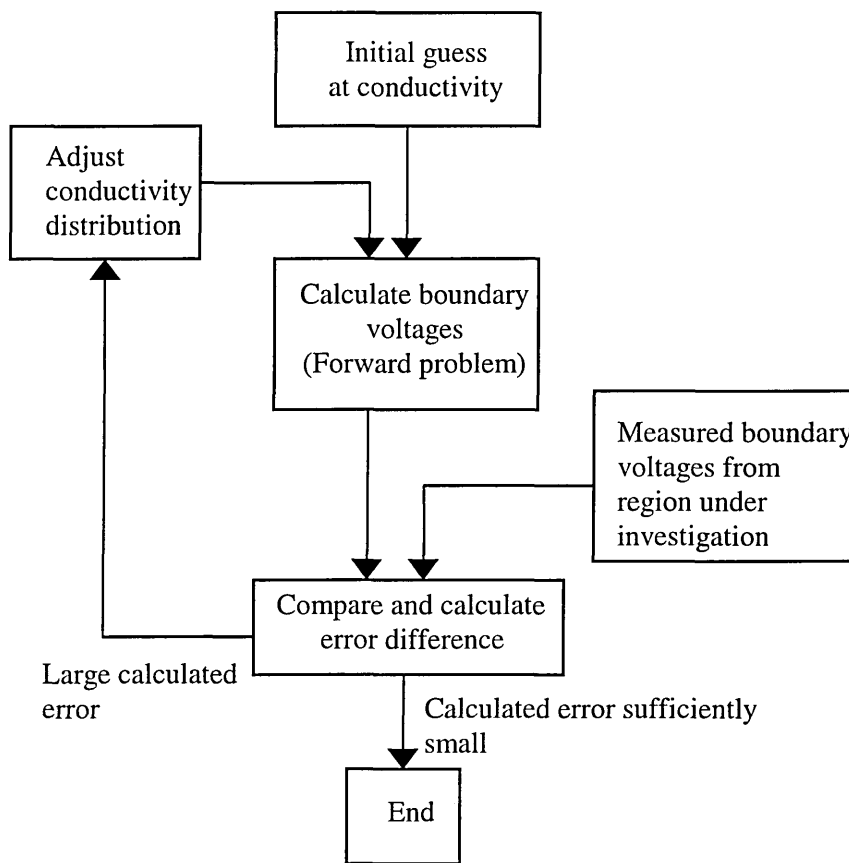


**Figure 4.1. Flow chart of an iterative reconstruction algorithm**

Problems associated with this technique include its sensitivity to noise and measurement error (Boone et al 1997). Also the reconstruction algorithm works best when including an accurate model of the system being imaged, that is, some *a-priori* information about the exact position of electrodes, the shape of electrodes and even the electrode-skin contact impedance. However, at present this iterative method can provide the most accurate and best spatial resolution of any reconstruction techniques.

#### **4.4 Image reconstruction using the sensitivity matrix**

The conductivity of a region, discretised into small areas or elements, can be written as a column matrix or vector. When the conductivity of a region within an object changes from a reference conductivity distribution  $c_{\text{ref}}$  (where each element has units of conductivity ( $\text{Sm}^{-1}$ )) to a conductivity  $c_{\text{dat}}$  (where each element has units of  $\text{Sm}^{-1}$ ) it represents a change in conductivity  $\Delta c = c_{\text{dat}} - c_{\text{ref}}$ , where  $\Delta c$  is a vector of the same size as both  $c_{\text{dat}}$  and  $c_{\text{ref}}$ . Images of this change in internal conductivity distribution can be

reconstructed from the resulting change in differential boundary voltages measured in volts ( $\Delta g = g_{\text{dat}} - g_{\text{ref}}$ ) from a uniform conductivity distribution, where  $g_{\text{dat}}$ ,  $g_{\text{ref}}$  and  $\Delta g$  are column vectors, usually of a different size from the conductivity vectors; the actual size depending on the number of independent differential boundary voltage measurements. These images of conductivity change can be obtained using a relationship described by a sensitivity matrix  $\mathbf{S}$  which is derived using a theorem by Geselowitz (1971). This relationship is given by:

$$\Delta g = S\Delta c \quad (4.2)$$

where  $\mathbf{S}$  is a sensitivity matrix (usually non-square),  $\Delta c$  is a vector containing the changes in conductivity and  $\Delta g$  is a vector containing the corresponding changes in voltage profiles. Matrix  $\mathbf{S}$  relates the small conductivity change within each individual pixel of the image to the corresponding differential boundary voltage change for each and every pixel and each and every drive-receive electrode combination. The relationship between  $\Delta g$  and  $\Delta c$  is often assumed to be linear (Barber and Brown 1990) and thus the elements of  $\mathbf{S}$  are independent of conductivity. The sensitivity matrix  $\mathbf{S}$  is usually calculated by assuming that the initial conductivity distribution is uniform, i.e. all elements within a region to be imaged have the same conductivity value (Barber and Brown 1990) and then calculating the resulting boundary voltage changes due to small perturbations in the conductivity values for each and every element.

The sensitivity matrix  $\mathbf{S}$  calculated and used here is a matrix of 208 by 1920 elements, the 208 rows being the 208 different voltage profiles (16 drive electrode pairs  $\times$  13 receive electrode pairs) and 1920 columns of sensitivity coefficient for each independent pixel corresponding to the 1920 pixels in the model being imaged as shown in Figure 4.2. The sensitivity coefficient for each pixel is given by:

$$S_{m,n,i} = -\int_u \frac{\nabla\Phi_m}{I_m} \frac{\nabla\Phi_n}{I_n} du \quad (4.4)$$

where  $i$  is the pixel number,  $m$  is the drive electrode pair,  $n$  is the receive electrode pair, the electrical field  $\Phi_m$  in pixel  $i$  is due to the current injected through electrode pair  $m$

and the electrical field  $\Phi_n$  in pixel  $i$  is that produced when electrode pair  $n$  is carrying the same current. The integration is over the volume of the element. In EIT where constant current is used,  $I_m = I_n = I$ , a constant which for this work will be taken as unity.

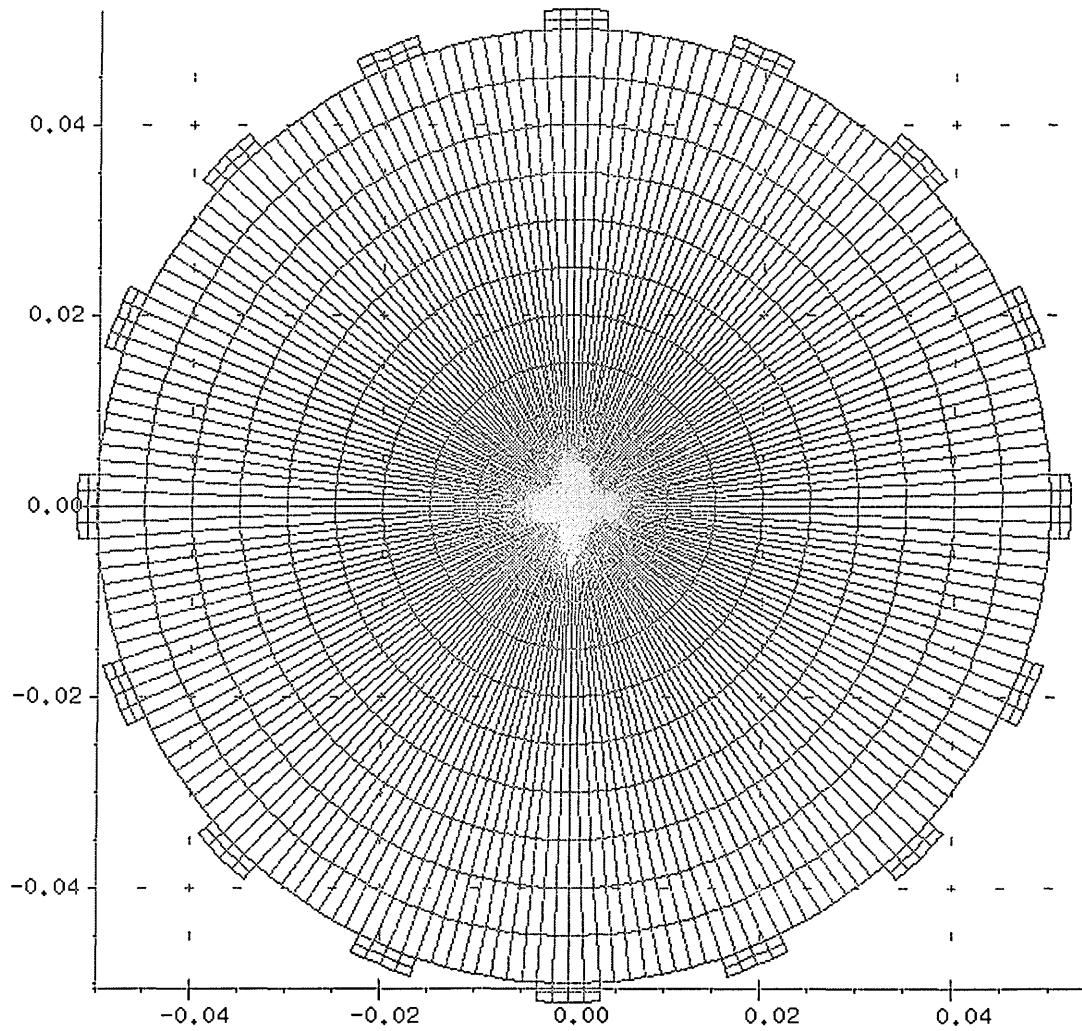


**Figure 4.2. Circular model used for calculation of sensitivity matrix and hence image reconstruction. The axis show the geometrical dimensions of the model with units of metres.**

The electric field can be calculated for each pixel using the finite element package available. Two scalar values ( $E_{x_i}$  and  $E_{y_i}$ ) are exported for each pixel for each drive combination, where  $i$  is the pixel number. These are the electric field components for pixel  $i$ .

The electric field ( $E_{x_i}$  and  $E_{y_i}$ ) was calculated at the Gaussian point of each second order element. It is therefore important to consider how accurate the calculated sensitivity matrix will be using these numerically derived electric fields. In theory the electric field for the model can be calculated at any point within an element or as an average of the total field over the whole element. In addition, elements can be of first, second or a higher order. The accuracy of the model, together with the calculated electric field and the derived sensitivity matrix will next be considered.

The sensitivity coefficient for pixel  $i$  is given by equation (4.5), where this coefficient is then integrated over the volume (area in the two dimensional case) to give the sensitivity coefficient for that pixel  $i$  for that given drive/receive pair. This was achieved using Matlab (The Mathworks Inc.), and the routines used, 'proj.m' and 'dot\_e.m', are given in Appendix C.

$$S_i = -\int_u (E_{x_m}, E_{y_m}) \cdot (E_{x_n}, E_{y_n}) du \quad (4.5)$$

The sensitivity matrix  $\mathbf{S}$  is therefore formed for a model consisting of 1920 discrete elements, Figure 4.2. To give a measure for the accuracy of this sensitivity matrix, it is possible to compare the voltage profile obtained from the FEM with the voltage profile calculated using equation (4.2). This is shown for a uniform model of unity uniform conductivity in Figure 4.3.

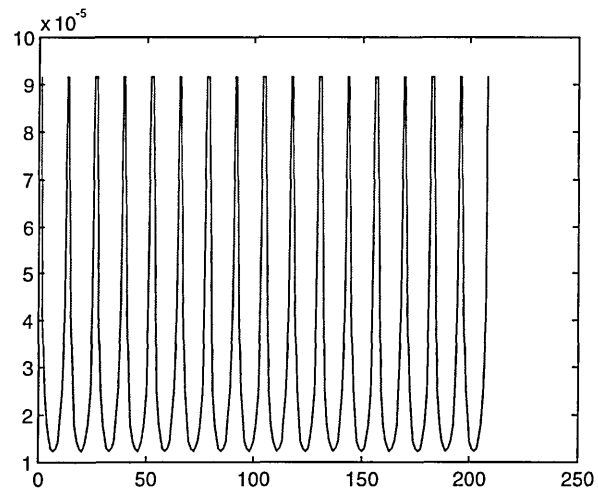


**Figure 4.3 (a) Voltage profile of a uniform model obtained using FEM**

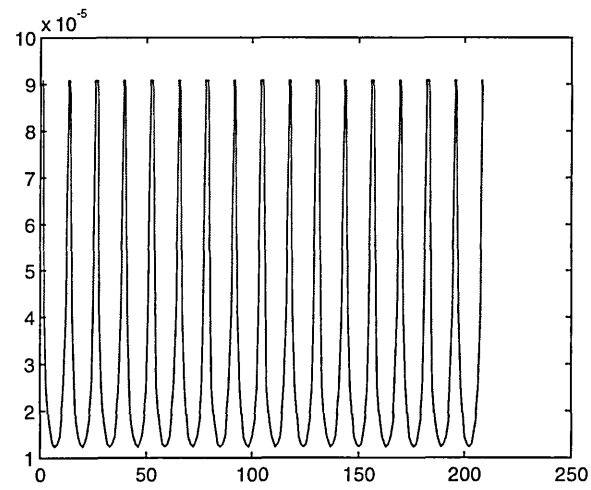


**Figure 4.3(b) Voltage profile of a uniform model obtained using the sensitivity matrix**

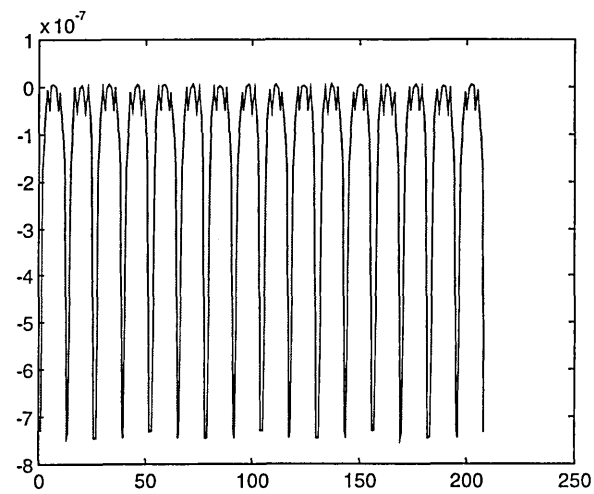


**Figure 4.3(c) Plot of the numerical difference of Figure 4.3 (a) and (b)**

There is a numerical difference between the two voltage profiles, Figure 4.3(c). However, the magnitude of this difference is very small compared to the actual value of voltages and is most likely due to numerical rounding errors.

A map of the sensitivity coefficient distributions for three various drive (m) and receive (n) pairs are shown in Figure 4.4. These visually correspond well with images produced by Kotre (1993).

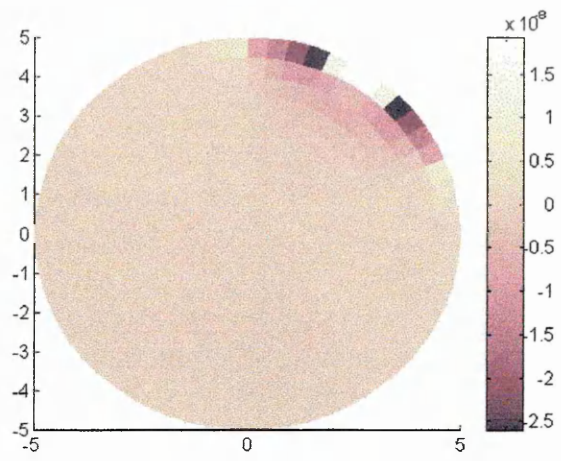


**Figure 4.4 (a) Sensitivity plot for  $m=1$  and  $n=1$**

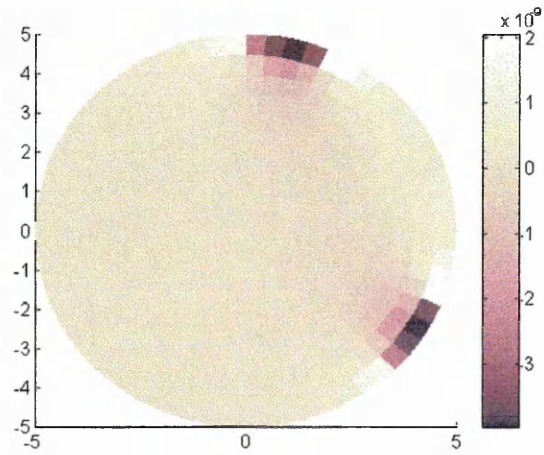


**Figure 4.4 (b) Sensitivity plot for  $m=1$  and  $n=4$**

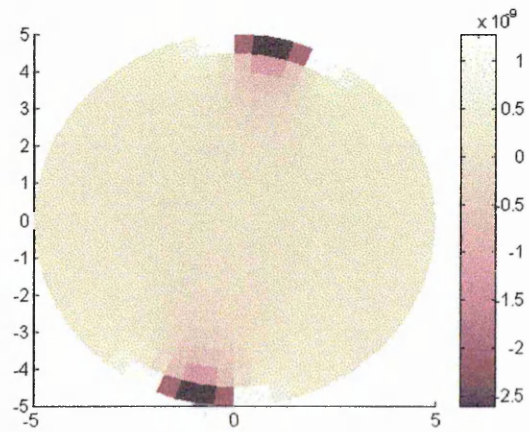


**Figure 4.4 (c) Sensitivity plot for  $m=1$  and  $n=7$**

In principle the calculated sensitivity matrix can now be used to reconstruct an image of the change in conductivity distribution from the boundary potential differences. This relationship can be derived from equation (4.2) to give:

$$\Delta c = S^{-1} \Delta g \quad (4.3)$$

where  $S^{-1}$  is the inverse of  $S$ .

The calculation of  $S^{-1}$  is not a straight forward problem.  $S$  is a non-square matrix. This implies that a square matrix must first be formed using  $S$ . This can be achieved using the following steps:

$$\Delta g = S \Delta c \quad (4.2)$$

$$S^T \Delta g = [S^T S] \Delta c \quad (4.6)$$

$$[S^T S]^{-1} S^T \Delta g = [S^T S]^{-1} [S^T S] \Delta c \quad (4.7)$$

$$\Delta c = [S^T S]^{-1} S^T \Delta g \quad (4.8)$$

where  $(.)^{-1}$  is the inverse operator and  $(.)^T$  is the transpose operator.

Matrix  $[S^T S]$  is singular. It is a square matrix ( $1920 \times 1920$ ) and has only a rank of 104. This singularity means that the problem has (virtually) a zero determinant and no true inverse exists to the problem. It is however possible to calculate a pseudo-inverse using various techniques, two of which are discussed here:

1. Pseudo-inverse using Singular Value Decomposition (Press et al 1992).

All the calculations described here are performed in Matlab, and the routines 'Invsvd.m' used are given in Appendix C. All images are reconstructed in Matlab and the routines 'plot\_c.m' are also given in Appendix C.

Singular Value Decomposition (SVD) breaks down a matrix  $M$  into three separate matrices such that

$$M = UKL^T \quad (4.9)$$

where  $U$  and  $L$  are orthogonal matrices of the eigenvectors and  $K$  is a diagonal matrix of singular values ( $k_1, k_2, k_3, \dots, k_i$ ) of  $M$ . The elements of  $K$  are arranged in order such that ( $k_1 > k_2 > k_3 > \dots > k_{i-1} > 0$ ).

The generalised matrix inverse defines the pseudo-inverse matrix  $M^{-1}$  to be the minimal least squares inverse of the matrix  $M$  such that

$$M^{-1} = UK^+L^T \quad (4.10)$$

where  $K^+$  is a diagonal matrix whose non-zero entries are given by:

$$K^+ = \begin{cases} \frac{1}{k_i} & \text{if } i > p \\ 0 & \text{if } i \leq p \end{cases} \quad (4.11)$$

where  $p$  is a the number of the singular values taken as the threshold level. The value of  $p$  can be chosen arbitrary. However,  $p$  is normally chosen based on a criteria defined to minimise error in the calculated conductivity from the true conductivity. In practical applications,  $p$  is usually determined by the signal to noise ratio of the measurement system. The smaller the threshold level, the more noise and error in the calculated pseudo inverse, but less blurring.

Zadehkoochack et al (1991) have presented images when the thresholding value  $p$  is varied. An example of this is shown in Figure 4.5.

Figure 4.5(a) shows the forward model of the distribution of conductivity used to generate boundary voltages using the FEM, together with the plot of each pixel conductivity values. Figure 4.5(b) - Figure 4.5(f) show the resultant reconstructed images for values of  $p = 10, 20, 30, 40$  and  $50$ , together with the plot of calculated pixel values. Absolute values are presented rather than differential by addition of known reference conductivity to the calculated change in conductivity.

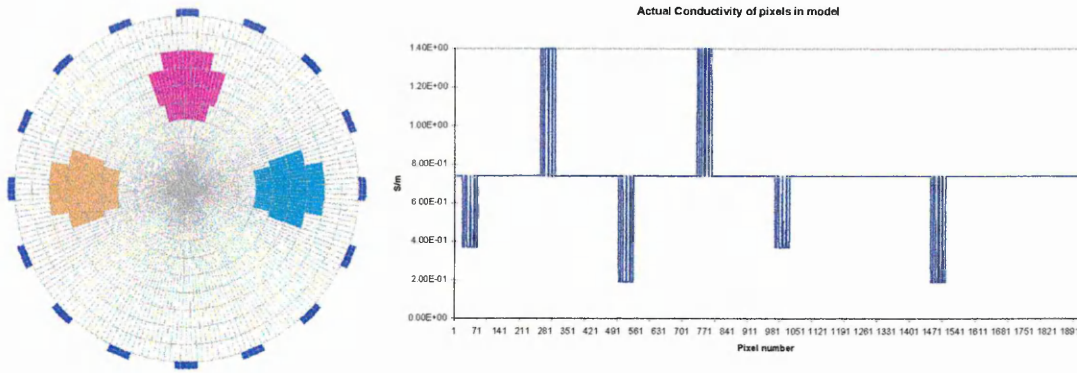


Figure 4.5(a). The forward model. Background conductivity is  $7.4 \text{ Sm}^{-1}$ , the top anomaly has a conductivity of  $1.4 \text{ Sm}^{-1}$ , left anomaly a conductivity of  $2 \text{ Sm}^{-1}$  and right anomaly a conductivity of  $3.7 \text{ Sm}^{-1}$ .

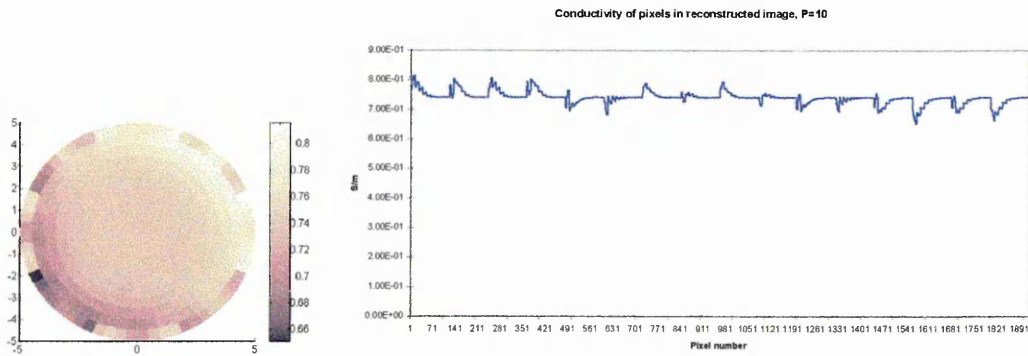


Figure 4.5(b) Reconstructed image when  $p=10$

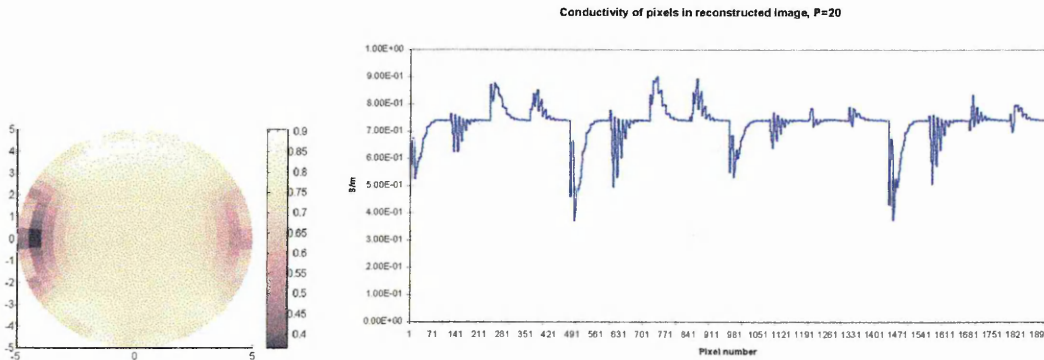


Figure 4.5(c) Reconstructed image when  $p=20$

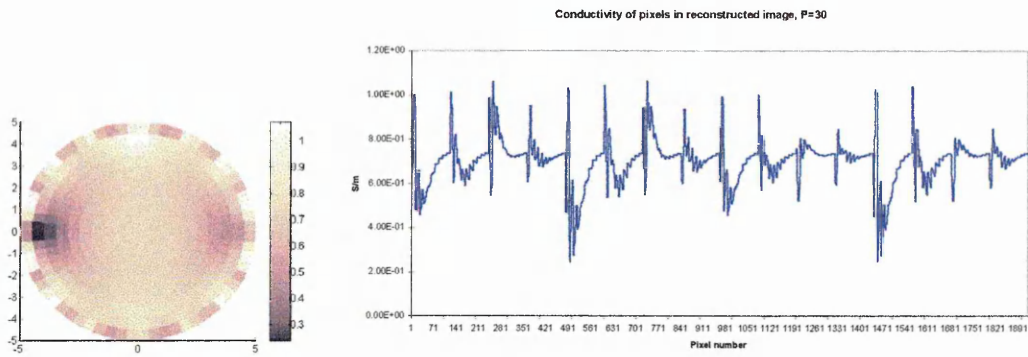


Figure 4.5(d) Reconstructed image when  $p=30$

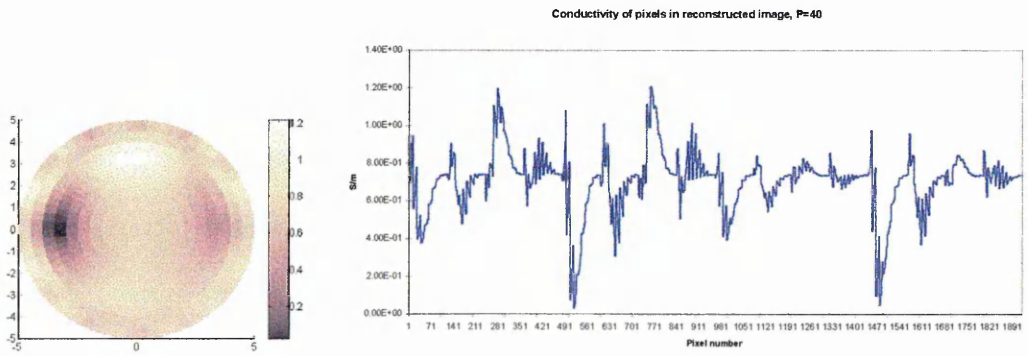


Figure 4.5(e) Reconstructed image when  $p=40$

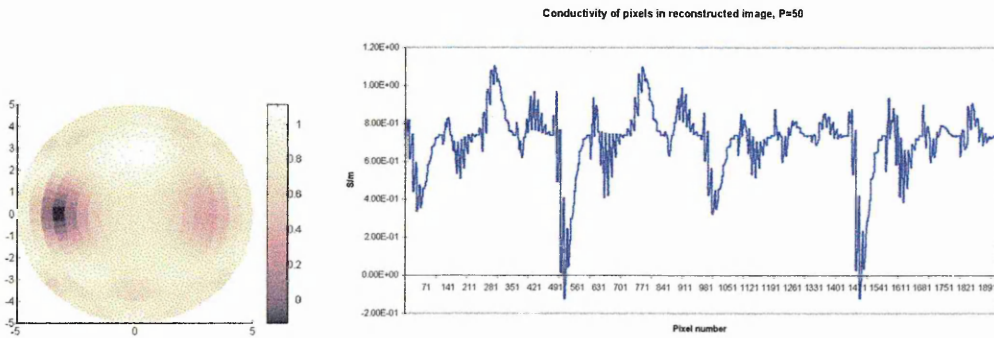


Figure 4.5(f) Reconstructed image when  $p=50$

## 2. Pseudo-inverse using diagonally dominant matrix (Menke 1989)

All the calculations described here are performed in Matlab, and the routines 'Invdamp.m' used are given in Appendix C.

The term  $[S^T S]$  is a square matrix of size 1920 by 1920, rank of 104 and has a very large (infinite) condition number. The condition number can however be calculated using MATLAB as approximately  $3 \times 10^{20}$ , which is considered as large. The condition number can be reduced by making the matrix diagonally dominant by

$$[S^T S + \lambda F_{\max} I]^{-1} \quad (4.12)$$

where  $\lambda$  is the regularisation factor,  $F_{\max}$  is the maximum main diagonal element value of matrix  $[S^T S]$  and  $I$  is a unity diagonal matrix of the same size as  $[S^T S]$ .

$[S^T S]$  is a square matrix but is regularised in order to reduce the condition number for the system and hence obtain a pseudo-inverse and hence an approximate solution. For a non-zero value of  $\lambda$  an inverse can be calculated although its condition number, and hence the stability of the inversion, will depend on  $\lambda$ . Generally speaking if  $\lambda$  is large the reconstructed image will be too smooth and blurred but if  $\lambda$  is too small the image will be dominated by noise.

The generalised matrix inverse defines the pseudo-inverse matrix  $[S^T S]^+$  to be the damped least square inverse of the matrix  $[S^T S]$  such that

$$[S^T S]^+ \approx [S^T S + \lambda F_{\max} I]^{-1} \quad (4.13)$$

Once the pseudo-inverse to  $[S^T S]$  has been calculated, it will be possible to calculate an approximation to the distribution of the change in conductivity from a set of boundary differential profiles using equation (4.7).

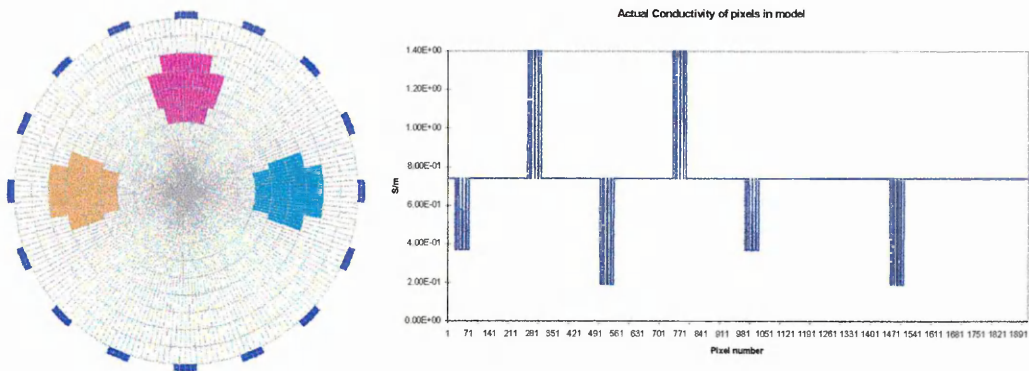


**Figure 4.6(a).** The forward model. Background conductivity is  $7.4 \text{ Sm}^{-1}$ , the top anomaly has a conductivity of  $1.4 \text{ Sm}^{-1}$ , left anomaly a conductivity of  $2 \text{ Sm}^{-1}$  and right anomaly a conductivity of  $3.7 \text{ Sm}^{-1}$ .

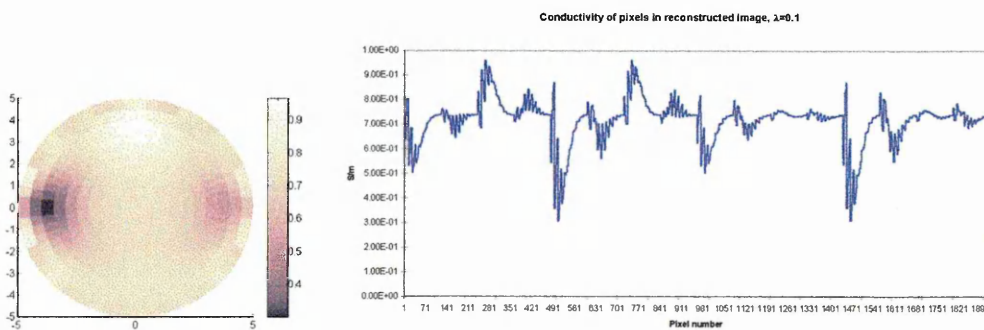


**Figure 4.6(b)** Reconstructed image when  $\lambda=0.1$

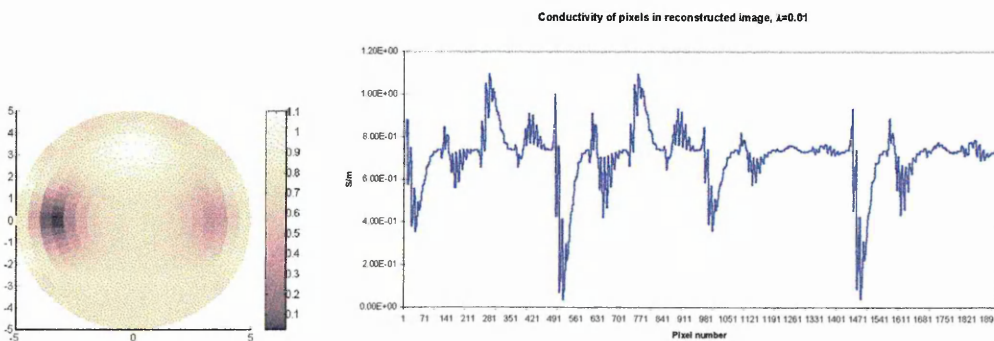


**Figure 4.6(c)** Reconstructed image when  $\lambda=0.01$

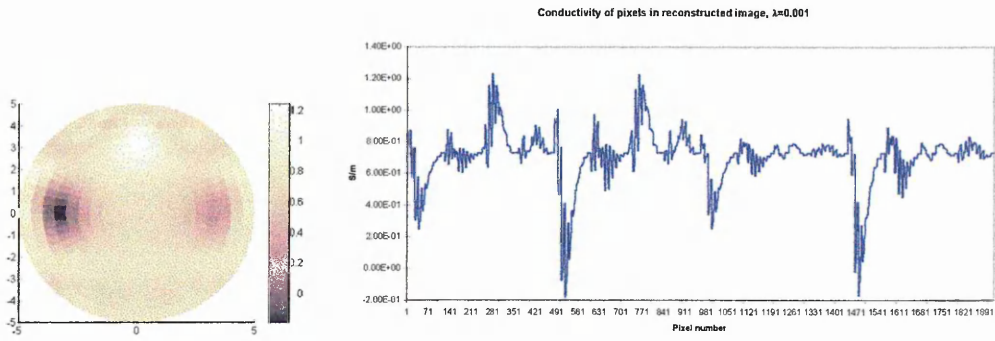


Figure 4.6(d) Reconstructed image when  $\lambda=0.001$

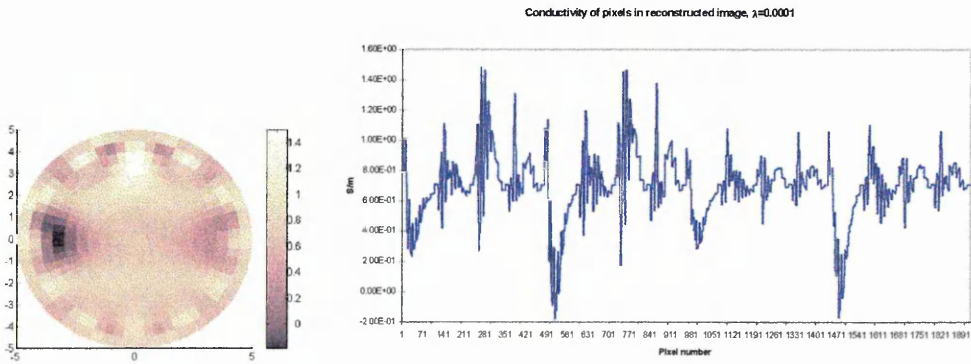


Figure 4.6(e) Reconstructed image when  $\lambda=0.0001$

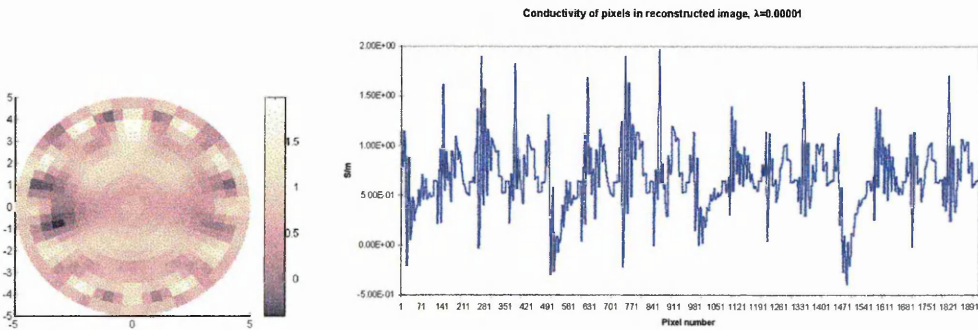


Figure 4.6(f) Reconstructed image when  $\lambda=0.00001$

Figure 4.6(b) - Figure 4.6(g) shows the effect of varying  $\lambda$  on the reconstructed images together with the actual distribution of the anomalies, Figure 4.6(a). In general terms, as  $\lambda$  decreases, more singular values of matrix  $[S^T S]$  are included in the calculation of the pseudo-inverse. It can be seen that this results in the image of the objects being pushed in towards the centre of the interrogated area and the image also contains more artefacts. For higher values of  $\lambda$  the image of the objects looks more spread out and blurred.

These images are static images and are produced by adding the known reference conductivity ( $c_{ref}$ ) to the calculated change in conductivity  $\Delta c$ .

#### **4.4.1 Discussions and conclusions**

Of the methods available for image reconstruction, differential imaging has been employed for this work. In differential imaging the images of changes in conductivity with reference to an initial conductivity are sought, which is also helpful since it assumes linearity for the problem. In this work, however, since the starting reference conductivity is known, from the forward model, images of the absolute conductivity distributions are presented. This is not possible in practice since the initial conductivity distribution is unknown for this mode of imaging.

The sensitivity algorithm has been used for image reconstruction. A finite element model is used to solve the forward problem to obtain a sensitivity matrix. To find a pseudo-inverse to the sensitivity matrix, two methods have been presented, using SVD and the damped least square method. Reconstructed images using both these methods have been presented and have been shown to produce an approximate solution to the internal conductivity distribution rather than an actual true distribution. The accuracy of the reconstructed image depends on the amount of regularisation used in both cases. No additional filtering of the final image has been carried out and the presented reconstructed images are 'raw' images.

Of the two pseudo-inversion methods described, the damped least square method is here considered as more accurate since the reconstructed images and values of conductivity are better calculated even at very high regularisation, as shown in figures

4.5 and 4.6. Further more this method proved to be a computationally faster method than the SVD.

## **4.5 The calculation of conductivity using the reduced sensitivity matrix.**

### **4.5.1 Introduction**

The calculation of the sensitivity matrix has so far been discussed, however, its accuracy in calculating the internal conductivity distribution needs to be investigated so that measures of error can be calculated.

In a given forward model, where the internal conductivity distribution is known, it is possible to use this information as *a-priori* information and reduce the size of the sensitivity matrix from 1920 columns to only a few columns with each column corresponding to a known region rather than a pixel. That is to say, instead of each pixel having a sensitivity coefficient, only each region will have a sensitivity coefficient. In this manner, the size of the sensitivity matrix is reduced and therefore its condition number reduces. This new reduced sensitivity matrix will no longer be singular, and a true inverse to the matrix will exist. Using this new reduced sensitivity matrix,  $S_{\text{reduced}}$ , conductivity values for separate regions in 18 different models of conductivity distributions will be calculated using the inverse solution. These calculated conductivity values will then be compared to the actual values to show errors of non-linearity.

Since all the work here is computational and the uniform reference conductivity is known, the absolute conductivity of regions will be calculated; that is, static imaging rather than differential imaging. These calculated absolute values for each region will be compared to the actual conductivity values for a given region in the forward model.

### **4.5.2 Method**

A circular model was used with a uniform conductivity distribution for the calculation of the sensitivity matrix. The simulation was at zero frequency and the conductivity of the uniform model was  $1 \text{ Sm}^{-1}$ .

The sensitivity matrix  $\mathbf{S}$  is non-square, near singular and badly conditioned, so the calculation of a true inverse is not possible. But for the following work the sensitivity matrix  $\mathbf{S}$  can be reduced in size.

The body to be imaged shown in Figure 4.7 contains 3 regions:

- i. background region
- ii. first anomaly region
- iii. second anomaly region.

It is therefore possible by knowing which pixels each region occupies in the forward model, to reduce the matrix  $\mathbf{S}$  from a 208 by 1920 elements to a 208 by 3 element matrix,  $\mathbf{S}_{\text{reduced}}$ . In this manner, instead of having a sensitivity coefficient for each individual pixel, each region has a sensitivity coefficient.

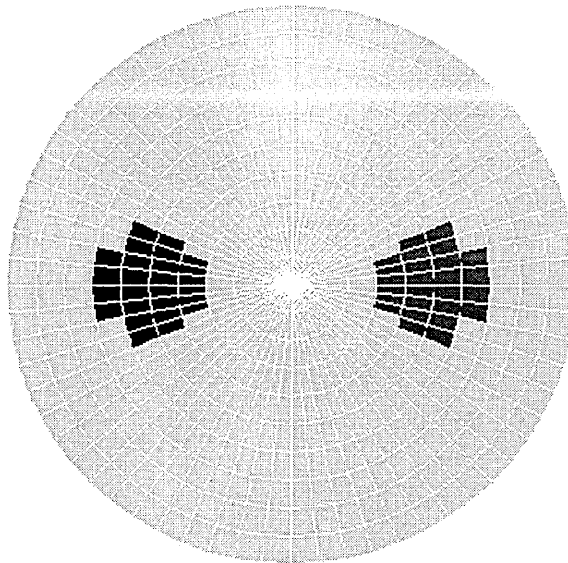


**Figure 4.7. Two off-centre anomalies in a uniform circular model.**

The reduction is achieved by simply summing the sensitivity coefficient of all pixels in each separate region to give one overall sensitivity coefficient for that region. Consider one voltage profile for all pixels in a given region:

$$g = cS_1 + cS_2 + cS_3 + \dots + cS_i \quad (4.14)$$

where  $g$  is the voltage profile,  $c$  is the conductivity value for the pixels which are from the same region and hence and have same conductivity values and  $S_i$  is the sensitivity coefficient for pixel  $i$ .

Equation (4.14) can be reduced to:

$$g = c(S_1 + S_2 + S_3 + \dots + S_i) \quad (4.15)$$

It can be therefore seen that the addition of the sensitivity coefficients of pixels occupying the same region to give one sensitivity coefficient is valid.

The new reduced sensitivity matrix  $S_{\text{reduced}}$  is still a non-square matrix but it is now much simpler to calculate an inverse to the matrix. This is achieved using the following relationship:

$$S_{\text{reduced}}^{-1} = [S_{\text{reduced}}^T S_{\text{reduced}}]^{-1} S_{\text{reduced}}^T \quad (4.16)$$

where  $(.)^T$  is the transpose of a matrix and  $(.)^{-1}$  is the inverse. The term  $[S_{\text{reduced}}^T S_{\text{reduced}}]$  is a small square matrix ( $3 \times 3$ ) and is now better conditioned (in the case described in this section the condition number for the matrix was 16.77). A true inverse to this matrix exists.

The changes in conductivity can now be calculated for each of the 3 regions by:

$$\Delta c = S_{\text{reduced}}^{-1} \Delta g \quad (4.17)$$

However this is only a calculated change in conductivity. Since the change in conductivity is given by:

$$\Delta c = c_{\text{dat}} - c_{\text{ref}} \quad (4.18)$$

where the uniform conductivity,  $c_{ref}$ , is known, it is possible to calculate the conductivity of the perturbed region from:

$$c_{dat} = \Delta c + c_{ref} \quad (4.19)$$

A total of 18 models were solved to obtain 18 voltage measurements. The conductivity of the uniform background was kept at a constant at  $1 \text{ Sm}^{-1}$  and the conductivity of the anomalies were varied from  $0.01$  to  $1 \text{ Sm}^{-1}$ .

To further show that this method for reduction of the sensitivity matrix is correct the following test provides a good validation. Both the full matrix  $\mathbf{S}$  and the reduced matrix  $\mathbf{S}_{reduced}$  were multiplied by a unity conductivity matrix with each in turn calculating the voltage profile for a unity conductivity distribution. Figure 4.8 shows the resultant calculated voltage profile. The graphs in Figure 4.8(a) and 4.8(b) are nearly identical. This shows that both methods give the same results and that use of the reduced sensitivity matrix is valid.

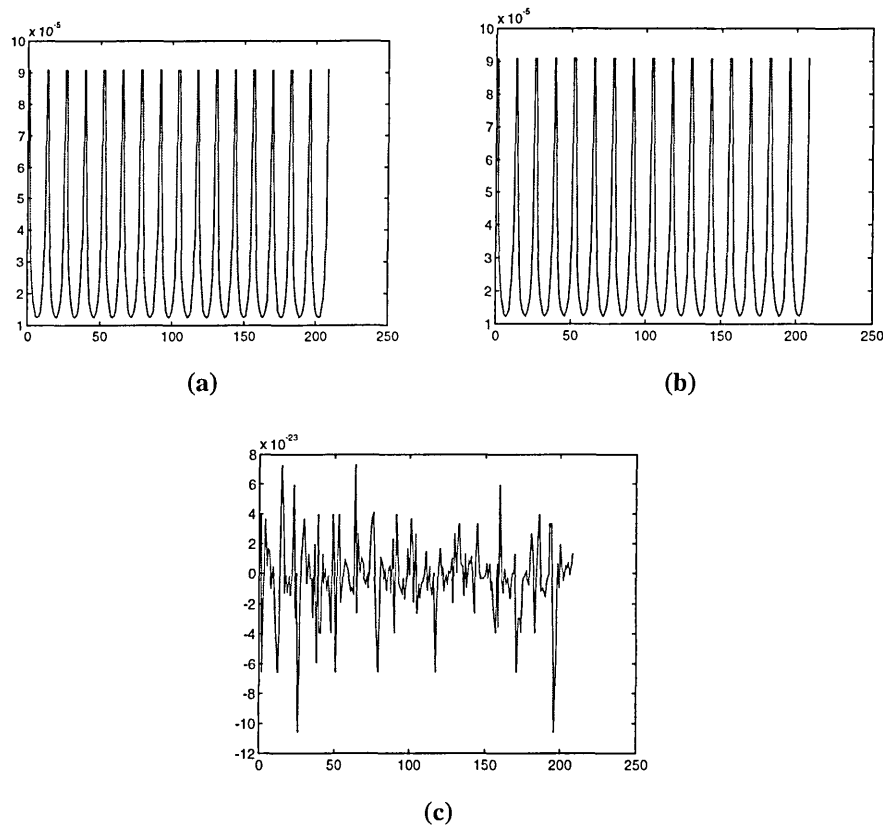


**Figure 4.8. Voltage profiles from a unity conductivity from (a) full (b) reduced matrix and (c) the difference between the full and reduced profiles**

The plot in Figure 4.8(c) shows the differences between the voltage profiles from the full and reduced matrix. The differences are in the order of  $10^{-23}$  which are very small and are definitely due to computational error.

The differential boundary voltages calculated for the 18 separate models were used to calculate the conductivity for the anomaly regions. Only one region is shown since both regions are of the same size and properties (both anomalies were perturbed by the same amount). The results are shown in Figure 4.9 and Table 4.1.

**Table 4.1. The actual and calculated values of conductivity using the reduced matrix**

Actual anomaly ( $\text{Sm}^{-1}$ )	Calculated Background ( $\text{Sm}^{-1}$ )	Calculated Anomaly ( $\text{Sm}^{-1}$ )
0.01	0.9996	-1.1618
0.02	0.9996	-1.1114
0.03	0.9996	-1.0626
0.04	0.9997	-1.0152
0.05	0.9997	-0.9691
0.06	0.9997	-0.9243
0.07	0.9997	-0.8807
0.08	0.9997	-0.8383
0.09	0.9998	-0.797
0.1	0.9989	-0.7661
0.2	0.9994	-0.408
0.3	0.9991	-0.1253
0.4	0.9996	0.1207
0.5	0.9996	0.3224
0.6	0.9997	0.4927
0.7	0.9993	0.6434
0.8	0.9993	0.7747
0.9	0.9996	0.8951
0.91	0.9995	0.9051
0.92	0.9995	0.916
0.93	0.9995	0.9269
0.94	0.9995	0.9376
0.95	0.9995	0.9482
0.96	0.9995	0.9587
0.97	0.9995	0.9691
0.98	0.9995	0.9794
0.99	0.9995	0.9895
1	1	1

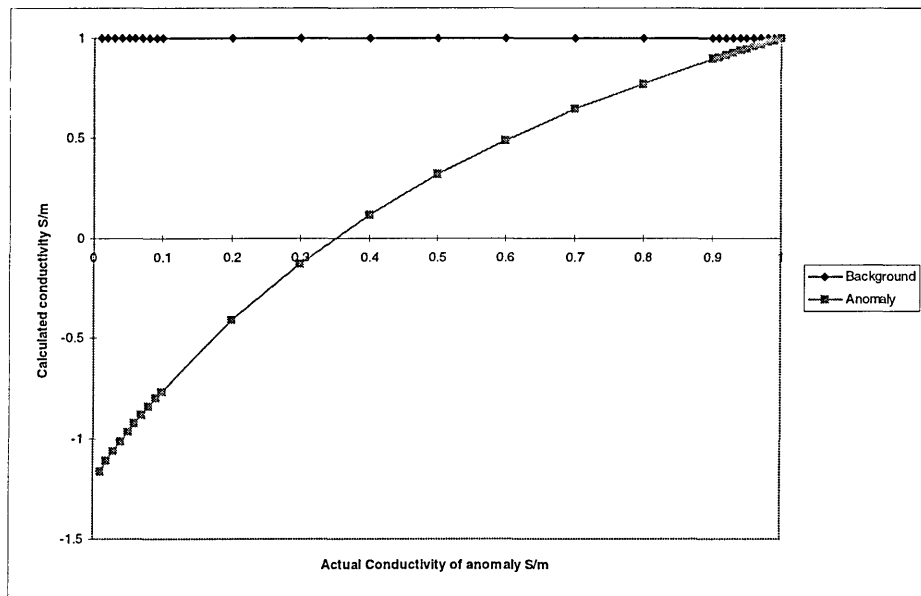


Figure 4.9. The plot of calculated anomaly and background conductivity against actual.

### 4.5.3 Results

The calculated background conductivity changes slightly with changes in anomaly conductivity. This shows that there is some interference (rather than blurring) from the conductivity of anomalies to the uniform background. No blurring effects are present here as the sensitivity matrix was accurately inverted without the use of a pseudo-inverse method.

The calculated anomaly conductivity is interesting. It shows high degrees of non-linearity. More clearly, it shows calculated negative conductivity for anomalies whose actual conductivity is greater than 65% of uniform reference conductivity (i.e. 1 S/m).

If the true conductivity of an anomaly is within 10% of the conductivity of the uniform background region, the conductivity calculated for that anomaly from calculated boundary voltages and using the reduced sensitivity matrix, is found to be accurate. For example, an anomaly whose true conductivity is  $0.96 \text{ Sm}^{-1}$ , the calculated conductivity is  $0.958 \text{ Sm}^{-1}$ , which is considered accurate. This 10% limit is therefore referred to as the linear region. Other studies have however reported that for a small region, the linear approximation is valid for the conductivity changes of up to 300% of the background (Shaw et al 1993).

#### **4.5.4 Discussion**

The sensitivity matrix that was originally calculated has been used to investigate the effect of non-linearity in image reconstruction using the sensitivity theorem. This has been achieved by reducing the large original sensitivity matrix, which represents individual elements, into a smaller matrix, now representing individual regions only. This reduction method produced a sensitivity matrix which was no longer ill-conditioned. This allows an accurate inversion of the sensitivity matrix thus eliminating any blurring effects due to regularisation.

The sensitivity matrix is an accurate method for calculating conductivity, providing that the change in conductivity of an anomaly is small compared to the uniform reference conductivity. It has been shown in this work that if the conductivity of an anomaly is within 10% of the reference uniform anomaly the calculated conductivity is reasonably close to the actual conductivity of the model.

It has also been shown that if internal anatomical information about a region to be modelled is known then the sensitivity matrix can be reduced to enable a faster image reconstruction which is also free of blurring effects due to matrix regularisation.

It has also been shown that there is interference between the conductivity of one region with another. The calculated conductivity of the background in this work was found to vary slightly with the actual conductivity of the anomalies. This interference can be due to the fact that the conductivity of anomalies disturb the path of current through the unperturbed uniform background.

The method described in this section will constrain the imaging method to 3 homogenous regions, so therefore details within each region can not be resolved.

## 4.6. Incorporation of a-priori information into image reconstruction

### 4.6.1. Introduction

The methodology of EIT and image reconstruction have so far been presented and discussed. It has been shown that due to ill conditioning of the problem and the near singularity of the sensitivity matrix, image reconstruction using the sensitivity matrix only provides an approximation to the conductivity distribution within the region to be imaged. In the following section, the concept of *a-priori* information to be incorporated into the image reconstruction method will be discussed to show the amount of possible improvement in the reconstructed images when *a-priori* information in the form of the spatial internal conductivity distribution is considered.

Previous investigations of such an approach includes the incorporation of *a-priori* information into the Sheffield filtered backprojection image reconstruction algorithm, which showed some success (Avis and Barber 1995). Also, Zadehkoochak et al (1991) presented a reconstruction algorithm based on the inversion of the sensitivity matrix associated with a non-uniform conductivity distribution using the singular value decomposition (SVD) method. They did not present any reconstructed images. Zadehkoochak et al (1993) have also investigated the use of *a-priori* information associated with imaging the thorax and reported artefacts in the resulting images. The use of a universal model (a standard model of internal conductivity distribution within the human thorax) has been speculated by Zadehkoochak et al (1993) to be invalid; however, it will be shown that providing the assumed anatomical model is closely matched to the patient's anatomy an improvement in the reconstructed image is achieved.

From equation (4.2):

$$\Delta g = S\Delta c \tag{4.2}$$

the relationship between  $\Delta g$  and  $\Delta c$  in the above equation is often assumed to be linear (Barber and Brown 1990) and thus the elements of  $\mathbf{S}$  are independent of conductivity.  $\mathbf{S}$  is usually calculated by assuming that the initial conductivity distribution is uniform, i.e. all elements within a region to be imaged have the same conductivity value (Barber

and Brown 1990) and then calculating the resulting boundary voltage changes due to small perturbations in the conductivity values for each and every element. The sensitivity matrix derived in this manner is, in this work, called the uniform sensitivity matrix, denoted by  $\mathbf{S}_{\text{unif}}$ . However, the relationship between the conductivity changes and the corresponding differential boundary voltages is not linear and virtually no interrogated region is uniform. The applied current distribution and therefore the voltage distribution within a body depends on the conductivity distribution within that body and as a consequence this is also true of the sensitivity matrix. For example, a small change in conductivity next to a physically large conductive area will have a smaller effect on the boundary voltages than the same small change in conductivity next to a relatively small area. Thus the coefficients of the true sensitivity matrix vary with the conductivity distribution and this matrix is referred to in this work as the ideal sensitivity matrix,  $\mathbf{S}_{\text{ideal}}$ .

In general therefore, although the sensitivity matrix  $\mathbf{S}$  changes with the conductivity distribution and equation (4.2) is therefore non-linear, it has been argued that for small changes in conductivity this non-linearity can be ignored (Barber and Brown 1990). Shaw et al (1993) have also reported a similar result, namely that for a small region, the linear approximation is valid for the conductivity changes of up to 300% of the background. This result does not however compare well with the findings of section 4.5. This is because the region of interest used by Shaw et al (1993) was comparatively very small with respect to the region used in the study described in section 4.5.

Previous work (section 4.5) has shown that the assumption of linearity by Barber and Brown (1990) is violated in conditions where there is a wide range of conductivity values; this is also in accordance with findings by Seagar (1983). Given accurate spatial and conductivity information about a region to be imaged, an accurate image of the conductivity distribution can be reconstructed from the boundary voltage data. Although this may be self-evident, it shows whether or not the relationship described by equation (4.2) is valid. It also shows the extent of the blurring of the image due to the algorithm and computational process. Also, it serves as a benchmark for images obtained using less *a-priori* information and as such is the "best" image that can be obtained. Recognising that in general complete anatomical information will not be available, this section will address the degree of accuracy needed in the *a-priori*

information in order to produce a useful reconstructed image. If the method is reasonably robust it may be possible to use anatomical information taken from a database rather than from the subject being imaged, contrary to previous speculations (Zadehkoochak et al 1993). It will be shown in the work presented here that providing the model is closely matched to that of the interrogated area an improvement in image quality is achieved. It also will be demonstrated how the present widely used sensitivity algorithm can be combined with an approximate knowledge of the spatial distribution of the tissues to provide a better estimate of the conductivity values.

#### **4.6.2. Method**

In order to generate the sensitivity matrix  $\mathbf{S}$ , the area of interest, a 2D circular tank, is split into 1920 triangular and brick elements as previously shown in Figure 4.2. The elements representing the modelled electrodes are not shown in the reconstructed images and the central elements are not displayed well due to their small size.

The linearised sensitivity matrix  $\mathbf{S}_{unif}$  is calculated (as discussed in section 4.4) assuming that the conductivity distribution is uniform before and after a change has occurred and this is the matrix which has been used to date even when the reference conductivity is not uniform (Barber and Brown 1990, Kotre 1989).

The sensitivity coefficient for each element  $i$  of  $\mathbf{S}_{unif}$  was calculated using equation (4.5), where for element  $i$  the electrical field  $(E_{x_m}, E_{y_m})$  in element  $i$  is due to the current injected through electrode pair  $m$  and the electrical field  $(E_{x_n}, E_{y_n})$  is that produced when the same current is injected through electrode pair  $n$ .

$$S_{unif(i)} = - \int_u (E_{x_m}, E_{y_m}) \cdot (E_{x_n}, E_{y_n}) du \quad (4.5)$$

The integration is over the area of the element  $u$ , i.e. multiplication of the dot product with the area of the element  $u$ .

In principle the calculated sensitivity matrix can now be used to reconstruct an image of the change in conductivity distribution calculated from the boundary potential differences. This relationship can be derived from equation (4.2) to give:

$$\Delta c = S^{-1} \Delta g \quad (4.3)$$

where  $S^{-1}$  is the inverse of  $S$ .

$S$  is a non-square (208 x 1920) and ill-conditioned matrix. Using the damped least squares method (Menke 1989):

$$\Delta c = [S^T S + \lambda F_{\max} I]^{-1} S^T \Delta g \quad (4.20)$$

Figure 4.10 shows an example of the effect of varying  $\lambda$  on the (resultant) reconstructed image. In this case the sensitivity matrix is that calculated for uniform conductivity distribution,  $S_{\text{unif}}$ . The model used to generate the boundary voltage data is also shown in Figure 4.10(a). The conductivity values used in the finite element model are shown in Table 4.2 (Weast, 1989). These conductivity values are different but not significantly different compared with the values used by other workers but note that the underlying principle described here will apply to any tissue conductivity value.  $S_{\text{unif}}$  was calculated by using a uniform conductivity distribution consisting of muscle tissue.  $\lambda$  is represented as fraction of the maximum diagonal value of matrix  $[S^T S]$ , where  $F_{\max} = 2.8653 \times 10^{-15}$ . In general terms, as  $\lambda$  decreases, more singular values of matrix  $[S^T S]$  are included in the calculation of the pseudo-inverse. It can be seen that this results in the image of the organs being pushed in towards the centre of the interrogated area and the image also contains more artefacts. For higher values of  $\lambda$  the image of the organs looks more spread out and blurred.

The images in Figure 4.10 and all subsequent images are static images and are produced by adding the known reference conductivity ( $c_{\text{ref}}$ ) to the calculated change in conductivity  $\Delta c$ .

**Table 4.2. The conductivity values of biological tissue (Weast 1989).**

	Muscle	Lung	Heart
Conductivity ( $\text{Sm}^{-1}$ )	0.74	0.11	1.16

We now replace the sensitivity matrix  $S_{\text{unif}}$  with the correct sensitivity matrix  $S_{\text{ideal}}$ . The calculation of the sensitivity coefficient for each element of  $S_{\text{ideal}}$  is done by using Geselowitz theorem and from equation (4.4) we have:

$$S_{ideal(i)} = -\int_u (Ex_m, Ey_m) \cdot (Hx_n, Hy_n) du \quad (4.21)$$

where for element  $i$  the electrical field components  $(Ex_m, Ey_m)$  in element  $i$  are due to the current injected through electrode pair  $m$  for the uniform conductivity and the electrical field components  $(Hx_n, Hy_n)$  produced when the same current had been injected through electrode pair  $n$  after there has been a change in conductivity from  $c_{ref}$  to  $c_{dat}$ , for pixel  $i$ , where  $c_{ref}$  is the uniform conductivity, i.e.  $0.74 \text{ Sm}^{-1}$ , and  $c_{dat}$  is the actual conductivity of pixel  $i$  for the thorax model used.

Figure 4.11(a) shows four 2D models of the human thorax. Each model was used for the calculation of its corresponding  $S_{ideal}$  and differential boundary voltages. Figure 4.11(b) shows the resulting reconstructed images using the calculated  $S_{ideal}$  for each corresponding model, with  $\lambda$  set at 0.01 for the calculation of each pseudo-inverse.  $F_{max}$  for a typical ideal sensitivity matrix is  $5.9324 \times 10^{-15}$ . The conductivity values used are again as shown in Table 4.2.

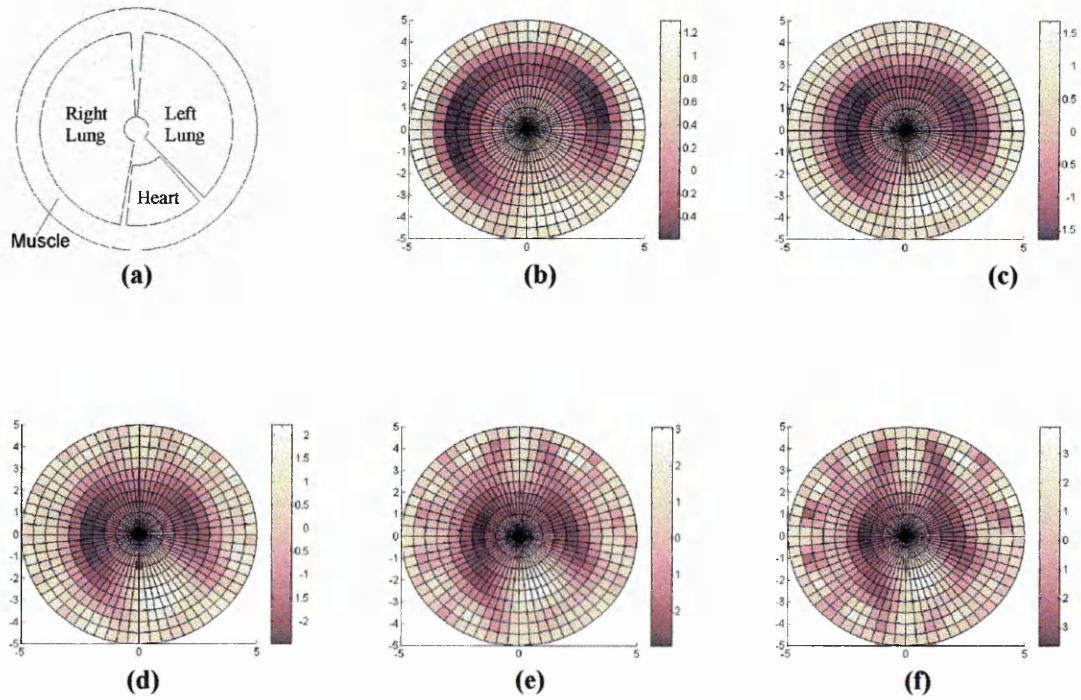


**Figure 4.10. (a) Model of the human thorax with the reconstructed images for various  $\lambda$ , where for diagrams (b - f),  $\lambda = 0.1, 0.01, 0.001, 0.0001$  and  $0.00001$  respectively. Reconstructed using  $S_{unif}$ .**

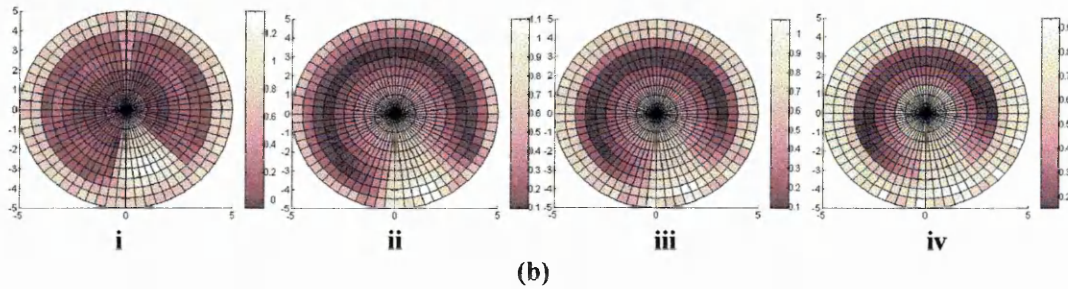
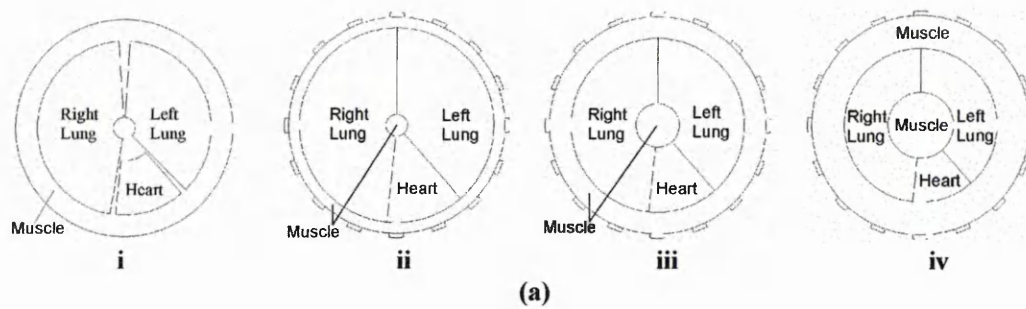


Figure 4.11. (a)i-iv The forward 2D problem models of human thorax and (b)i-iv the reconstructed images using their corresponding full Geselowitz sensitivity matrix, where  $\lambda = 0.01$

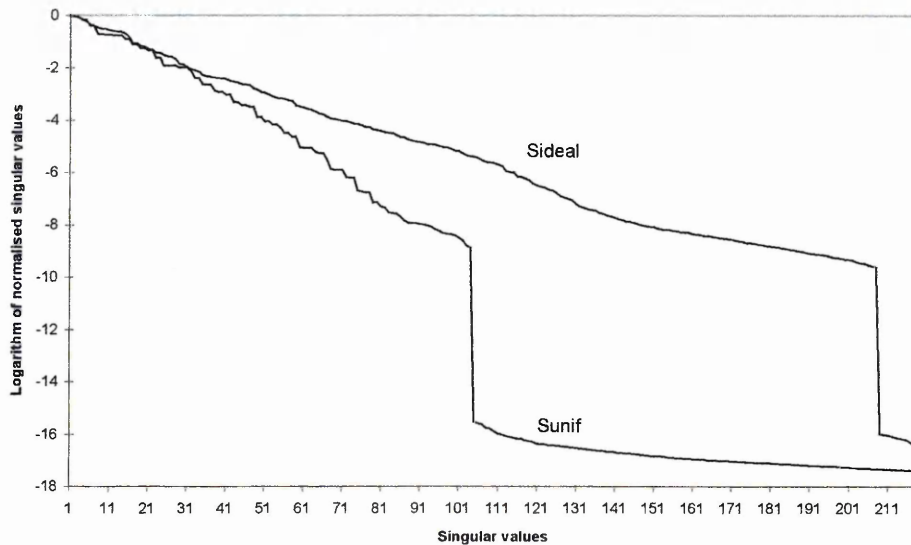


Figure 4.12. Plots of the first 220 singular values of the square matrices  $[S^T S]$  calculated using either  $S_{unif}$  (lower curve) or a typical  $S_{ideal}$  for a chest model (upper curve).

The sensitivity matrix  $\mathbf{S}_{\text{ideal}}$  for each model has a rank of 208 and is better conditioned than the corresponding square matrix formed from  $\mathbf{S}_{\text{unif}}$ , a result which has not been commented on before.

The rank of 208 for a sensitivity matrix calculated from two non-equal electric fields is not surprising as the reciprocity in this ideal sensitivity matrix will no longer be valid. But reciprocity in the differential boundary voltage data still holds and therefore the maximum possible rank of the data set will be 104 and therefore the overall underlying problem of reconstruction will have only a rank of 104.

Figure 4.12 shows a plot of the singular values of two square matrices  $[S^T S]$ , calculated using  $\mathbf{S}_{\text{unif}}$  and a typical  $\mathbf{S}_{\text{ideal}}$ . Initially, the differences between the singular values of the two different matrices are small. After the first 30 values, the singular values from the square matrix  $[S^T S]$  formed using  $\mathbf{S}_{\text{unif}}$  decay more rapidly than those of the square matrix  $[S^T S]$  formed using  $\mathbf{S}_{\text{ideal}}$ . This means that for a given level of regularisation more singular values are used in image reconstruction when using  $\mathbf{S}_{\text{ideal}}$  resulting in a better image resolution. The reconstructed image of the ideal human model obtained using  $\mathbf{S}_{\text{ideal}}$ , Figure 4.11(b)i, is more accurate than the corresponding image obtained using  $\mathbf{S}_{\text{unif}}$ , Figure 4.10, because  $\mathbf{S}_{\text{ideal}}$  incorporates the correct full anatomical and conductivity information. However, in clinical practice, the information used in the calculation of  $\mathbf{S}_{\text{ideal}}$  is not available.

In a clinical case where no information about the internal conductivity distribution is available it may be possible to estimate the conductivity distribution. For example, if an anatomical image from another high resolution modality, such as MRI, were available it should be possible to use this data, plus published values of tissue conductivity, to construct an initial  $\mathbf{S}_{\text{ideal}}$  which should certainly be an improvement on  $\mathbf{S}_{\text{unif}}$ . However, a more economical approach might be to use an MR image taken from a data base of images. In this case the image would not be a perfect match to the patients' anatomy but could be sufficiently close to provide a useful  $\mathbf{S}_{\text{ideal}}$ .

To test this approach, a total of six different *a-priori* models, Figure 4.13, were constructed, whose spatial conductivity distributions were varied from an over-

estimation to an under-estimation of the patient model of Figure 4.10(a), the ideal model. The conductivity values for the regions within the six models were calculated by superimposing each model onto the ideal patient model and averaging the conductivity values of each element within the area covered by each non-ideal patient region. The total conductivity of each model is hence kept constant and equal both to each other and to the ideal model. This method of calculating the conductivity values was chosen rather than using a typical set of published values, to allow for a wider range of possible conductivity values. In this manner, the model is not restricted to a fixed geometry, but also the regional conductivity values are allowed to vary within a considerable range. The conductivity values used for each model are shown in Table 4.3.

**Table 4.3. The conductivity values used for the non-ideal patient models shown in Figure 4.13.**

	Muscle ( $\text{Sm}^{-1}$ )	Lung ( $\text{Sm}^{-1}$ )	Heart ( $\text{Sm}^{-1}$ )
Model (a)	-	0.07	0.64
Model (b)	1.5	0.08	0.8
Model (c)	0.75	0.11	1.06
Model (d)	0.5	0.17	1.6
Model (e)	0.38	0.33	3.19
Model (f)	0.3	-	-

These new models shown in Figure 4.13 were used as the *a-priori* information and a new ideal sensitivity matrix was calculated for each of the six different *a-priori* models using the same method as described for the previous example. Two regularisation factors,  $\lambda$  of 0.1 and 0.01, were chosen for the reconstruction for each case. These values have been selected *a-posteriori* by visual examination. The regularisation parameter could also be chosen by some objective method but according to Kolehmainen et al (1997) these do not always give (visually) meaningful results. In practice, where there is noise in the data, a high value of  $\lambda$  such as 0.1 must be used to minimise the reconstruction error by damping out the noise with a consequent loss in spatial resolution. This is visually evident from the reconstructed images shown in Figure 4.10.

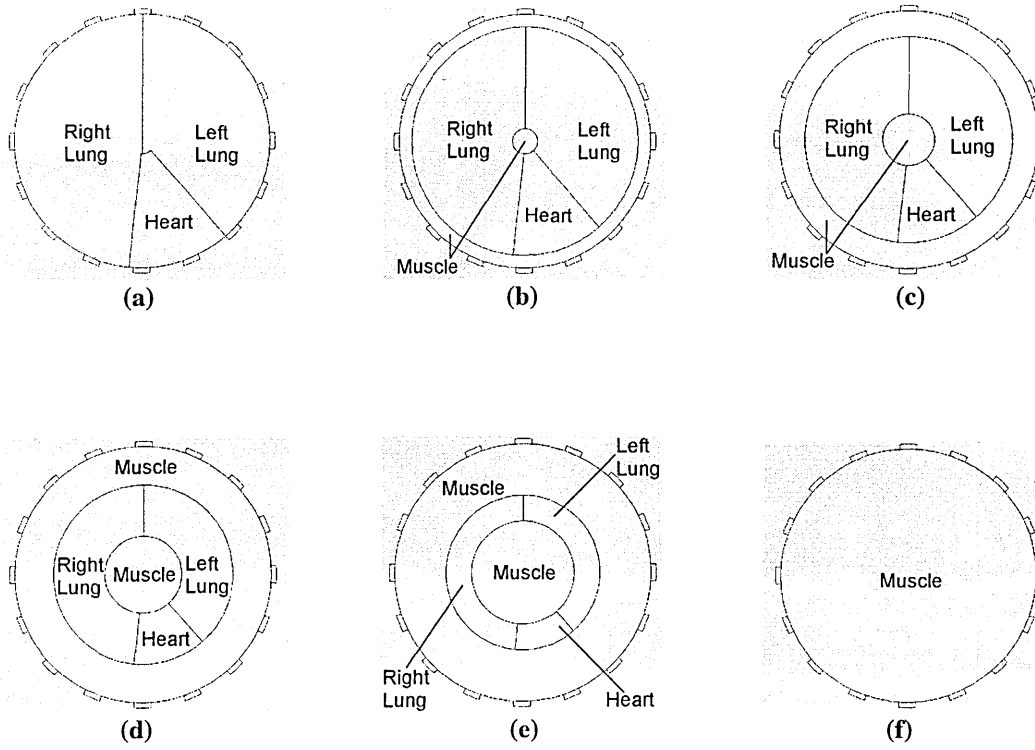


**Figure 4.13. A set of pre-defined regions of interest, which over-estimates the size and position or under-estimates the size and positions of organs. (a) is the most over-estimated with no muscle tissue region, and (f) is the most under-estimated with only muscle tissue region.**

The boundary voltage data taken from the ideal patient model was used to reconstruct a set of images using each of these six new ideal sensitivity matrices for each of the two values of  $\lambda$ ; Figure 4.14(b) ( $\lambda = 0.1$ ) and Figure 4.14(c) ( $\lambda = 0.01$ ). As a measure of the accuracy of the new reconstructed images, the  $\Delta_{rms}$ , on a pixel by pixel basis, was calculated with respect to the ideal reconstructed image of the same value of  $\lambda$ , as shown in Figure 4.14(a)(ii-iii). The  $\Delta_{rms}$  values for the six images in Figure 4.14 are shown in Table 4.4. The  $\Delta_{rms}$  is given by:

$$\Delta_{rms} = \sqrt{\frac{1}{1920} \sum_{i=1}^{1920} (c(i)_{calculated} - c(i)_{ideal})^2 \times u_i} \quad (4.22)$$

where  $c(i)_{calculated}$  is the calculated conductivity for pixel (i),  $c(i)_{ideal}$  is the 'ideal' or best reconstructed conductivity for the same pixel (i) and  $u_i$  is the area of the pixel (i).

**Table 4.4. The  $\Delta_{rms}$  of the new reconstructed images shown in Figure 4.14(b and c) with respect to the ideal reconstructed image, Figure 4.14(a)i-ii.**

	$\Delta_{rms} (\lambda=0.1)$	$\Delta_{rms} (\lambda=0.01)$
Model (a)	$1.36 \times 10^{-6}$	$2.06 \times 10^{-6}$
Model (b)	$9.97 \times 10^{-7}$	$1.56 \times 10^{-6}$
Model (c)	$6.40 \times 10^{-7}$	$9.03 \times 10^{-7}$
Model (d)	$1.15 \times 10^{-6}$	$1.70 \times 10^{-6}$
Model (e)	$1.42 \times 10^{-6}$	$2.52 \times 10^{-6}$
Model (f)	$1.30 \times 10^{-6}$	$3.34 \times 10^{-6}$

The smallest value of the  $\Delta_{rms}$  is seen when the model in Figure 4.13(c) is used for the *a-priori* information. The  $\Delta_{rms}$  increases as the differences between the *a-priori* model and the ideal patient model increases; it is worth noting that the value of  $\lambda=0.1$  reconstructs the more accurate image.

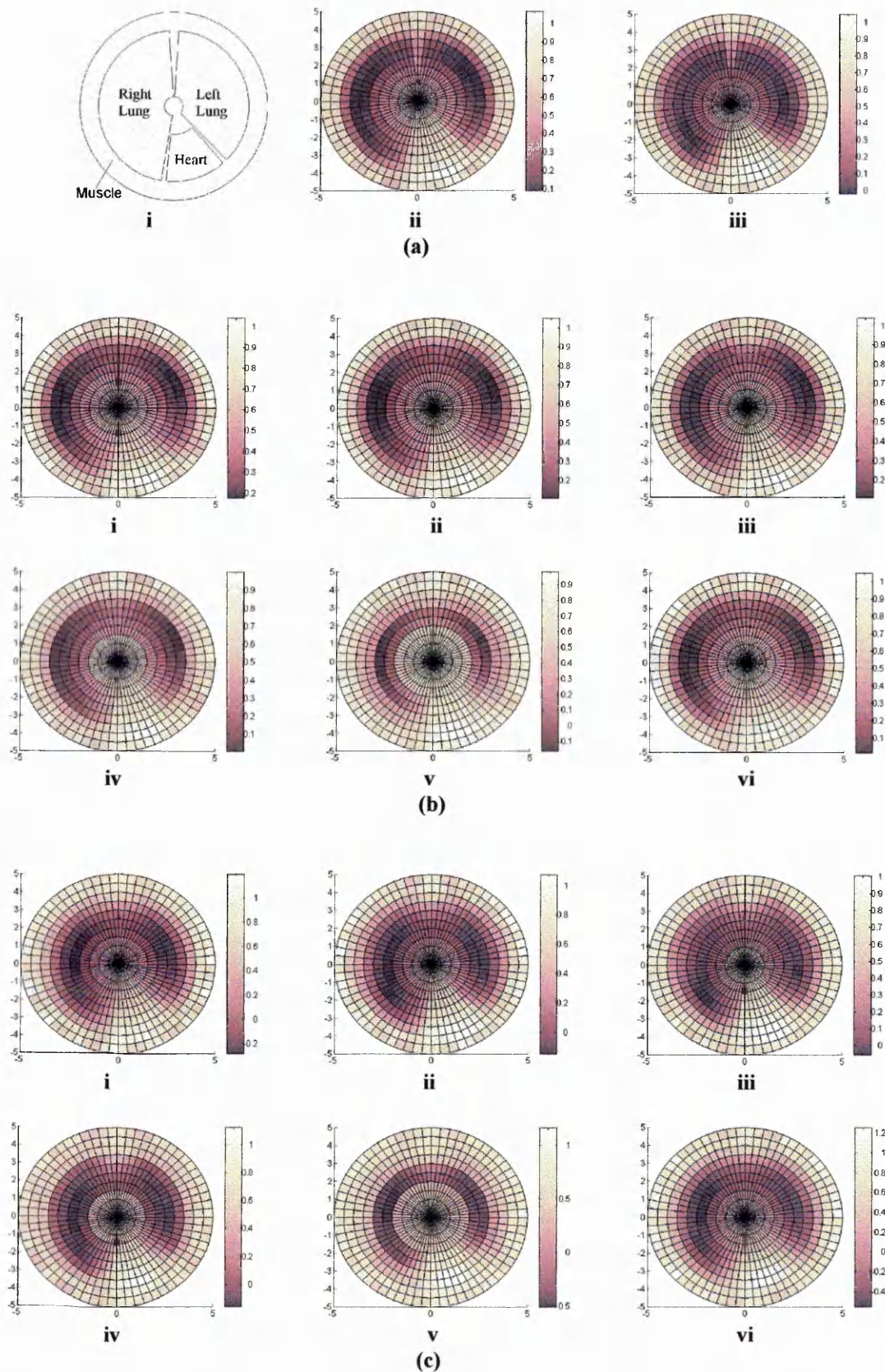


**Figure 4.14. (a)i** The ideal patient model. **(a)ii** ideal image reconstructed with  $\lambda=0.1$  and **(a)iii** the ideal image reconstructed with  $\lambda=0.01$ . Images **(b)** and **(c)**: The reconstructed images using the sensitivity matrices calculated from the anatomical models shown in figure 4.13. Images **(b)** and **(c)** i - vi correspond to the models shown in figure 4.13 (a) to (f).  $\lambda=0.1$  for images **(b)** i - vi and  $\lambda=0.01$  for images **(c)** i - vi.

### **4.6.3 An iterative algorithm based on the sensitivity matrix**

The models described so far all contain some estimates of the conductivity values of the tissues. In practice these may not be known with any accuracy; indeed, the determination of the conductivity values is an important aim of EIT imaging. It has been shown that using a close approximation of the internal conductivity distribution improves the quality of the reconstructed images. It will now be shown how the anatomical information can be used, without making any prior assumptions about tissue conductivity values, in order to determine these conductivities.

Initially, all the conductivity values are assumed the same. The boundary voltage data from the ideal patient model is used together with the uniform sensitivity matrix  $\mathbf{S}_{\text{unif}}$  to reconstruct an initial image of the internal conductivity distribution for the ideal patient. The ideal structural information as shown in Figure 4.15(a)i was super-imposed over the reconstructed image Figure 4.15(b)i for ( $\lambda = 0.1$ ) and Figure 4.15(c)i for ( $\lambda = 0.01$ ), and the reconstructed conductivity values of the initial image in each segment of the superimposed image were averaged. These conductivity values were used to calculate a new electric field distribution and hence a new sensitivity matrix which was then used to produce another new reconstructed image. This step was repeated until no further improvement to the reconstructed images was found; in this case after 9 iterations. Two regularisation factors  $\lambda=0.1$ , Figure 4.15(b), and  $\lambda=0.01$ , Figure 4.15(c), were used. To measure the accuracy, the ideal image was reconstructed for each value of  $\lambda$ , Figure 4.15(a)ii and 4.15(a)iii, and the  $\Delta r_{\text{rms}}$  was calculated for each image with respect to its ideal image reconstructed with the same value of  $\lambda$ . The reconstructed images at iteration step 9 of both values of  $\lambda$  are shown in Figure 4.15(b)ii and Figure 4.15(c)ii.

If the sensitivity matrix is not correct it is possible, due to high non-linearity of the problem, for negative conductivity values to be calculated from boundary voltage data - a physical impossibility. Where this occurred the conductivity was set to the small value of  $0.01 \text{ Sm}^{-1}$  (a small non-zero value). The conductivity values for each region calculated at iteration steps 1 and 9 are shown in Table 4.5.

**Table 4.5. The conductivity values for each region of images found in Figure 4.15(b) and 4.15(c)**

	Muscle ( $\text{Sm}^{-1}$ )	Right lung ( $\text{Sm}^{-1}$ )	Left lung ( $\text{Sm}^{-1}$ )	Heart ( $\text{Sm}^{-1}$ )
$\lambda=0.1$ : Iteration step 1	0.67	-0.04	-0.01	0.62
$\lambda=0.1$ : Iteration step 9	0.69	0.26	0.27	0.69
$\lambda=0.01$ : Iteration step 1	0.55	-0.78	-0.71	0.73
$\lambda=0.01$ : Iteration step 9	0.71	0.48	0.47	0.79

Figure 4.16 shows the plot of the  $\Delta$ rms calculated for each of the two regularisation factors at each step of the iteration process.

It can be seen that after the 1st iteration the  $\Delta$ rms is reduced and in spite of the oscillatory behaviour some further improvement in the image quality measure seems possible although the image does not converge exactly to the ideal image. It can be seen that due to non-linearity the calculated conductivity values, shown in Table 4.5, the values at iteration step 1 are inaccurate, and in some cases negative; by iteration step 9, although the calculated conductivity values do not accurately match the actual values, they are no longer negative and are closer to their true value.

The aim of the next set of experiments was to investigate how close the estimated anatomical structure must be to the actual patient anatomy for a successful iteration, i.e. an improved reconstructed image. In this part of the study boundary data was calculated from three patient models using the models shown in Figure 4.17(a)i-iii. These data sets were used together with a pre-defined set of internal conductivity distribution, Figure 4.17(b), in the iterative method already described. In this case we simulate the situation where the *a-priori* model for the anatomy was the same for all patients. The reconstructed images using the uniform sensitivity matrix are shown in Figure 4.17(c)i, Figure 4.17(d)i and Figure 4.17(e)i for each the patient models shown in Figure 4.17(a)i-iii respectively. The reconstructed images at iteration step 9 is shown in Figure 4.17(c-e)ii. The regularisation factor of  $\lambda=0.1$  was used for all cases. The conductivity values for each region calculated at iteration steps 1 and 9 are shown in Table 4.6.

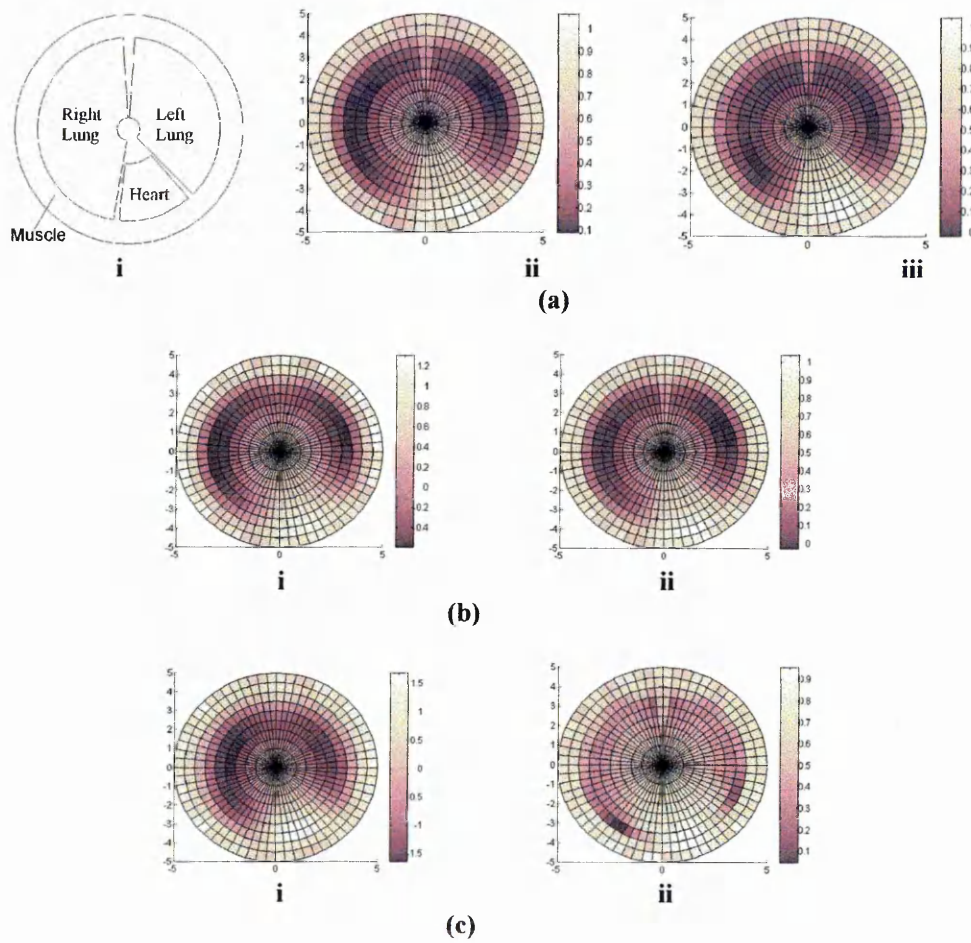


Figure 4.15. (a) The ideal patient model. (a)ii Ideal image reconstructed with  $\lambda=0.1$  and (a)iii the ideal image reconstructed with  $\lambda=0.01$ . (b) and (c) Images reconstructed using  $\lambda=0.1$  and  $\lambda=0.01$  respectively, (b)i and (c)i using uniform sensitivity matrix. (b)ii and (c)ii at iteration step 9.

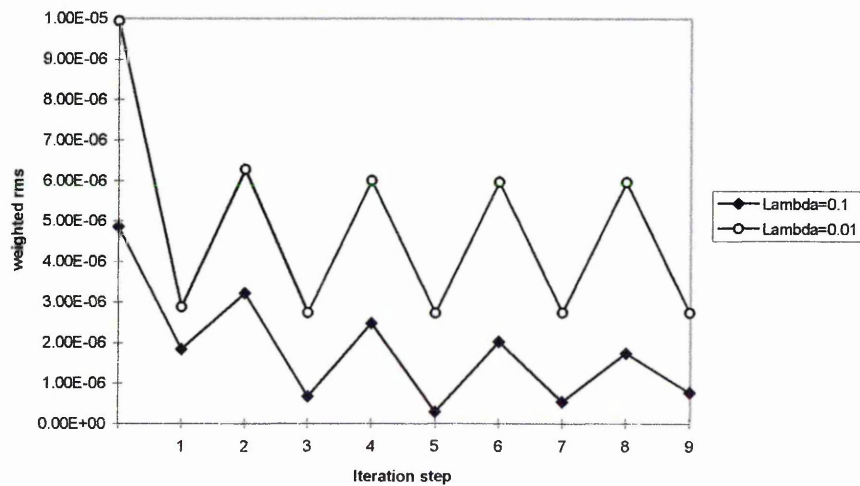


Figure 4.16. Graph showing the  $\Delta rms$  with respect to ideal reconstructed image of same  $\lambda$ , calculated at each iteration step.

**Table 4.6. The conductivity values for each region of images found in Figure 4.17(c) - 4.17(e)**

	Muscle ( $\text{Sm}^{-1}$ )	Right lung ( $\text{Sm}^{-1}$ )	Left lung ( $\text{Sm}^{-1}$ )	Heart ( $\text{Sm}^{-1}$ )
Image 4.17(c): Iteration step 1	0.35	-0.51	-0.48	0.70
Image 4.17(c): Iteration step 9	0.58	0.50	0.49	0.77
Image 4.17(d): Iteration step 1	0.66	-0.05	-0.03	0.60
Image 4.17(d): Iteration step 9	0.68	0.27	0.27	0.68
Image 4.17(e): Iteration step 1	0.75	0.26	0.27	0.61
Image 4.17(e): Iteration step 9	0.75	0.34	0.35	0.65

Figure 4.18 shows the plot of the  $\Delta r_{ms}$  calculated for each of the images in Figure 4.17(c-e) with respect to their ideal image reconstructed at the same value of  $\lambda=0.1$ .

It can be seen that once again after the 1st iteration the  $\Delta r_{ms}$  is reduced and again although the behaviour is oscillatory some further improvement seems possible. The best improvement is seen in the images reconstructed when the patient data comes from a model which closely approximates the *a-priori* model used for the iteration. It can be seen from the calculated conductivity values that due to the non-linear nature of the problem, negative conductivity were calculated at iteration step 1. By step 9, however, using the technique for handling negative calculated conductivity values previously described, the final conductivity values were generally closer to the actual conductivity. The image in Figure 4.17(d)ii is the closest to its ideal reconstructed image, demonstrating that the use of *a-priori* anatomical information close to the true anatomical information produces better calculated conductivity values.

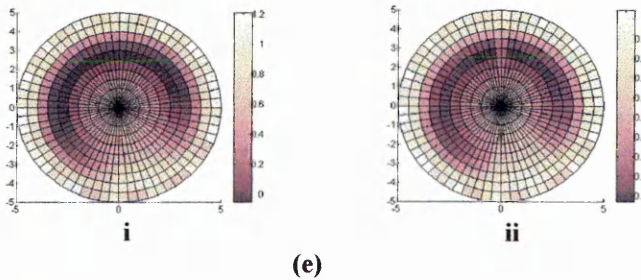
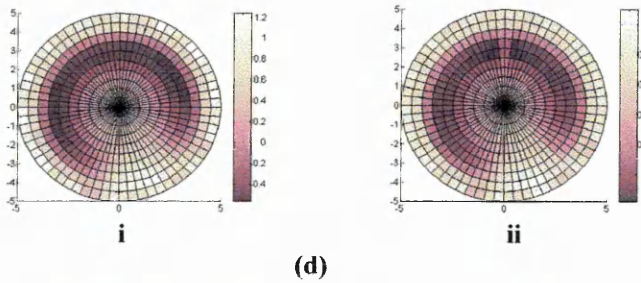
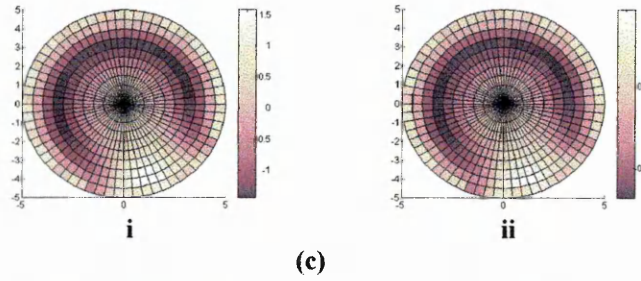
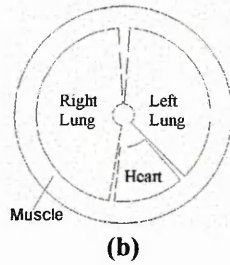
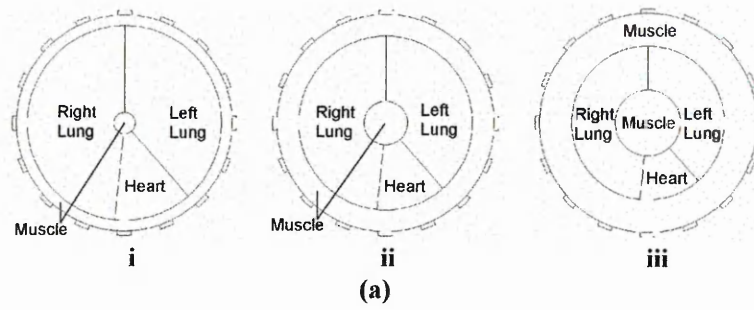
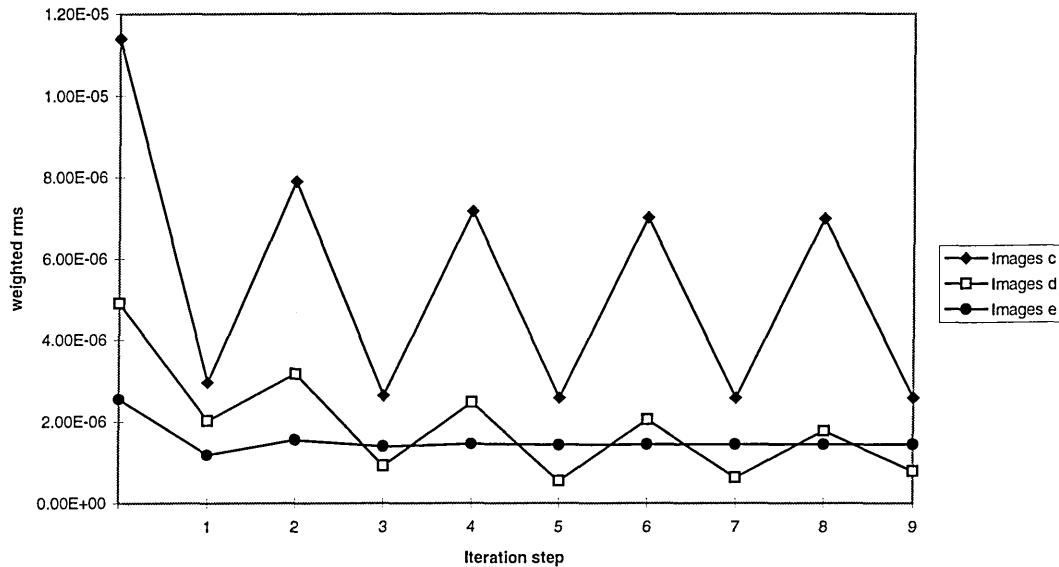


Figure 4.17. (a) The three patient models used for boundary data calculations. (b) The estimate of internal conductivity distribution used for internal conductivity calculations. (c) The reconstructed images using (i) uniform sensitivity matrix and (ii) at iteration step 9, from patient data (a)i. (d) The reconstructed images using (i) uniform sensitivity matrix and (ii) at iteration step 9, from patient data (a)ii. (e) The reconstructed images using (i) uniform sensitivity matrix and (ii) at iteration step 9, from patient data (a)iii.



**Figure 4.18.** Graph showing the  $\Delta_{rms}$  of images in figure 4.17(c-e) with respect to ideal reconstructed image of same  $\lambda$ , calculated at each iteration step.

#### 4.6.4. Discussion

Three cases have been presented where the inclusion of anatomical *a-priori* information into the reconstruction algorithm has been tested. In the first case, a complete set of *a-priori* information was used. This included not only the internal conductivity distribution (geometrical positions of organs) but also the true conductivity values of each region. The resulting reconstructed image showed a great improvement in comparison with an image reconstructed where no *a-priori* information had been included. This shows, as expected, that given all the *a-priori* information a much more accurate image can be reconstructed from the boundary data. Of course, if such information were available no imaging would be required but this work does show the best reconstructable image possible. In the second case, an *a-priori* approximation was made as to the internal anatomy (six approximate cases, from over-estimation to under-estimation), together with an estimate of the conductivity values for the interrogated area. The results show an improvement in the (resulting) reconstructed image compared to the images obtained using only the standard sensitivity matrix  $S_{unif}$ . The best improvement is seen when the approximation to the internal structure is a close match to the actual anatomy.

This work has shown that a high value of regularisation factor works well compared to smaller values where computational noise is present. Also, it has been shown that it is possible to iterate from the initial reconstructed image to a more accurate image using a sensitivity matrix which has been calculated initially from a uniform conductivity distribution together with the anatomy of the region to be imaged. Using this method, improvements are seen after the first iteration. No visible improvements were found after the ninth iteration. Finally, the boundary data from three patient models have been used to reconstruct images using a sensitivity matrix which was initially calculated from a uniform conductivity distribution. Using a model of the estimated anatomy, it has been found that there is an improvement in the reconstructed images using the iterative method proposed here. The best improvement were seen when the *a-priori* anatomy closely matched the patient's anatomy. Traces of the anatomical model used to estimate the *a-priori* information can be clearly seen in all the final images reconstructed using this iterative method. These images may not be anatomically more accurate but the calculated conductivity values are more accurate than those where the reconstructed images are obtained as a single pass from the uniform sensitivity matrix.

Future work on this imaging reconstruction method could include the ability to adjust the shape of the anatomical information, within appropriate constraints, to more closely represent the anatomy of the patient. This could be done by defining an appropriate warping function whose parameters are treated as unknowns in the reconstruction process. Chest expansion has been shown to create an additional artefact in EIT measurements of the thorax (Alder et al 1994). Further considerations may be needed to include more accurate *a-priori* information where any chest expansion maybe considered.

#### **4.6.5. Conclusion**

A considerable improvement in the reconstructed image can be obtained by using accurate *a-priori* information about a region to be imaged. It has also been shown that a close approximation of such *a-priori* information also produces an improved reconstructed image. Finally, it has been demonstrated that given the present widely used sensitivity matrix which is calculated from a uniform conductivity distribution, together with a good approximation of the internal anatomy, it is possible to reconstruct

a much improved image of the internal conductivity distribution using an iterative method. This improved image is more accurate in a quantitative manner, where the calculated conductivity values are nearer to the actual tissue conductivity values.

## Chapter 5

### 5 Multi-frequency EIT image reconstruction

#### 5.1 Introduction

The methodology of two-dimensional electrical impedance tomography and single frequency image reconstruction has so far been discussed. In the work described previously in chapter 4, measurements are in practice taken at one single frequency, typically at 50 kHz and images are reconstructed assuming zero frequency. This assumption is valid if:

1. Quasi-static conditions are held. This assumption can be justified providing that the wavelength of the potential distribution within the bounded region under investigation is large compared with the maximum dimension of the volume. This allows the current present everywhere within this volume to vary in synchrony.
2. The current flow in the conductive distribution is only due to pure conductors and has no displacement component.

Techniques in the instrumentation have improved over the years since EIT was first proposed and consequently the range of usable frequencies over which measurements can be taken has also increased to cover a range of about 10 kHz to 1 MHz.

It has already been shown that tissue has a complex impedance. By the term complex it is meant that the impedance has both magnitude and phase. This complex impedance can be modelled by equation (1.3) as (Schwan 1957):

$$Z^* = R_{\infty} + \frac{R_0 - R_{\infty}}{\left(1 + \left(j \frac{f}{f_r}\right)^{1-\alpha}\right)} \quad (1.3)$$

where  $Z^*$  is the complex impedance,  $R_{\infty}$  is the very high frequency impedance,  $R_0$  is the low frequency impedance,  $f$  is the measurement frequency,  $f_r$  is the relaxation frequency for the tissue and  $\alpha$  is a constant that characterises the Cole-Cole distribution function for a particular tissue of interest.

From Chapter 1, at low frequencies, the measured impedance contains information about structures within both extracellular spaces and cell membranes. This information can be used to provide insight into tissue structure and changes in tissue structure under various pathological and physiological conditions. Above 100 kHz, the changes in permittivity of tissue will 'show' tumours (Fricke and Morse 1926, Surowiec et al 1988). Some EIT research groups have already published results using multi-frequency EIT (Riu et al 1992a, 1992b, Zhang and Griffiths 1990). Brown et al (1994b) are now making measurements over a range of frequencies with a view to reducing the effects of body geometry on the reconstructed images and are also in the hope that tissue can be characterised in terms of how the impedance varies with frequency.

In order to take advantage of all the information contained in complex tissue impedance, it is important to consider for the purpose of reconstruction, not only the real part of the complex measured boundary voltage but also the imaginary part. From multi-frequency impedance measurements of various tissues it should be possible to distinguish between various kinds of tissue and also assess the physiological state of a tissue under investigation.

Researchers have used multi-frequency EIT to look at tissue characterisation by reconstructing images of changes of conductivity at one frequency with respect to a reference frequency, usually the lowest measured frequency (Brown et al 1994a, 1994b, Lu et al 1995, Hampshire et al 1995). The used frequency range by these researchers is between 9.6 kHz and 1.2 MHz and images of differential conductivity changes are reconstructed with respect to data measured at 9.6 kHz.

Brown et al (1994a, b) have argued that due to stray capacitance the imaginary part of boundary voltage can not be accurately measured. These researchers have therefore only measured the real part of the boundary voltages for the purpose of image reconstruction. From these "real" (in-phase) measurements, they have reconstructed images of tissue conductivity (real part of conductivity only) changes with respect to frequency and from these images they have calculated tissue dependent characteristics (from Cole-Cole model) for a chosen region of interest. The images obtained using the above method have shown some reasonable success, as far as visual qualities of images are concerned. However, no quantitative analysis of this method has so far been performed to assess its

accuracy. This chapter will address the validity of this assumption by the use of FEM to assess the accuracy of reconstructed images when calculated complex boundary data are considered.

## 5.2 Method

The idealised 2D finite element model of the thorax is used for all of the following work, figure 5.1. The assumed conductivity and permittivity values used for each region within the model are shown in table 5.1 (Weast 1989).

**Table 5.1. Conductivity of permittivity values used in model of Figure 5.1.**

	Conductivity ( $\text{Sm}^{-1}$ )	Relative Permittivity
Muscle	0.74	18095
Lung	0.11	5000
Heart	1.16	18095

The procedure for modelling has already been described (Chapter 3) except that the analysis is now at 8 various frequencies over a range of 9.6 kHz to 1.2 MHz. A total of 16 electrodes have been placed around the phantom. Current is driven into the object through two adjacent (drive) electrodes. For each of the 16 drive-electrode pairs, 13 voltage differences between the remaining adjacent non-current carrying (receive) electrodes are recorded.

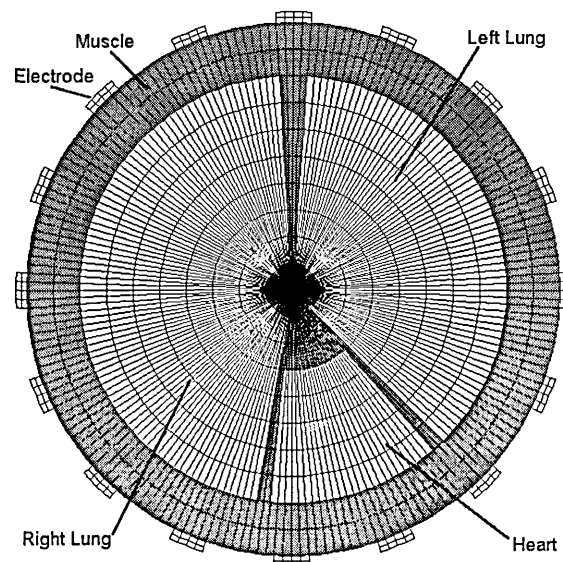


**Figure 5.1. The finite element model used. The central elements are not clear due to their small size.**

In the work described here the concept and method of image reconstruction using multi-frequency data will be given together with some reconstructed images using this technique. Also, the effects and importance of ignoring complex data by Brown et al (1994a, 1994b) will be investigated and highlighted.

### **5.2.1 Complex sensitivity matrix**

For a given frequency, the differential complex boundary voltage,  $\Delta g^*$ , is given by a modification of equation (4.2):

$$\Delta g^* = S^* \Delta c^* \quad (5.1)$$

where  $\Delta c^*$  is now the change in the complex conductivity or admittance from a reference complex conductivity and  $S^*$  is the complex sensitivity matrix for the given frequency. The complex boundary voltage can be expressed as:

$$g^* = g_{real} - jg_{imag} \quad (5.2)$$

and complex conductivity is given as:

$$c^* = c_{real} + jc_{imag} \quad (5.3)$$

or

$$c^* = \sigma + j\omega\epsilon \quad (5.4)$$

where  $\omega$  is the angular frequency of the applied current,  $\sigma$  is the conductivity for the given frequency and  $\epsilon$  the permittivity of the region.

It was seen from FEM analysis that the imaginary part of the calculated boundary voltage is negative in magnitude. This is important to note since most EIT instrumentation measure the absolute voltage difference between two receive electrodes rather than actual electrode voltages.

For a complex system, i.e. complex conductivity, an injected current at a given frequency will generate a complex electric field  $E^*$ , and hence a complex voltage,  $g^*$ ,

throughout the system. The complex sensitivity coefficient for a given pixel (i),  $S_i^*$ , is given by modifying equation (4.5):

$$S_i^* = - \int_u (E_{x_m}^*, E_{y_m}^*) \cdot (E_{x_n}^*, E_{y_n}^*) du \quad (5.6)$$

where for element i the electrical field ( $E_{x_m}^*$ ,  $E_{y_m}^*$ ) in element i is due to the current injected through electrode pair m and the electrical field ( $E_{x_n}^*$ ,  $E_{y_n}^*$ ) is that produced when the same current is injected through electrode pair n. (\*) denotes a complex (real and imaginary) variable.

Using a multi-frequency system (for example, the Sheffield MK3b system) where data is measured at eight different frequencies, from 9.2 kHz to 1228.8 kHz, there is a complex sensitivity matrix  $S^*$  for each of the measurement frequencies. This matrix relates the measured boundary voltages for a given frequency to the internal conductivity distribution. However, the boundary voltages are no longer a function of the internal conductivity distribution but also a function of the internal permittivity distribution and therefore a function of frequency.

The calculation of an inverse to the sensitivity matrix for the purpose of image reconstruction is as previously described for the single frequency case, and is given by modifying equation (4.20) to give:

$$\Delta c^* = [S^{*T} S^* + \lambda F_{\max} I]^{-1} S^{*T} \Delta g^* \quad (5.7)$$

In equation (5.7),  $S^{*T}$  denotes the conjugate transpose of  $S^*$ . This results in  $\lambda$  and  $F_{\max}$  being real only variables (no imaginary part) since the main diagonal of square matrix  $[S^{*T} S^*]$  is also real only.

$S^*$  has been calculated assuming the relationship in equation (5.2) is linear, i.e. any change in conductivity from a reference uniform conductivity (muscle tissue) is small.  $S^*$  calculated using this assumption will be referred to as  $S_{\text{unif}}^*$ , where the initial complex uniform conductivity is that of muscle, Table 5.1.

### 5.2.2 Reconstructed images of complex conductivity

For 8 frequencies, from 9.8 kHz to 1228.8 kHz, complex boundary data,  $g^*$ , have been calculated using FEM using methods described in chapter 3.  $S_{unif}^*$  has also been calculated for each frequency for a uniform reference complex conductivity of muscle tissue (Table 5.1), and images of internal conductivity distribution can be calculated using equation (5.7). Figure 5.2 shows the reconstructed images of real and imaginary part of the conductivity for each frequency, when  $\lambda=0.1$ .

It is observed from reconstructed images in figure 5.2 that the reconstructed images at each frequency are blurred as they were in the single frequency images and are similar to the images presented in Figure 4.10(b). This again is due to the fact that the matrix is near singular, and some regularisation is used. Since the conductivity was set to be constant over the range of frequency, the real part of the calculated conductivity is seen also to be constant over the range of frequency. The imaginary part of the calculated conductivity however, increases in proportion to the increasing frequency since from equation (5.4) the imaginary part of the conductivity is proportional to frequency.

In section 4.6.2 the idea of an ideal sensitivity matrix was introduced,  $S_{ideal}$ . By the term ideal, it is meant that full *a-priori* information about the internal conductivity distribution is taken into account in the calculation of the sensitivity matrix  $S_{ideal}$ . In this sense, by modifying equation (4.21) we can calculate the complex ideal sensitivity matrix  $S_{ideal}^*$ :

$$S_{ideal(i)}^* = - \int_u (Ex_m^*, Ey_m^*). (Hx_n^*, Hy_n^*) du \quad (5.8)$$

where for element  $i$  the complex electrical field components  $(Ex_m^*, Ey_m^*)$  in element  $i$  are due to the current injected through electrode pair  $m$  for the uniform conductivity. The electrical field components  $(Hx_n^*, Hy_n^*)$  are produced when the same current had been injected through electrode pair  $n$  after there has been a change in complex conductivity. That is from  $c_{ref}^*$  to  $c_{dat}^*$ , for pixel  $i$ , where  $c_{ref}^*$  is the uniform complex conductivity, and  $c_{dat}^*$  is the actual conductivity of pixel  $i$  for the thorax model used.

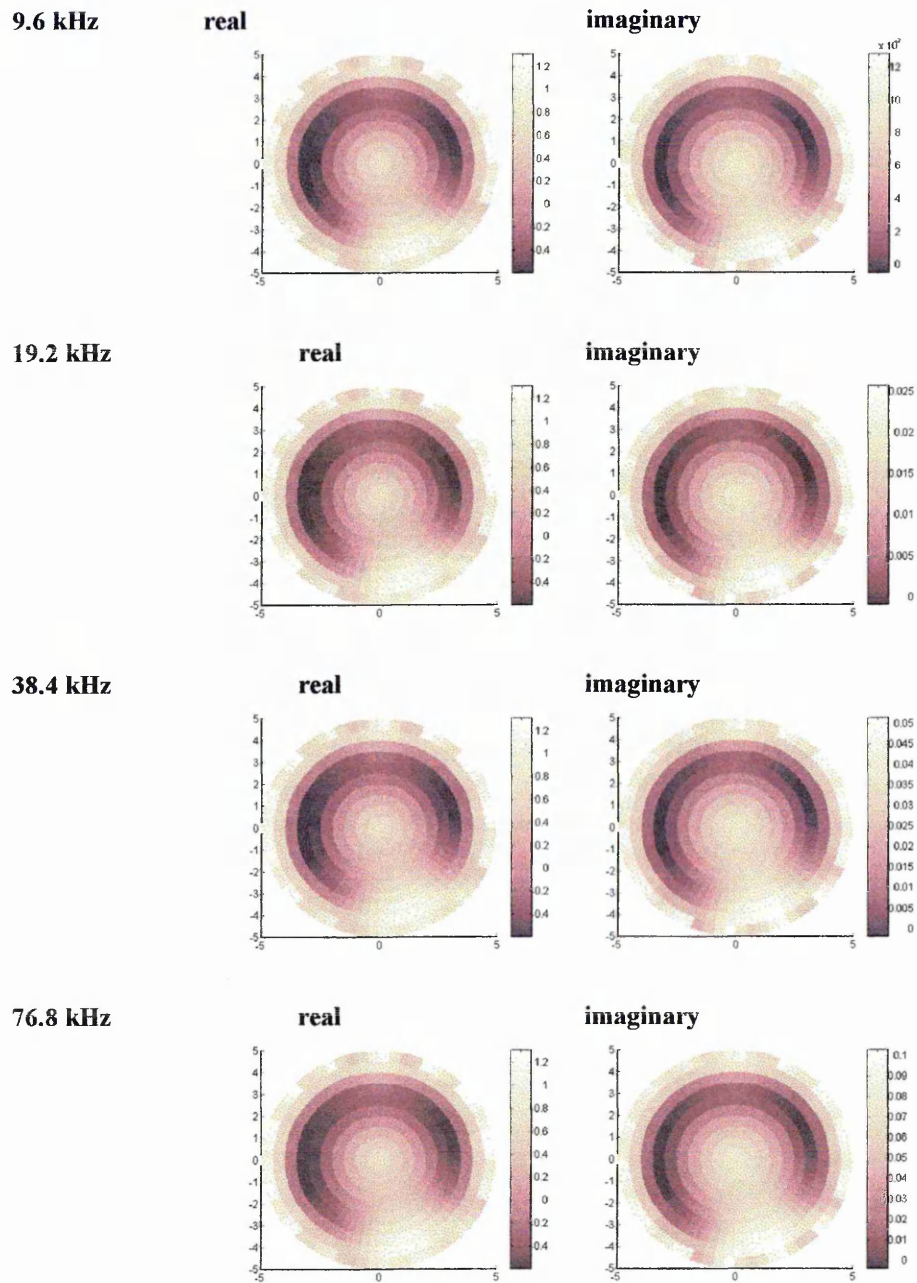
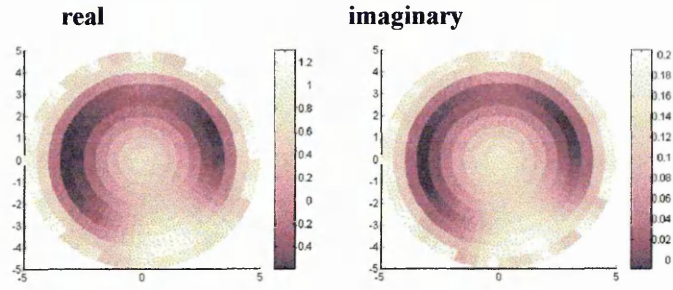
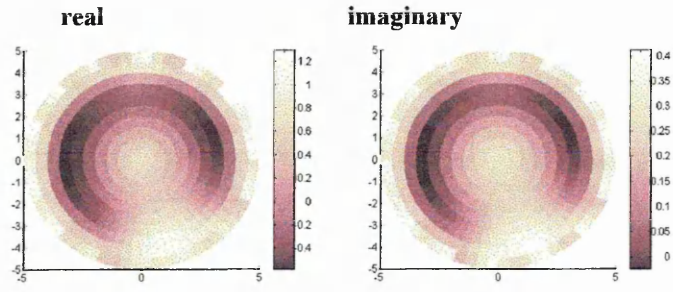


Figure 5.2(a) Reconstructed images of complex conductivity, real and imaginary parts, at 9.6 kHz, 19.2 kHz, 38.4 kHz and 76.8 kHz using  $S_{unif}$ .

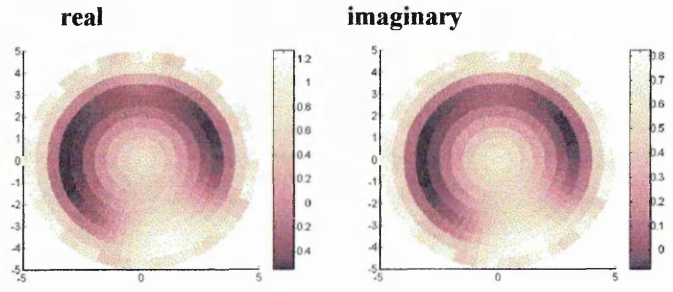
153.6 kHz



307.2 kHz



614.4 kHz



1228.8 kHz

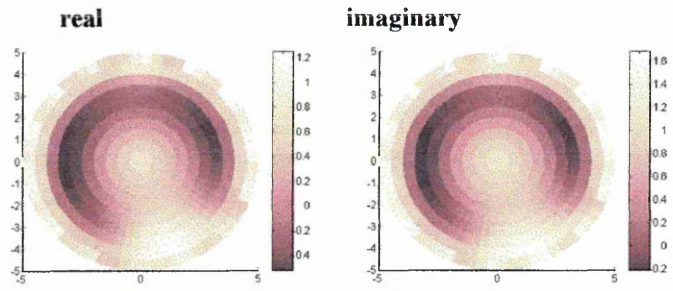


Figure 5.2(b) Reconstructed images of complex conductivity, real and imaginary parts, at 153.6 kHz, 307.2 kHz, 614.4 kHz and 1228.8 kHz using  $S_{unif}$ .

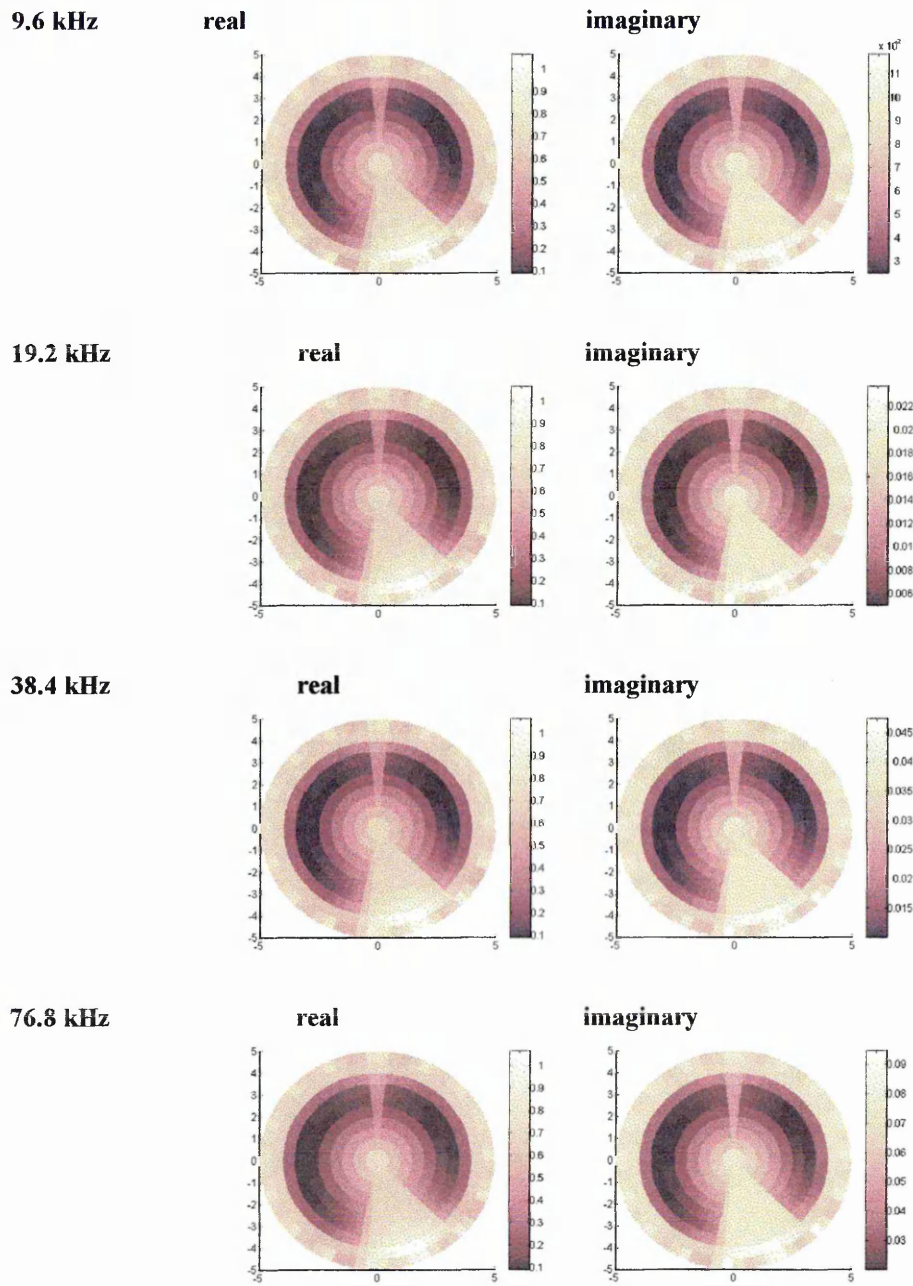
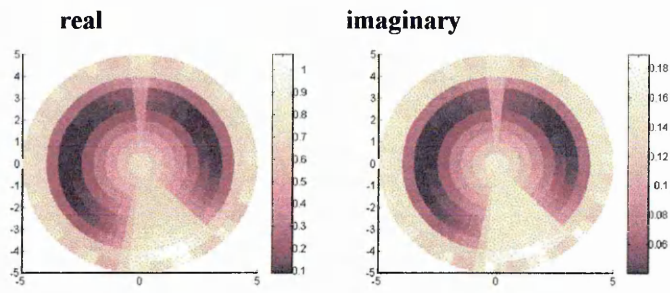
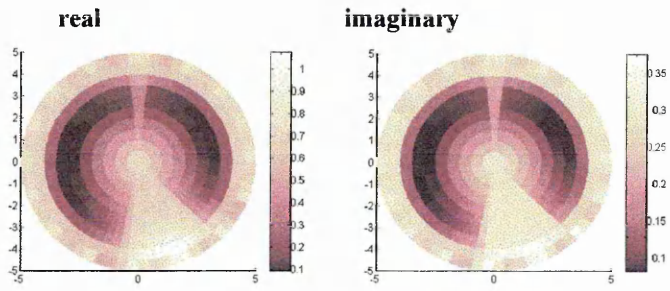


Figure 5.3(a) Reconstructed images of complex conductivity, real and imaginary parts, at 9.6 kHz, 19.2 kHz, 38.4 kHz and 76.8 kHz, using the ideal sensitivity matrix.

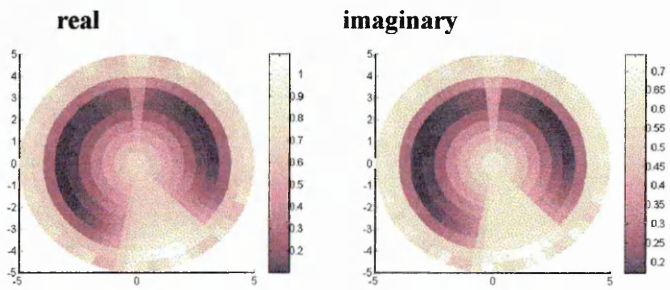
153.6 kHz



307.2 kHz



614.4 kHz



1228.8 kHz

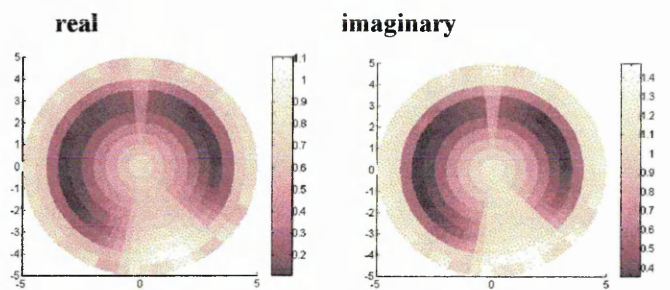


Figure 5.3(b) Reconstructed images of complex conductivity, real and imaginary parts, at 153.6 kHz, 307.2 kHz, 614.4 kHz and 1228.8 kHz, using the ideal sensitivity matrix.

Figure 5.3 shows reconstructed images when the complex ideal sensitivity matrix is used together with complex boundary data. The regularisation factor  $\lambda$  used in this case is also 0.1.

In Figure 5.3, the calculated conductivity is constant over a range of frequency. The imaginary part of the conductivity is again seen to be a function of frequency. The reconstructed images using  $\mathbf{S}_{ideal}^*$  are sharper than those seen in Figure 5.2 when no *a-priori* information is used. This was also seen in single frequency image reconstruction (section 4.6.2).

### **5.3 Frequency dependence of the complex sensitivity matrix**

In the calculation of the complex sensitivity coefficient  $\mathbf{S}_{unif}^*$  for pixel  $i$  equation (5.6) can be simplified by only considering the electric field in a given pixel:

$$S_i^* = E_m^* \cdot E_n^* \quad (5.9)$$

where for pixel  $i$ ,  $\mathbf{S}_i^*$  is the complex sensitivity coefficient,  $\mathbf{E}_m^*$  is the electric field due to current injected through electrode pair  $m$ , and  $\mathbf{E}_n^*$  is the electric field due to current injected through electrode pair  $n$ .

Since

$$J = E^* \sigma^* \quad (5.10)$$

where  $J$  is the total current density, then for pixel  $i$

$$\begin{aligned} E_m^* &= \frac{J_m}{\sigma_{real} + j\sigma_{imag}} \\ E_n^* &= \frac{J_n}{\sigma_{real} + j\sigma_{imag}} \end{aligned} \quad (5.11)$$

where  $J_m$  and  $J_n$  are the total current density due to the current injected through electrode pair  $m$  and due to the current injected through electrode pair  $n$  respectively.

and thus

$$\begin{aligned}
 E_m^* &= \frac{J_m}{\sigma_{real} + j\sigma_{imag}} \times \frac{\sigma_{real} - j\sigma_{imag}}{\sigma_{real} - j\sigma_{imag}} = \frac{J_m(\sigma_{real} - j\sigma_{imag})}{(\sigma_{real}^2 + \sigma_{imag}^2)} \\
 E_n^* &= \frac{J_n}{\sigma_{real} + j\sigma_{imag}} \times \frac{\sigma_{real} - j\sigma_{imag}}{\sigma_{real} - j\sigma_{imag}} = \frac{J_n(\sigma_{real} - j\sigma_{imag})}{(\sigma_{real}^2 + \sigma_{imag}^2)}
 \end{aligned} \tag{5.12}$$

hence

$$S_i^* = E_m^* \cdot E_n^* = J_m J_n \frac{(\sigma_{real}^2 - \sigma_{imag}^2 - j2\sigma_{real}\sigma_{imag})}{(\sigma_{real}^2 + \sigma_{imag}^2)^2} \tag{5.13}$$

However, in pixel i the sensitivity coefficient calculated at zero frequency in equation (4.5), can be written as

$$S_i = E_m \cdot E_n = \frac{J_m}{\sigma_{real}} \cdot \frac{J_n}{\sigma_{real}} = \frac{J_m J_n}{\sigma_{real}^2} \tag{5.14}$$

and therefore

$$\frac{S_i^*}{S_i} = \sigma_{real}^2 \frac{(\sigma_{real}^2 - \sigma_{imag}^2 - j2\sigma_{real}\sigma_{imag})}{(\sigma_{real}^2 + \sigma_{imag}^2)^2} \tag{5.15}$$

For a sensitivity matrix where linearity is assumed,  $\mathbf{S}_{unif}^*$ , there is a uniform conductivity throughout the region of interest. Then the relationship for any pixel can be expressed as:

$$\frac{S^*}{S} = \mu + j\gamma \tag{5.16}$$

where

$$\mu = \frac{\sigma_{real}^4}{(\sigma_{real}^2 + \sigma_{imag}^2)^2} \cdot \left(1 - \frac{\sigma_{imag}^2}{\sigma_{real}^2}\right) \tag{5.17}$$

and

$$\gamma = -\frac{\sigma_{real}^4}{(\sigma_{real}^2 + \sigma_{imag}^2)^2} \cdot \frac{2\sigma_{imag}}{\sigma_{real}} \quad (5.18)$$

The relationship described by equation (5.16) was previously described by Shallof (1997). However, the formula for  $\gamma$  presented by Shallof in his thesis is incorrect and the corrected version is shown in equation (5.18).

For a sensitivity matrix at any given frequency which has been calculated using electric fields from a uniform conductivity distribution, the complex scalar ( $\mu+j\gamma$ ) will be found to be equal for each and every pixel.

The complex scalars for eight different frequencies have been calculated using two methods:

1. Analytical : from equations (5.17) and (5.18). The values for the reference complex conductivity has been chosen from the assumed conductivity and permittivity of uniform conductivity consisting of muscle tissue (Table 5.1) and equation (5.4).
2. Numerical: from equation (5.16) where the complex sensitivity matrix has been calculated using the FEM.

Table 5.2 shows the calculated complex scalars using these two methods with Figure 5.4 showing a plot of these values for each frequency.

**Table 5.2 Complex scalar calculated using two methods for the sensitivity matrix at each frequency**

Numerical		Frequency (kHz)	Analytical	
$\mu$	$\gamma$		$\mu$	$\gamma$
0.9993	-0.0261	9.6	0.9995	-0.0261
0.998	-0.0522	19.2	0.998	-0.0522
0.9917	-0.1039	38.4	0.9919	-0.1039
0.9679	-0.2044	76.8	0.9678	-0.2045
0.8776	-0.3836	153.6	0.878	-0.3837
0.5981	-0.6057	307.2	0.5982	-0.6058
0.1045	-0.5794	614.4	0.1045	-0.5794
-0.1246	-0.2321	1228.8	-0.1246	-0.2327

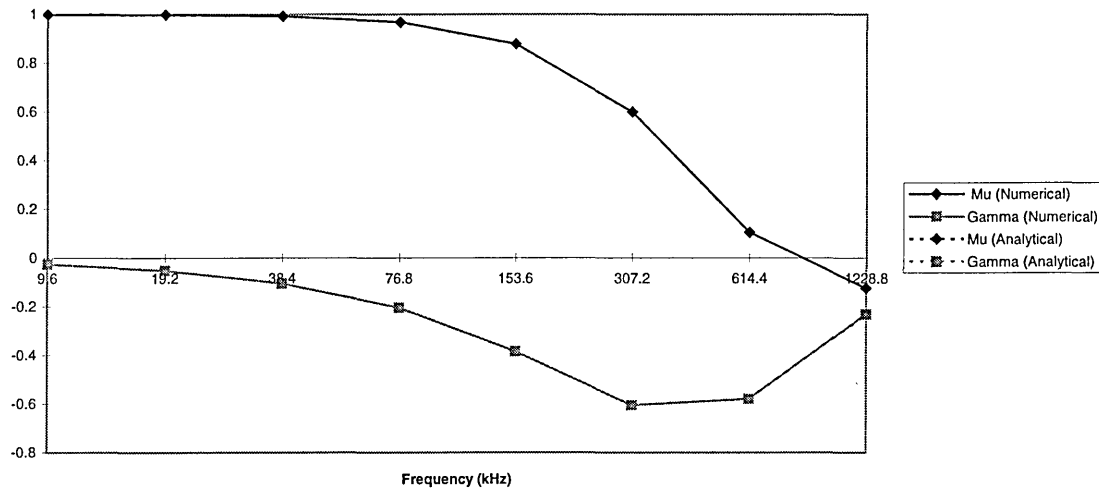


**Figure 5.4 Plot of the complex scalar ( $\mu$  and  $\gamma$ ) with frequency**

From the results shown in Table 5.2 and Figure 5.4, it is evident that there exists a relationship between the complex sensitivity matrix at any given frequency and the sensitivity matrix calculated at zero frequency. Both methods used to calculate this relationship, numerical and analytical, produce the same results. The real part of the complex scalar  $\mu$  decreases with frequency, and is negative in magnitude at the highest frequency. The imaginary part  $\gamma$  is negative with a peak in magnitude at 307.2 kHz.

It is possible, therefore, that given a sensitivity matrix calculated from the uniform reference conductivity distribution at zero frequency, and the complex conductivity coefficients  $\sigma_{\text{real}}$  and  $\sigma_{\text{imag}}$ , a complex sensitivity matrix can be calculated for any frequency from equation (5.16). This calculated complex sensitivity matrix can then be used with complex boundary voltages for the calculation of internal conductivity distribution.

#### **5.4 Complex boundary voltages: importance of the imaginary part**

We have earlier shown that images of the complex conductivity can be reconstructed using the complex boundary voltages and complex sensitivity matrix for a given frequency. Brown et al (1994a, 1994b) have argued that due to stray capacitance the imaginary part of boundary voltage cannot be accurately be measured. They have therefore used only the real part of the measured boundary voltage and a real only sensitivity matrix (one calculated assuming zero frequency) for the purpose of image

reconstruction. The importance of ignoring the imaginary part of the voltage will be investigated next.

As an initial comparison, images were reconstructed for each measurement frequency using the complex sensitivity matrix for each given frequency and only the real part of the calculated boundary voltages for that given frequency, rather than complex boundary voltages and the complex sensitivity matrix which were shown in Figure 5.2. The reconstructed images are shown in Figure 5.5.

It can be seen from the reconstructed images that the imaginary part of the calculated conductivity is no longer accurate. Also the real part of the calculated conductivity is no longer constant over the range of the used frequency.

In Figure 5.5 imaginary components of the conductivity are also shown. These are calculated since the complex sensitivity matrix used at each frequency itself has a real and imaginary component and using a real only boundary voltages with these complex sensitivity matrices will result in both real and imaginary calculated conductivity. The imaginary part of the calculated conductivity is however inaccurate.

Next, images have been reconstructed for two different cases in three different categories. The three categories are when:

1. full *a-priori* knowledge about the conductivity distribution is known and the corresponding complex sensitivity matrix,  $\mathbf{S}_{\text{ideal}}^*$ , is used,
2. no *a-priori* knowledge is used and the complex sensitivity matrix,  $\mathbf{S}_{\text{unif}}^*$ , is used,
3. no *a-priori* knowledge is used and a real only (zero frequency) sensitivity matrix,  $\mathbf{S}$ , is used for all frequencies.

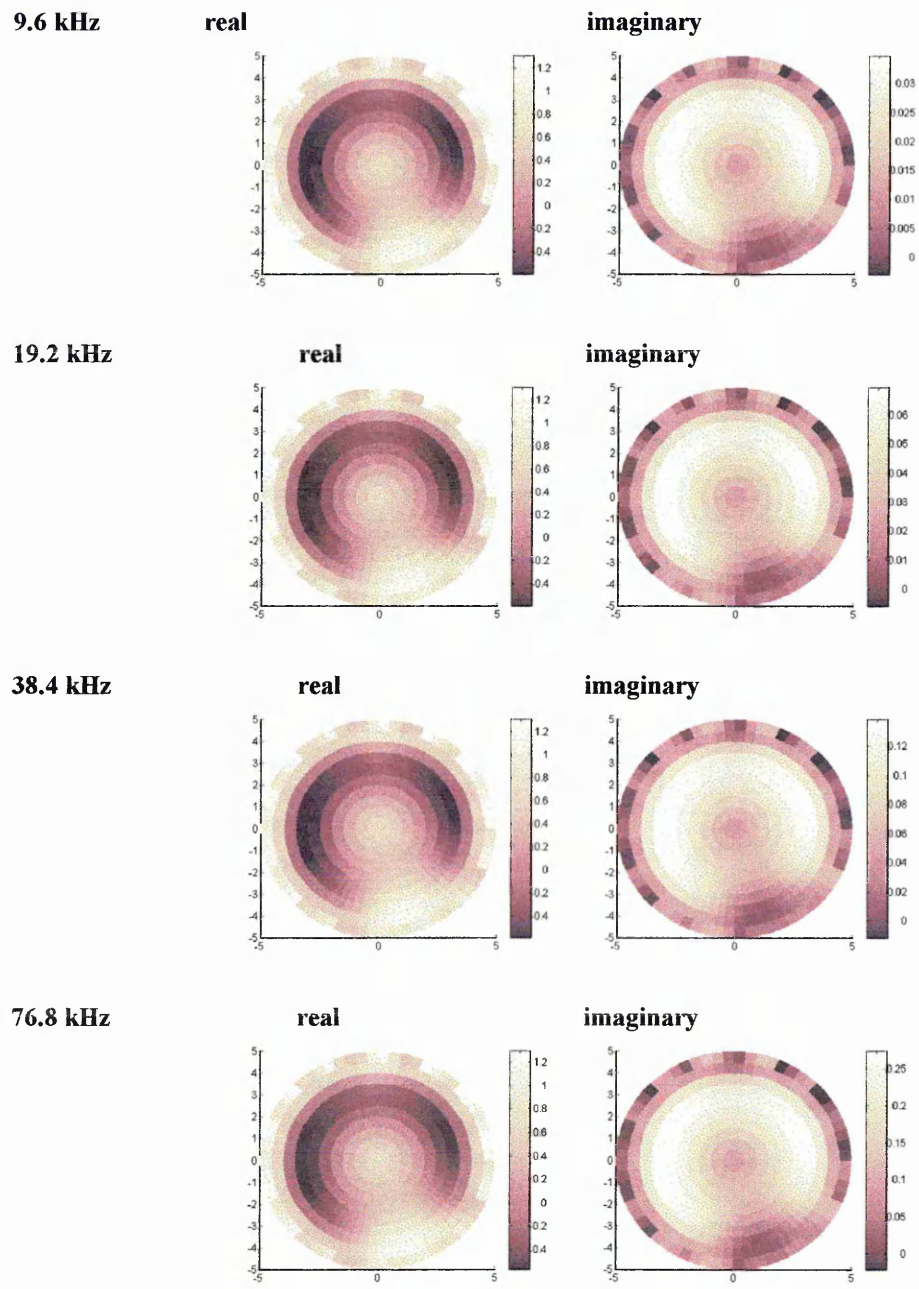
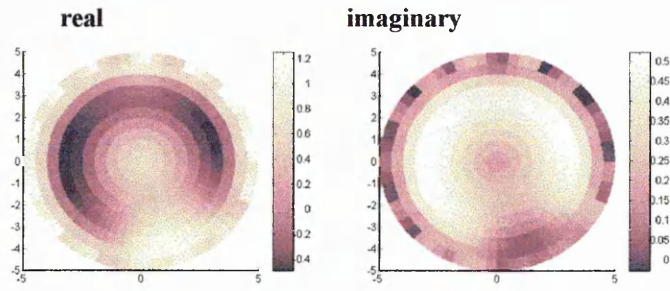
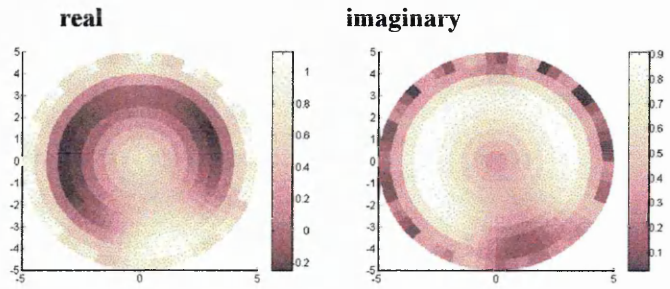


**Figure 5.5(a) Reconstructed images of complex conductivity, real and imaginary parts, at 9.6 kHz, 19.2 kHz, 38.4 kHz and 76.8 kHz, using complex sensitivity matrix and the real only boundary voltage at the given frequency.**

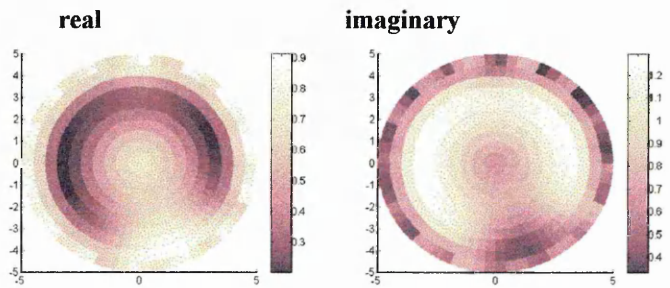
153.6 kHz



307.2 kHz



614.4 kHz



1228.8 kHz

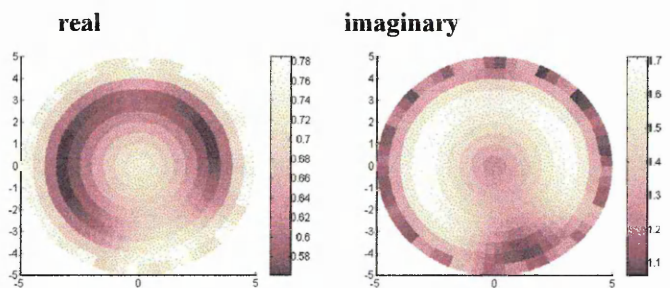


Figure 5.5(b) Reconstructed images of complex conductivity, real and imaginary parts, at 153.6 kHz, 307.2 kHz, 614.4 kHz and 1228.8 kHz, using complex sensitivity matrix and the real only boundary voltage at the given frequency.

The two cases are:

- a. real only boundary voltage,  $g_{\text{real}}$ , is used.
- b. complex voltage,  $g^*$ , is used.

The *a-priori* information used for the calculation of the complex sensitivity matrix  $S_{\text{ideal}}^*$  are the anatomical information of the model being imaged together with the complex conductivity for each pixel in the model. It is self evident that, given the full *a-priori* information about the model being imaged, no imaging is needed as discussed in section 4.6. However, this will serve as a useful benchmark for the best results possible and will show the effects of regularisation in the calculation of an inverse to the problem.

Two sets of boundary data have been calculated using FEM for use in this work. The first is when lungs are modelled as being inflated, where the conductivity is chosen as  $0.11 \text{ Sm}^{-1}$ , and when the lungs are modelled as being deflated where the conductivity is chosen as  $0.33 \text{ Sm}^{-1}$ . All other tissue properties are as previously stated in Table 5.1. Two regularisation factors of  $\lambda = 0.1$  and  $\lambda = 0.01$  are used in the image reconstruction.

From the forward model, pixels occupied by each region within the thorax model are known. From this and the reconstructed images, it is possible to calculate an average value of conductivity for each region for the purpose of comparison with actual values in the forward model used in FEM. Figures 5.6 - 5.15 show the calculated conductivity within each region of the reconstructed images for each of the two cases and three categories. Note that only figures 5.6, 5.7, 5.10 and 5.11 contain data from the modelled deflated lungs.

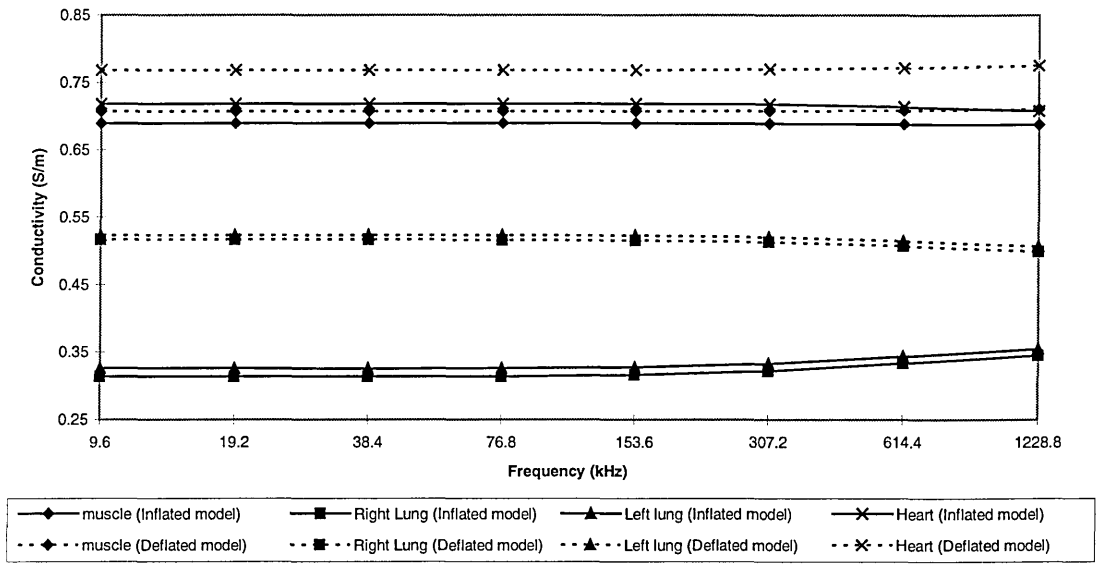


**Figure 5.6 Complex sensitivity matrix, a-priori information and  $g^*$ ,  $\lambda=0.1$ .**  
**Lung Inflated =  $0.11 \text{ Sm}^{-1}$ . Lung Deflated =  $0.33 \text{ Sm}^{-1}$ . Muscle =  $0.74 \text{ Sm}^{-1}$ . Heart =  $1.16 \text{ Sm}^{-1}$ .**

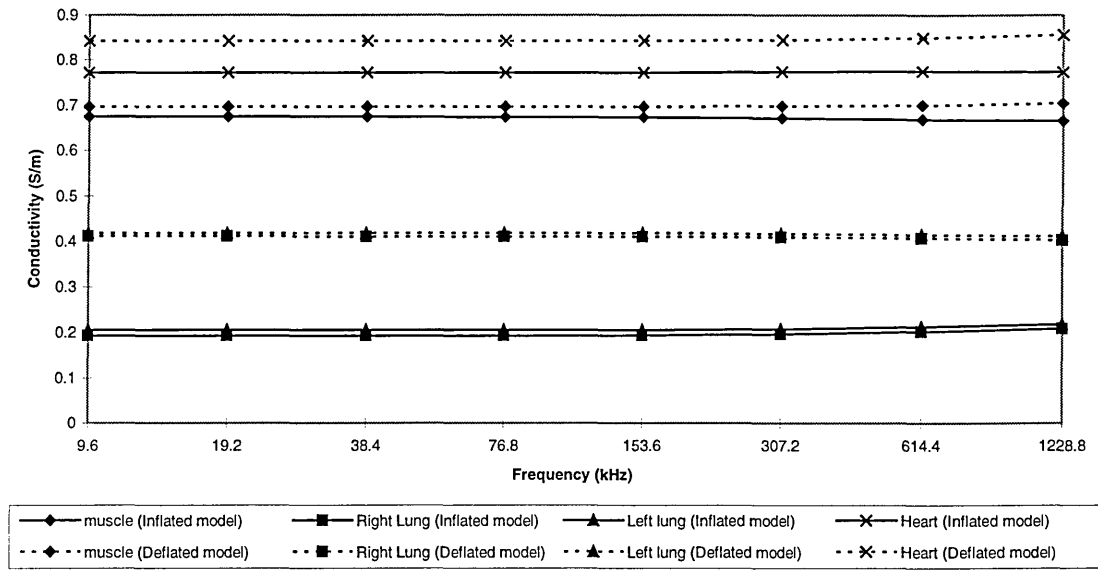
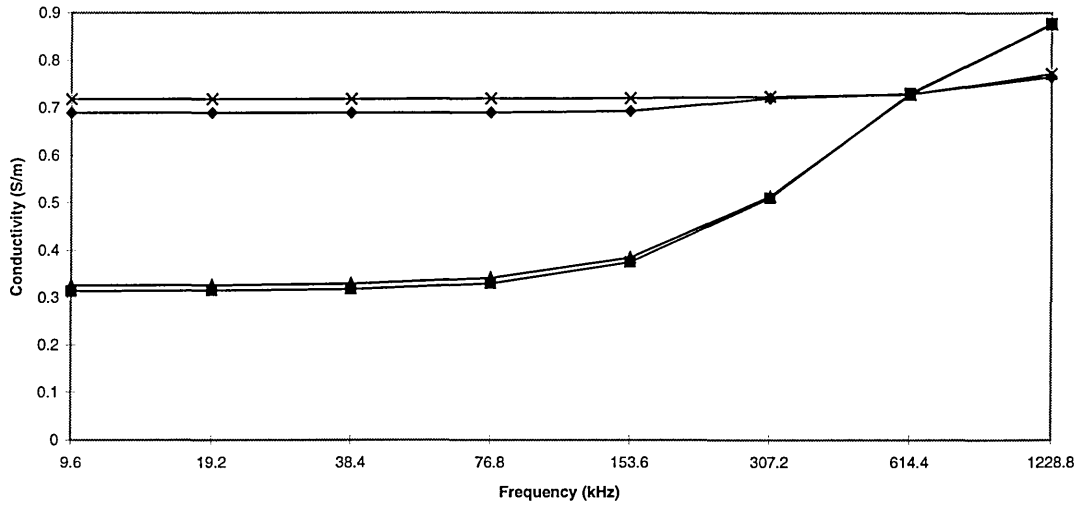
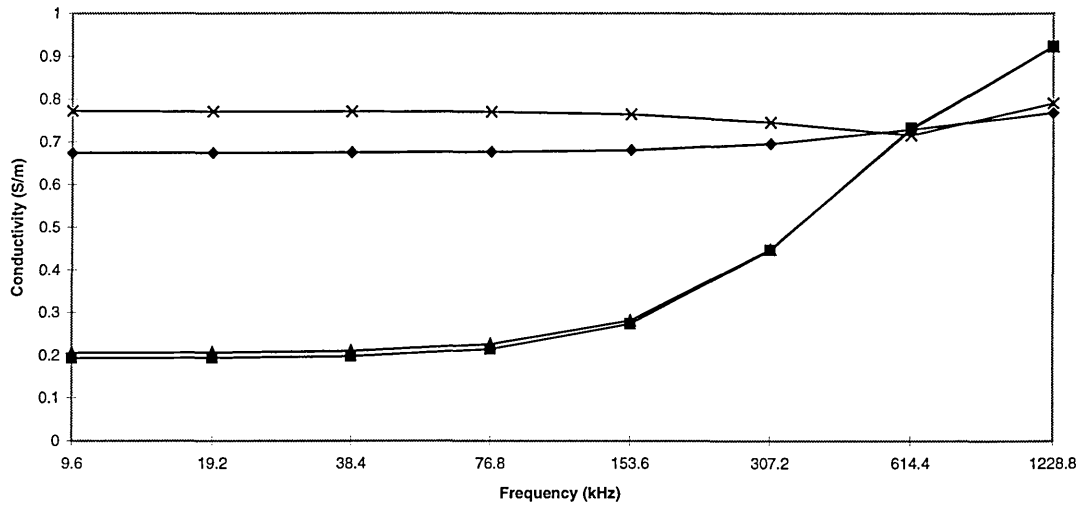


**Figure 5.7 Complex sensitivity matrix, a-priori information and  $g^*$ ,  $\lambda=0.01$ .**  
**Lung Inflated =  $0.11 \text{ Sm}^{-1}$ . Lung Deflated =  $0.33 \text{ Sm}^{-1}$ . Muscle =  $0.74 \text{ Sm}^{-1}$ . Heart =  $1.16 \text{ Sm}^{-1}$ .**



◆ muscle (Inflated model)    ■ Right Lung (Inflated model)    ▲ Left lung (Inflated model)    ✕ Heart (Inflated model)

**Figure 5.8 Complex sensitivity matrix, a-priori information and  $g_{\text{real}}$ ,  $\lambda=0.1$**   
**Lung Inflated =  $0.11 \text{ Sm}^{-1}$ . Muscle =  $0.74 \text{ Sm}^{-1}$ . Heart =  $1.16 \text{ Sm}^{-1}$ .**



◆ muscle (Inflated model)    ■ Right Lung (Inflated model)    ▲ Left lung (Inflated model)    ✕ Heart (Inflated model)

**Figure 5.9 Complex sensitivity matrix, a-priori information and  $g_{\text{real}}$ ,  $\lambda=0.01$**   
**Lung Inflated =  $0.11 \text{ Sm}^{-1}$ . Muscle =  $0.74 \text{ Sm}^{-1}$ . Heart =  $1.16 \text{ Sm}^{-1}$ .**

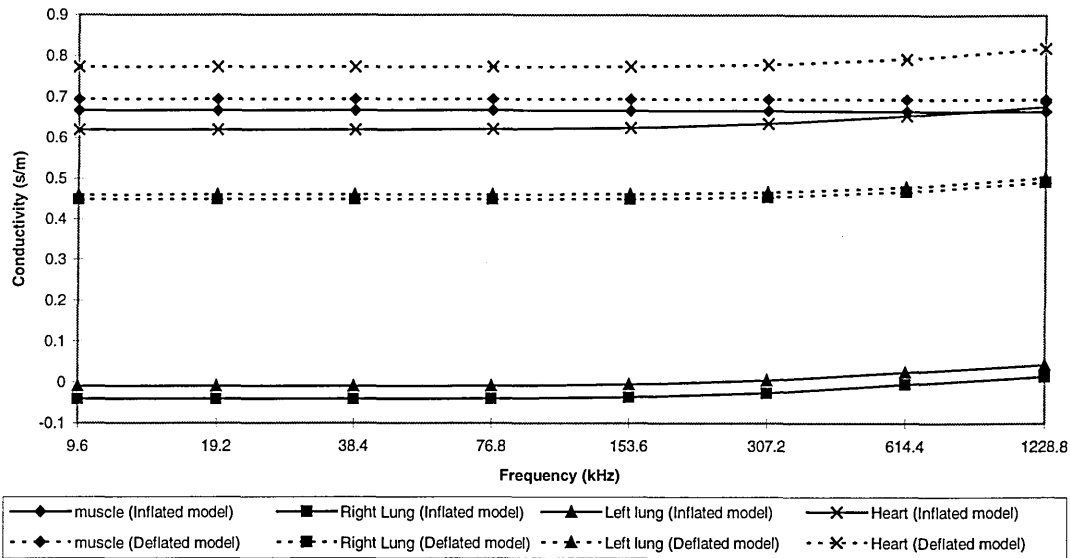


**Figure 5.10 Complex sensitivity matrix, no a-priori information and  $g^*$ ,  $\lambda=0.1$**   
**Lung Inflated =  $0.11 \text{ Sm}^{-1}$ . Lung Deflated =  $0.33 \text{ Sm}^{-1}$ . Muscle =  $0.74 \text{ Sm}^{-1}$ . Heart =  $1.16 \text{ Sm}^{-1}$ .**

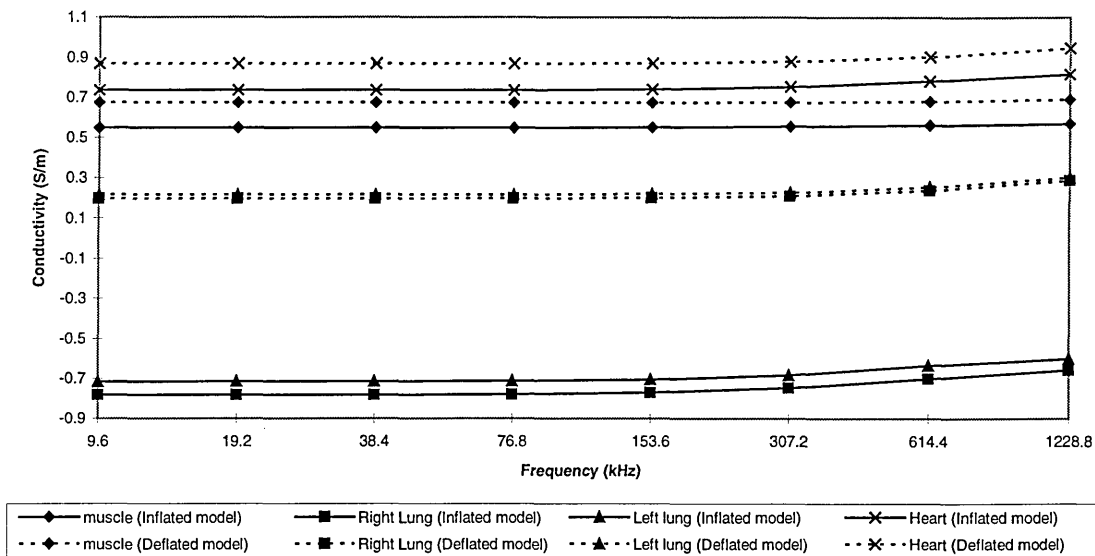


**Figure 5.11 Complex sensitivity matrix, no a-priori information and  $g^*$ ,  $\lambda=0.01$**   
**Lung Inflated =  $0.11 \text{ Sm}^{-1}$ . Lung Deflated =  $0.33 \text{ Sm}^{-1}$ . Muscle =  $0.74 \text{ Sm}^{-1}$ . Heart =  $1.16 \text{ Sm}^{-1}$ .**

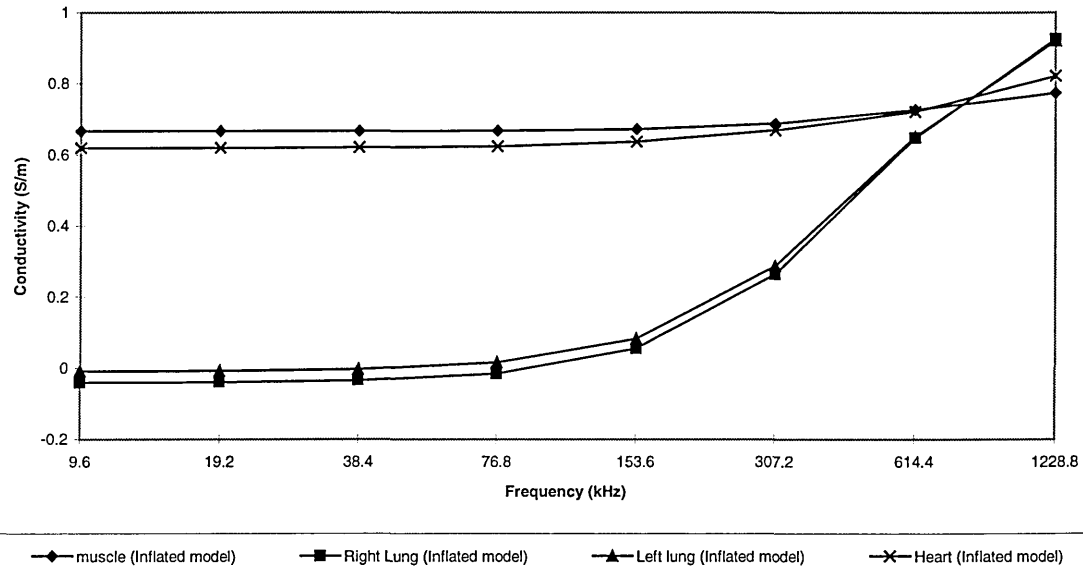


**Figure 5.12** Complex sensitivity matrix, no a-priori information and  $g_{real}, \lambda=0.1$   
 Lung Inflated =  $0.11 \text{ Sm}^{-1}$ . Muscle =  $0.74 \text{ Sm}^{-1}$ . Heart =  $1.16 \text{ Sm}^{-1}$ .

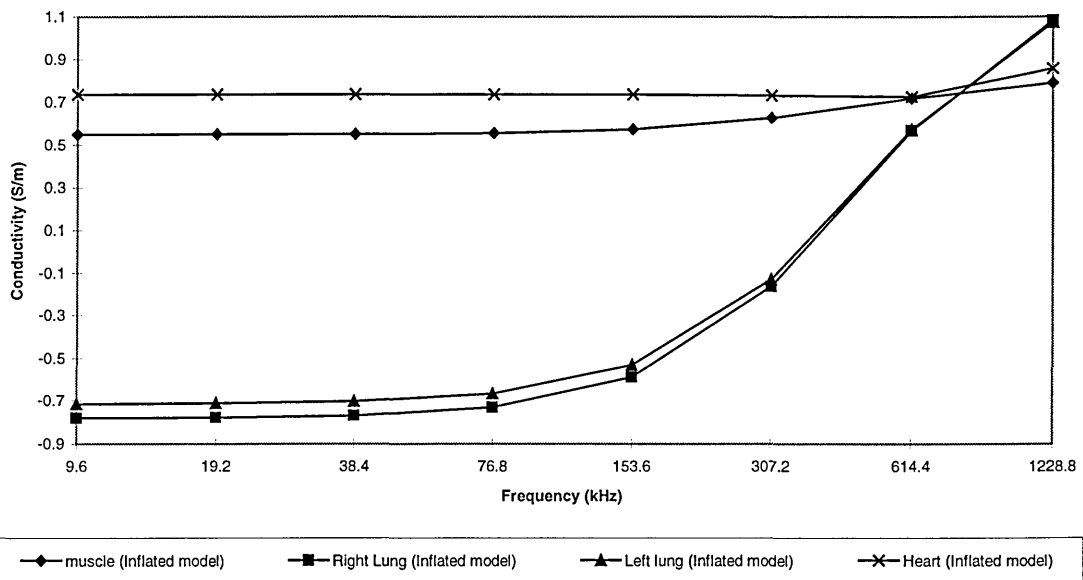


**Figure 5.13** Complex sensitivity matrix, no a-priori information and  $g_{real}, \lambda=0.01$   
 Lung Inflated =  $0.11 \text{ Sm}^{-1}$ . Muscle =  $0.74 \text{ Sm}^{-1}$ . Heart =  $1.16 \text{ Sm}^{-1}$ .

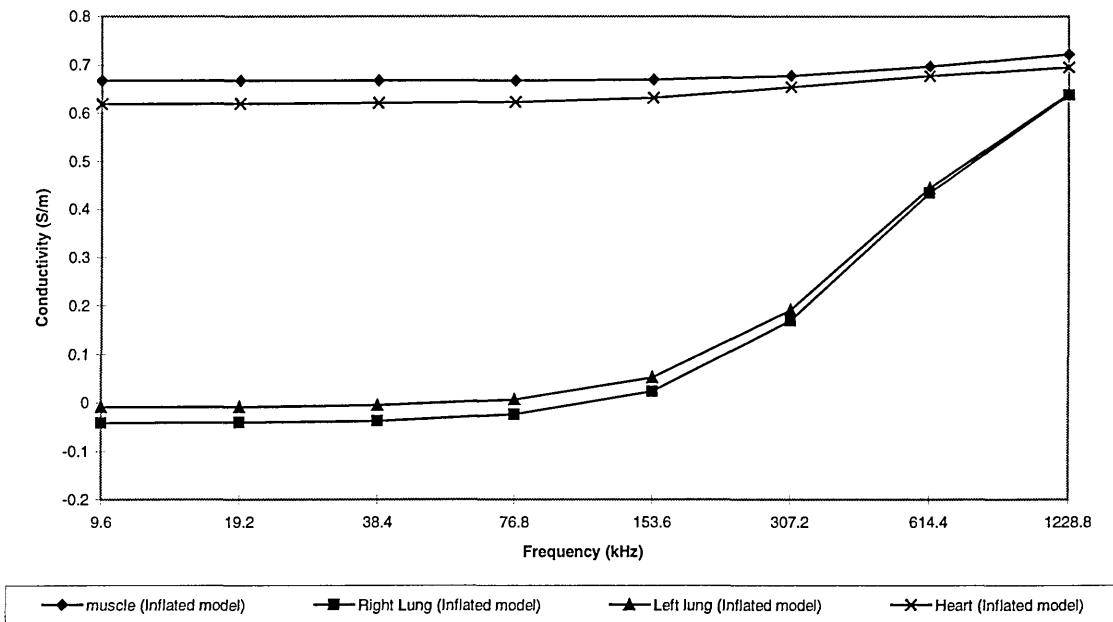


Figure 5.14 Real only sensitivity matrix, no a-priori information and  $g^*$ ,  $\lambda=0.1$  and Real only sensitivity matrix, no a-priori information and  $g_{\text{real}}$ ,  $\lambda=0.1$ . Note both real and complex data give same results.

Lung Inflated =  $0.11 \text{ Sm}^{-1}$ . Muscle =  $0.74 \text{ Sm}^{-1}$ . Heart =  $1.16 \text{ Sm}^{-1}$ .

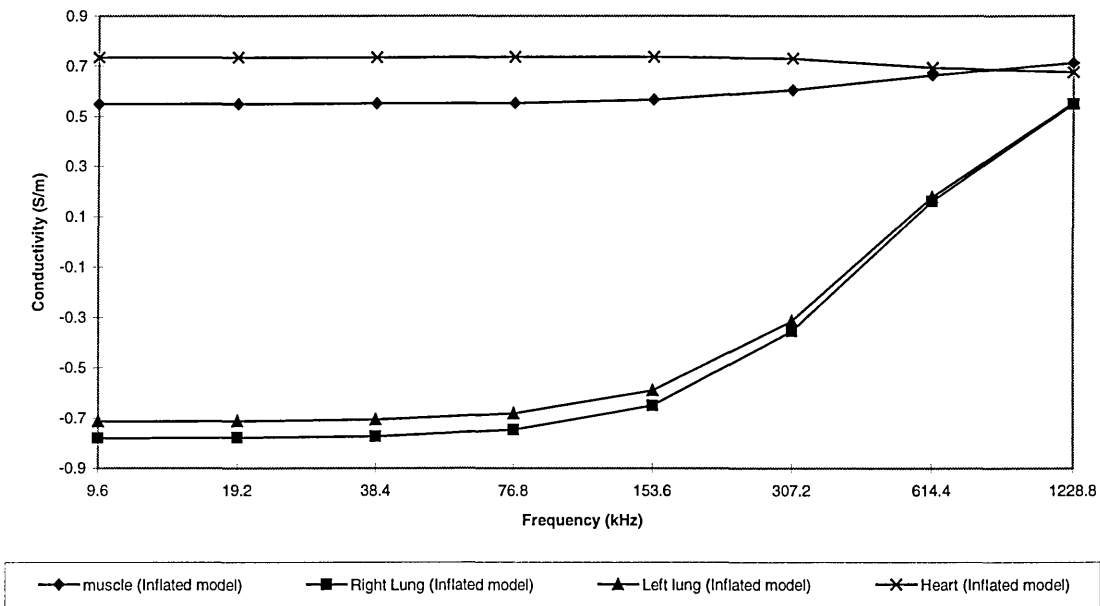


Figure 5.15 Real only sensitivity matrix, no a-priori information and  $g^*$ ,  $\lambda=0.01$  and Real only sensitivity matrix, no a-priori information and  $g_{\text{real}}$ ,  $\lambda=0.01$ . Note both real and complex data give same results.

Lung Inflated =  $0.11 \text{ Sm}^{-1}$ . Muscle =  $0.74 \text{ Sm}^{-1}$ . Heart =  $1.16 \text{ Sm}^{-1}$ .

From Figures 5.6 - 5.9 when *a-priori* information is used, it is clearly evident that for a constant conductivity over a range of frequency, if the imaginary part of the complex boundary voltages is ignored then the calculated conductivity is no longer constant over the range of used frequency. For the full *a-priori* information sensitivity matrix and complex data, Figures 5.6 and 5.7, the calculated actual conductivity appears more accurate if a smaller value of regularisation is used. When a change in conductivity of the lungs is modelled, that is from inflated to deflated, representing an actual conductivity change of  $0.22 \text{ Sm}^{-1}$ , the calculated change of conductivity is reconstructed with a good degree of accuracy (calculated as  $0.2 \text{ Sm}^{-1}$  when  $\lambda = 0.1$  and as  $0.22 \text{ Sm}^{-1}$  when  $\lambda = 0.01$ ) when using the *a-priori* information for both values of  $\lambda$ .

From Figures 5.10 - 5.13 where no *a-priori* information is used, it is again clearly evident that for a constant actual conductivity over a range of frequency, if the imaginary part of the complex boundary voltages is ignored, the calculated conductivity is no longer constant over the range of used frequency. Also when no *a-priori* information is used, the calculated conductivity value for each region of the model is further away from the actual conductivity values used in the forward model. This inaccuracy increases with decreasing value of  $\lambda$ . More importantly, when a change in conductivity of the lungs is modelled, that is from inflated to deflated, representing an actual conductivity change of  $0.22 \text{ Sm}^{-1}$ , the calculated change of conductivity is not reconstructed with any degree of accuracy (calculated as  $0.48 \text{ Sm}^{-1}$  when  $\lambda = 0.1$  and as  $0.97 \text{ Sm}^{-1}$  when  $\lambda = 0.01$ ) when using no *a-priori* information for both values of  $\lambda$ .

Finally from Figures 5.14 and 5.15, it can be seen that with or without ignoring the imaginary part of the complex boundary voltage, when a real only sensitivity matrix (sensitivity matrix calculated at zero frequency) is used for the purpose of image reconstruction, for any given value of  $\lambda$ , the calculated actual conductivity for the lungs is no longer constant over a range of frequencies.

### **5.4.1 Discussion**

In multi-frequency EIT, when measurements are made over a range of frequencies, both the real and imaginary parts of the boundary voltages are needed together with the complex sensitivity matrices for each measurement frequency for accurate image reconstruction. The degree of accuracy is greatly increased when *a-priori* information about the region under investigation is utilised.

### **5.5 Image reconstruction and the Cole-Cole model**

The work described so far in this chapter has only concentrated on imaging the internal conductivity of regions whose true conductivity is not a function of frequency. This maybe true for industrial tomography applications, where material conductivity is constant irrespective of the used frequency. However, in medical applications, biological tissue have a conductivity which is a function of the measurement frequency (section 1.5). The work therefore requires investigation of the calculated conductivity of biological tissue whose actual true conductivity is not constant over the range of applied frequency.

In section 1.5, the mathematical model based on the Cole-Cole model of biological tissue was given as:

$$Z^* = R_\infty + \frac{R_0 - R_\infty}{(1 + (j \frac{f}{f_r})^{(1-\alpha)})} \quad (1.3)$$

where  $Z^*$  is the complex impedance,  $R_\infty$  is the very high frequency impedance,  $R_0$  is the low frequency impedance,  $f$  is the measurement frequency,  $f_r$  is the relaxation frequency for the tissue and  $\alpha$  is the constant that characterises the Cole-Cole distribution function.

Brown et al (1994a, 1994b) and Lu et al (1995) have used this equation and the measurements made over a range of frequency to calculate the ratio of extracellular to intracellular fluid and also the characteristic frequency for a region of interest in a reconstructed image of conductivity. They have however, stated that only the real part of the impedance is measured as the imaginary part cannot be accurately measured due

to stray and body capacitance. Not only do they ignore the imaginary data but they also only use a sensitivity matrix calculated at zero frequency (real only matrix) for image reconstruction. Their method of imaging is differential where images of the normalised changes of conductivity are calculated with respect to the lowest frequency of measurement.

In the following section of this chapter the validity of the assumptions by Brown et al (1994a, 1994b) and Lu et al (1995) will be investigated with respect to the parametric images they have presented.

### **5.5.1 Method**

It has already been demonstrated that both the real and imaginary part of the voltage are crucial for accurate image reconstruction together with a sensitivity matrix for the measurement frequency. In the previous section a conductivity value for lungs were chosen which was constant over the range of frequency, however, from equation (1.3) it is evident that the conductivity of tissue changes with frequency.

From equation (1.3) and from published data (Brown et al 1994b) it is possible to calculate typical conductivity and permittivity of lung tissue for each measurement frequency, Table 5.3.

**Table 5.3 Conductivity and permittivity of lung tissue as a function of frequency**

Frequency kHz	Conductivity $\text{Sm}^{-1}$	Relative permittivity
9.6	0.1177	20700
19.2	0.1230	15100
38.4	0.1314	10300
76.8	0.1438	6320
153.6	0.1589	3380
307.2	0.1738	1550
614.4	0.1857	623
1228.8	0.1937	226

From Table 5.3 it can be seen that the conductivity of lung tissue increases slightly with frequency while its permittivity decreases rapidly. These values were used together with the values shown in Table 5.1 for the other tissues in the thorax model to generate complex data for each of the measurement frequencies. These boundary voltages were then used to calculate the change in conductivity of lung region with reference to the

lowest frequency conductivity value of the lungs, using the method employed by Brown et al (1994b). These images of change in conductivity are given by:

$$\Re \left[ \frac{c_{(i)}^* - c_{(1)}^*}{c_{(1)}^*} \right] \approx \left( \frac{S_{unif}}{g_{real(1)}} \right)^{-1} \frac{g_{real(i)} - g_{real(1)}}{g_{real(1)}} \quad (5.19)$$

where  $\Re$  represents the real part only,  $g_{real(1)}$  is the real part of the boundary voltage measured at the lowest frequency (9.6 kHz),  $g_{real(i)}$  is the real part of the voltage measured at the  $i^{th}$  measurement frequency,  $c_{(1)}^*$  is the complex conductivity at the lowest frequency,  $c_{(i)}^*$  is the complex conductivity at the measurement frequency and  $S_{unif}$  is the real only (zero frequency) sensitivity matrix.

The data are normalised with respect to the lowest frequency measurements to allow for unknown electrode placement and geometry.

Figure 5.16 shows the calculated change in real part of the conductivity as well as the actual change in conductivity with reference to the lowest frequency.

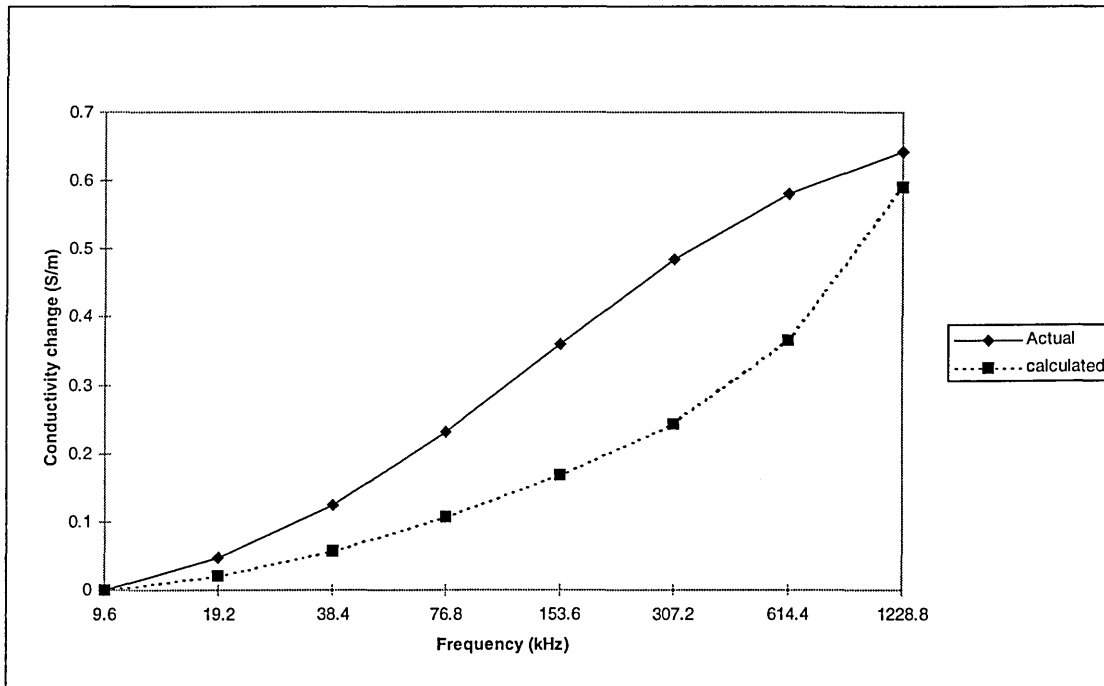


Figure 5.16 Graph showing the calculated real part of the normalised change in conductivity and the real part of the actual change in conductivity.

From Figure 5.16 it can be seen that even though the calculated change in conductivity is not very far from the actual change, the shape of the response itself is different. In practice parameters to the Cole-Cole model, for example the characteristic frequency  $f_r$ , are calculated from the reconstructed changes of conductivity for a chosen region of interest or pixel (Brown et al 1994a, 1994b, Lu et al 1995). The characteristic frequency by itself is the favoured extractable parameter from the reconstructed images, since it is the only parameter that can be independently calculated and it is not a relative parameter, i.e. it has units (Hz). It is evident from the results shown in Figure 5.16 that if the characteristic frequency is calculated for the reconstructed images using the method of Brown et al (1994a), (1994b) and Lu et al (1995) it will be significantly different to the actual characteristic frequency of the tissue under investigation.

It has been argued that complex data will be needed for a more accurate parametric imaging (section 5.4). If the imaginary part of the boundary voltage can be accurately measured, complex sensitivity matrices are needed for each measurement frequency. It has already been demonstrated in section (5.3) that the complex sensitivity matrix  $S_{unif}^*$  can be given by:

$$S_{unif}^* = (\mu + j\gamma)S_{unif} \quad (5.20)$$

Equation (5.20) together with complex boundary voltage  $g^*$  can be used to modify equation (5.19) to give:

$$\frac{c_{(i)}^* - c_{(1)}^*}{c_1^*} \approx \left( \frac{S_{unif}^*}{g_{(1)}^*} \right)^{-1} \frac{g_{(i)}^* (\mu_{(i)} + j\gamma_{(i)})^{-1} - g_{(1)}^* (\mu_{(1)} + j\gamma_{(1)})^{-1}}{g_{(1)}^*} \quad (5.21)$$

where (i) represents measurement frequency, and (1) the lowest frequency measurements.

In equation (5.21), not only are the complex voltages considered but the complexity of the sensitivity matrix will also be taken into account.

Equation (5.21) is used to calculate the change in complex conductivity with respect to lowest frequency, and the real part is then compared to the real part of the true actual change in conductivity of the forward model. These are shown in Figure 5.17.

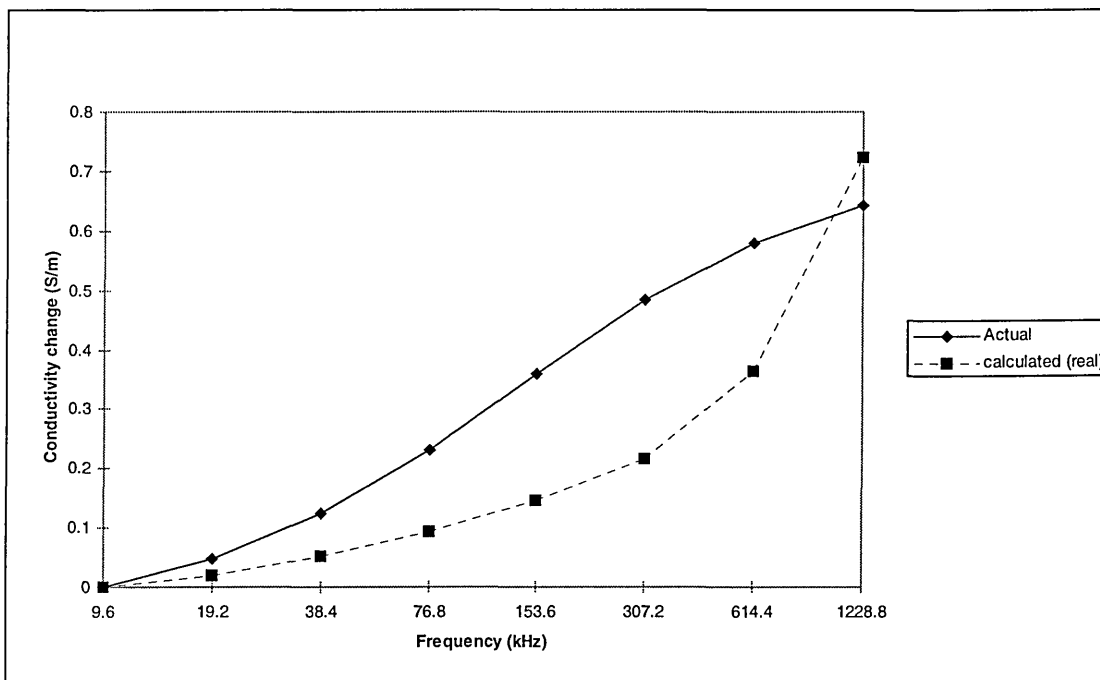


**Figure 5.17** Graph of the real part of the calculated change in conductivity of the lung regions using complex data and sensitivity matrix, and the real part of the actual change in conductivity in the forward model, both referenced to the lowest frequency value.

From Figure 5.17 it again can be seen that the calculated change in conductivity is different to the actual change. This again would result in the wrong calculation of parameters such as the characteristic frequency of the regions.

## **5.6 Conclusions**

In multi-frequency EIT, due to the complex tissue conductivity, any resultant boundary voltage due to a constant magnitude modulated current will also be complex in nature (magnitude and phase). To gain maximum advantage from such a system, not only are the magnitude of these boundary voltages needed but the phase is also crucial. For image reconstruction, as well as the complex boundary voltages, a complex sensitivity matrix for each frequency is also needed. This has been shown in cases where a constant conductivity over a range of frequency is imaged. Images reconstructed from real only components have shown to be inaccurate. Images reconstructed from complex data and sensitivity matrices have shown a far better accuracy. If *a-priori* information about the region to be imaged is considered, the degree of accuracy in reconstructed conductivity distribution increases.

Recognising the fact that complex boundary voltages may perhaps be obtained by the use of improved instrumentation, the calculation of a complex sensitivity matrix for any given frequency will also be needed. A simple analytical formulation for the calculation of complex sensitivity matrix has been presented. This calculation uses the commonly used real (only) sensitivity matrix,  $\mathbf{S}_{dc}$ , together with the reference uniform complex conductivity distribution (assuming that linearity holds).

Finally, it is known that biological tissue possesses a complex conductivity that varies with frequency. It has been shown that reconstructed images of this changing conductivity with frequency produce results that vary in a different manner to the actual variation with frequency. This difference in variation with frequency is present when complex data is used with or without the complex sensitivity matrices. However, the sensitivity matrices used here are the ones referred to in this work as uniform sensitivity matrices, where no *a-priori* information about the region being imaged is considered. These matrices are calculated on the assumption that for a uniform reference conductivity distribution, any change in conductivity seen will be small.

It is therefore concluded that to image varying conductivity within a region of interest with respect to frequency, to gain any accurate information about its frequency dependent behaviour, not only the complex components of measured data and sensitivity matrices are needed but almost certainly some *a-priori* information about the region being imaged is also necessary. This will improve the quality of the reconstructed images of internal conductivity distribution, as seen for the single frequency case in section 4.6.3, and hence allow a more accurate quantitative measurement of complex impedance.

## Chapter 6

### 6. Conclusions

#### 6.1 Introduction

In this work, a finite element modelling software package has been identified and used to solve the forward problem in electrical impedance tomography (EIT). The results from this numerical method have been used to investigate the behaviour of single and multi-frequency EIT. Limiting assumptions have been investigated in image reconstruction and an iterative algorithm based on the sensitivity matrix and *a-priori* information has been proposed. The new proposed algorithm greatly improves quantitative accuracy of reconstructed images. Image reconstruction in multi-frequency EIT has also been investigated. It has been shown that not only is complex (real and imaginary) data required, but that some *a-priori* information about the region being imaged will be vital to produce accurate reconstruction.

#### 6.2 Summary of key results

In Chapter 2 the need for forward modelling in EIT was discussed together with modelling methods. The advantages of finite element modelling over other numerical as well as analytical methods were given together with the need for improvements in previous modelling techniques. Governing equations that accurately describe a multi-frequency EIT system were given, which allow for variation of measurement frequency, permeability, permittivity as well as conductivity.

From the many commercially available FEM software packages, five have been reviewed and all but one were found to be unsuitable for accurately modelling an EIT system. This software package, MEGA, solves the derived equations (equations 2.11 - 2.13 and 2.14) which allowed accurate modelling of conduction current, displacement current and if desired allowed for effects of eddy currents in a system to be considered.

In Chapter 3 the basic modelling steps in FEM were given, together with some initial results of measures of performance in EIT. This chapter highlighted the capability of

FEM in modelling the behaviour of an EIT system under various conditions. A new measure of visibility,  $G$ , (an RMS measure) was introduced and it was shown to have a more physically meaningful interpretation than the previously proposed measure of visibility  $Q$ . Visibility  $G$  shows that an insulator is more visible than a conductor of the same size but of reciprocal conductivity.

Eddy currents in an EIT system were, for the first time, modelled in addition to conduction currents with respect to various applied excitation frequencies in order to investigate the possible effect on the measured boundary voltages due to skin-effect within the regions being imaged. Because biological tissues have negligible magnetic properties (permeability), it was found that eddy currents can in fact be neglected in the modelling of a multi-frequency EIT system for biomedical applications. However, similar experiments allowing for displacement currents have shown that since biological tissues have a high relative permittivity, displacement currents can not be neglected in the modelling of multi-frequency EIT.

In Chapter 4 the concept, needs and benefits of image reconstruction were given. Of the many methods available, the single pass sensitivity algorithm was used since it is a widely used method of image reconstruction in EIT and is ideal for differential imaging. Images reconstructed using this technique also showed the ill-conditioned problem faced in EIT. The assumption of linearity taken by most researchers for the purpose of image reconstruction was investigated and shown to be invalid. Images reconstructed using this method certainly look visually acceptable, but their quantitative information was found to be highly inaccurate. An iterative algorithm based on the sensitivity matrix was presented which incorporates *a-priori* information in the form of geometrical knowledge about the internal conductivity distribution of the region being imaged. This method showed an improvement in the quantitative information extractable from the reconstructed images of conductivity distribution.

In Chapter 5 reconstructed images of the complex (real and imaginary) conductivity over a range of frequencies were presented. It was shown that to accurately reconstruct images at various frequencies, not only are the real and imaginary boundary voltages

required but also a complex (real and imaginary) sensitivity matrix at each measurement frequency is needed.

It was shown that uniform complex sensitivity matrices (calculated assuming linearity) can be calculated from a uniform real (only) sensitivity. Finally, it was demonstrated, for the first time, that using complex boundary voltages and uniform complex sensitivity matrices does not provide accurate results for comparisons with a Cole-Cole model of biological tissue.

### **6.3 Suggestions for future developments**

A number of suggestions for future work in numerical modelling and image reconstruction in EIT can be identified. These will in turn assist in understanding the overall behaviour of an EIT system and provide new methods in making EIT more successful in clinical applications.

In general, EIT is a 3 dimensional (3D) imaging method. It has been demonstrated that 3D modelling of EIT is possible. To allow more accurate modelling of EIT, it is therefore suggested that further numerical modelling of the forward problem in EIT should concentrate its work on 3D analysis. This will show the effect of objects which are not in the imaging plane and hence possibly provide a method to incorporate their presence. The proposed iterative algorithm which incorporates *a-priori* information about the region being imaged has been developed for the 2D problem. It has been proposed that this method will also be valid for 3D image reconstruction. This assumption can further be investigated by 3D modelling.

Image reconstruction in multi-frequency EIT has been demonstrated in chapter 5. It has been suggested that to accurately reconstruct images from multi-frequency measurements not only is a complex sensitivity matrix for each frequency vital but also *a-priori* information about the region being imaged will be needed. *A-priori* information was shown to be useful in single-frequency EIT and this approach will need further investigation in multi-frequency EIT.

Although the reconstruction algorithms suggested in this work have only used modelled data, it will be necessary to test the accuracy with actual measured data from human volunteers and patients. This will allow for the necessary further investigation of the accuracy of the methods and to explore how the proposed algorithm will cope with measurement errors.

## **6.4 Conclusions**

EIT has been under development for over a decade. Its application in a clinical environment has yet to be justified and made widespread. Numerical modelling has shown its benefits to understanding the underlying behaviour of an EIT system and shown its application in image reconstruction in EIT. A proposed image reconstruction algorithm has suggested that EIT may be beneficial in accurately imaging the internal conductivity distribution within a region of interest, providing that *a-prior* information about the region is also taken into account. Numerical modelling has further shown that for accurate quantitative image reconstruction in multi-frequency EIT the imaginary part of the measured data is crucial as is the use of the complex (real and imaginary) sensitivity matrix at each measurement frequency. This finding should direct any future instrumentation work in EIT towards improving systems that can accurately measure the quadrature component of the boundary voltages as well as the magnitude of the in-phase component.

## Appendix A

In section 2.4 Maxwell's equations were presented and from those the three fundamental equations describing an EIT system were presented. In this appendix, those fundamental equations will be derived.

### A1. Full 3D electromagnetic field eddy current problem

In this section the basic defining equations, uniqueness conditions and the preliminary steps that define the equations 2.11 and 2.12 are shown.

Since field vector  $\mathbf{B}$  satisfies a zero divergence condition

$$\nabla \cdot \mathbf{B} = 0 \tag{2.8}$$

and since the 'divergence' of the 'curl' of any vector is equal to zero, equation (2.8) can be expressed in terms of a vector potential  $\mathbf{A}$  as:

$$\mathbf{B} = \nabla \times \mathbf{A} \tag{A.1}$$

and then from equation (2.6)

$$\nabla \times \mathbf{E} = -\frac{\partial \mathbf{B}}{\partial t} \tag{2.6}$$

and equation (A.1) it follows that

$$(\nabla \times \mathbf{E}) + \left( \nabla \times \frac{\partial \mathbf{A}}{\partial t} \right) = \nabla \times \left( \mathbf{E} + \frac{\partial \mathbf{A}}{\partial t} \right) = 0 \tag{A.2}$$

Hence by integration of equation (A.2)

$$\mathbf{E} = -\left( \frac{\partial \mathbf{A}}{\partial t} + \nabla V \right) \tag{A.3}$$

where  $V$  is a scalar potential.

In equation (A.3), neither  $\mathbf{A}$  nor  $V$  is completely defined since the gradient of an arbitrary function can be added to  $\mathbf{A}$ , and the time derivative of the same function can

be subtracted from  $V$  without affecting the physical quantities  $\mathbf{E}$  and  $\mathbf{B}$ . Changes such as these to  $\mathbf{A}$  and  $V$  are known as gauge transformations and the uniqueness of any solution is usually ensured by specifying the divergence (or gauge) of  $\mathbf{A}$  together with the necessary boundary conditions. Thus in a region of interest, using the complete set of Maxwell's equations, the governing equation in terms of  $\mathbf{A}$  and  $V$  is given as:

$$\nabla \times \frac{1}{\mu} \nabla \times \mathbf{A} + (\sigma + j\omega\epsilon) \left( \frac{\partial \mathbf{A}}{\partial t} + \nabla V \right) = 0 \quad (\text{A.4})$$

where  $\mu$  and  $\epsilon$  are the absolute magnetic permeability and electric permittivity respectively.

And a further condition to be satisfied is the current continuity condition:

$$\nabla \cdot \left( \mathbf{J} + \frac{\partial \mathbf{D}}{\partial t} \right) = 0 \quad (\text{A.5})$$

which can be expressed as:

$$\nabla \cdot (\sigma + j\omega\epsilon) \left( \frac{\partial \mathbf{A}}{\partial t} + \nabla V \right) = 0 \quad (\text{2.12})$$

Next equation (A.4) needs to be gauged to ensure uniqueness to the solution. One method is to assign Coulomb gauge explicitly into equation (A.4). In this case Coulomb gauge is given by:

$$\nabla \cdot \mathbf{A} = 0 \quad (\text{A.6})$$

which is imposed directly into equation (A.4), which leads to:

$$\nabla \times \frac{1}{\mu} \nabla \times \mathbf{A} - \left\{ \nabla \frac{1}{\mu} \nabla \cdot \mathbf{A} \right\} + (\sigma + j\omega\epsilon) \left( \frac{\partial \mathbf{A}}{\partial t} + \nabla V \right) = 0 \quad (\text{2.11})$$

## **A2. Electric scalar formulation with no eddy currents**

There are classes of problems where both displacement currents and conduction currents are significant whilst eddy currents are not. In this case the governing equations for the region of interest can be derived.

From the current continuity equation:

$$\nabla \cdot ((\sigma + j\omega\epsilon)E + \frac{\partial D}{\partial t}) = 0 \quad (\text{A.7})$$

The electric field can be represented as

$$E = -\nabla V \quad (\text{A.8})$$

substituted into equation (A.7) to give:

$$\nabla \cdot ((\sigma + j\omega\epsilon)\nabla V + \epsilon \frac{\partial V}{\partial t}) = 0 \quad (2.14)$$

## Appendix B

### B1. Finite element modelling using MEGA: A brief guide

The software package used for finite element modelling of EIT in this thesis is MEGA, a software package supplied by the Electromagnetic Research Group of Bath University.

Each software package has its own unique modelling stages and user commands and in this appendix details will be provided for the user on how a typical model was constructed and used to obtain solutions to the problem. Users are however advised on referring to user manual and command reference booklet supplied by the software package.

The software is used under the X-windows of UNIX and is semi-menu driven. All commands are in UPPERCASE, and all input commands by the user will here be displayed as a **BOLD UPPERCASE COMMANDS**.

To initial the pre and post processor, use **VIEW DP**. The option DP indicated Double Precision being used for calculations.

The EIT model used is a circular phantom of radius 5 cm with 16 electrodes of 2 mm thickness, placed equidistant on the periphery of the circular model. A 2D model will be constructed for modelling of conduction and displacement currents only. Since the model is highly symmetrical, it is possible and easier to only build one part of the model and then use this part to copy and complete the whole of the circular model. Here, only one sixteenth of the model will be initial built.

By the use of **AE** (Arc Edit) command, construct a section of the circular phantom. Choosing the arcs to start from  $0.0^\circ$  to  $22.5^\circ$  and having arcs of radii of 5.2, 5.1, 5.0, 4.5, 4.0, 3.5, 3.0, 2.5, 2.0, 1.5, 1.0 and 0.5 m, the user should obtain the diagram shown in Figure B1. Note that initially the units are SI units and will be in meters. These will later be scaled to appropriate units.

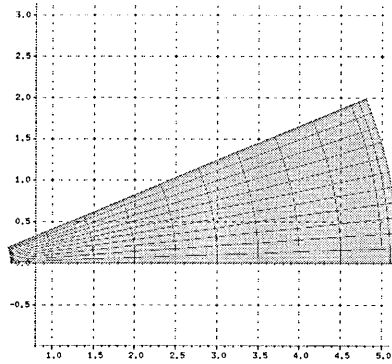


**Figure B1. Building one sixteenth of the model, with arcs of various radii.**

The central elements can then be constructed. Using **EN** (Edit Nodes) command, it is possible to edit nodes and add additional elements. By clicking the mouse on **K** (Key Node) nodes at co-ordinates defined by the user can be specified. Place a node at co-ordinate **0.0 0.0**. Then click on **S** (Super Element) to add a 3 sided region. Create a side from central co-ordinate **0.0 0.0**, to co-ordinate **0.5 0.0** and then stitch a side on the inner arc, and then create a final straight side back to central co-ordinate.

Using command **EE** (Edit Element) it is possible to edit elements. Elements on the two outer arcs of the arc need deleting to provide spacing between electrodes. Delete element by clicking on **0** and then clicking on elements as shown in figure B2.

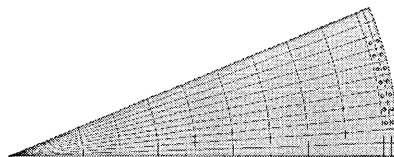


**Figure B2. Showing marked elements to provide spacing between electrodes.**

Now, one sixteenth part of the circular model is completed. It is now possible to select various regions and provide them with region id's to allow material property specification at a later stage. Still in the **EE** (Edit Element) menu, select **M** (Mark element) for marking elements. In the new displayed sub-menu, select **C** (Circle) to define a circle of radius **5.0 0.0** and a centre of **0.0 .0.0**. This will select all elements within this defined circle. On quitting this sub menu the user is prompted to input a region id. Chose **3**. This is the lowest region id number the user can have. Then using

**M** (Mark element) again, but this time use **P** (Point with cursor) command to click on the electrode elements, mark all electrode elements. On quitting the sub menu once again, the user is prompted for a region id and region id **4** should be used.

Now the defined segment will have coloured elements indicating the region id they possess, Figure B3.

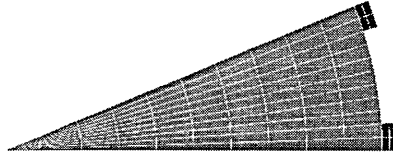


**Figure B3. Completed one sixteenth section of circular model after region id specification.**

The segment can now be copied and flipped a number of times to give a full circular model. Using **EN** (Edit Nodes) command, chose **F** (Copy utility) to copy elements, marking all elements and flip about a line. The user is prompted to give co-ordinates of a line about which the copied elements can be flipped. If instead of numbers for co-ordinates, **N** (cursor input) is typed, the user can click on a chosen co-ordinate instead of giving numerical co-ordinates. Click on bottom left hand corner for first co-ordinate, and then the top right hand corner for the second, to give one eighth of the model, Figure B4.

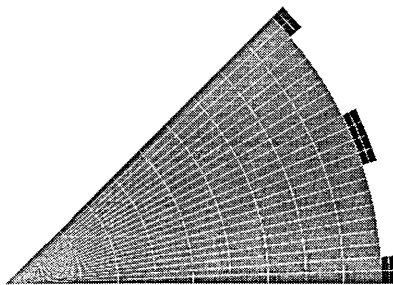


**Figure B4 After the first copy, one eighth of model is complete.**

Repeat as above again, to copy all elements and flip along the line defined by bottom left hand and top right hand corner, to give one quarter of the model, Figure B5.

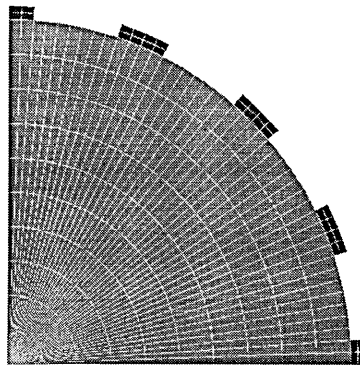


**Figure B5 One quarter of model completed.**

Once again repeat, but now flip along line defined by bottom left corner, and top left corner, to give half of model, Figure B6,

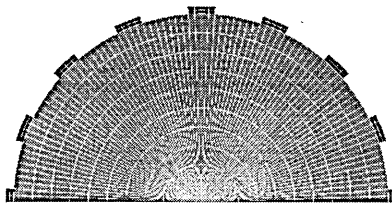


**Figure B6 One half of the model completed.**

and finally copy and flip along line from bottom left corner to bottom right corner to give a complete model, Figure B7.

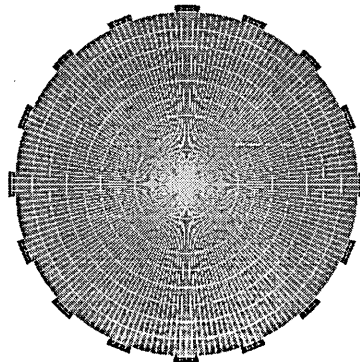


**Figure B7 The complete model.**

At any stage if the user needs to view the complete model, click on **W** (Window) at the bottom of the menu to re-size window, and select default value **D** (Default). On quitting

the user is prompted to 'kill' (delete) all duplicate nodes. All duplicate nodes **MUST** be killed.

Now since all dimensions are in metres, the model can be scaled down to user defined units. Type **MN** (Move Nodes) to move nodes. Then select all nodes by typing **NM** (Node Mark) and clicking on **all nodes**. Then **Q** (Quit) to return to first menu, and type **GT** (General Transformation) for general transformation, and then **SC** (Scaling) for scaling. The user can now scale all marked nodes. Use **0.01 0.01 0.01** to scale nodes down by a factor of 0.01 in x, y, and z direction. On quitting for this menu, type **Q** (Quit) and then display elements by selecting window **SW** (Set Window) and choosing default value **D** (Default). Then type **DG** (Draw Grid) to draw a grid, and the grid values are displayed as metres.

The user now needs to specify problem type and material property. Use **SP** (Set Problem) to set problem type. For the 2D conduction and displacement current problem, use **CD** (Conduction Displacement), then on quitting the user is prompted to define material name and property, conductivity and permittivity. It is suggested that as a first model, chose simple values as  $1 \text{ Sm}^{-1}$  and relative permittivity of 1.0 for uniform region, and  $10000 \text{ Sm}^{-1}$  and the default value of permittivity for non-permittive material.

Next, define the boundary conditions using **EB** (Edit Boundary). To set a boundary attribute to a node or nodes type **SA** (Set Attributes). The variable that needs assigning is **V** (Voltage) and the user can accept the default id number for this variable for the boundary. As each material region has a region id number as well as name, all boundary conditions also have an id number for identification. To assign a constant current, the variable type to chose is **TR** (Constant Current) and the value of which is suggested at this stage as **-1.0e-3 0.0**. The negative value assigns a current flowing into the face of the electrode. Chose command **P** (point) to point and click on the central 3 nodes of one electrode, Figure B8.

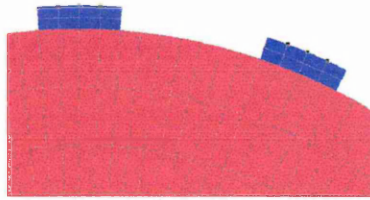


**Figure B8 Assigning boundary voltages on electrodes.**

Next to set the ground electrode, repeat all above, but now assigning a fixed variable, **FX** (Fixed) instead of the previous **TR** on the face of an adjacent electrode, Figure B8.

Now the model is ready to be saved and solved. To save model use **WR** (Write) command.

To solve model the user must exit from MEGA software, and submit the file to be solved using **SUBMIT** command. The user is then prompted to input file name. It is essential that the user specifies for the solver to use **DP** (Double precision) when prompted.

Once solved enter pre-post processor by typing **VIEW DP**. To read model, type **RE** (Read) and to read answer to a solved model type **RA** (Read Answer).

To View potential distribution, type **CC** (Calculate Contour) and then **NV** (Nodal Variable). The user is prompted for various options, and should chose to look at **V** (Voltage), no subset of elements, both colour and line contours, 26 contour levels, and accept default calculated values. Then the user should type **DC** (Display Contour) to draw contours and **CK** (Colour Key) for a colour bar, Figure B9.

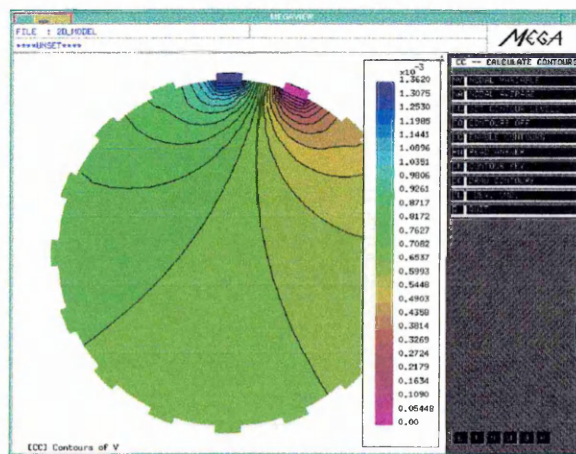


**Figure B9 Colour Contour of uniform model with colour key**

To plot boundary voltages, the user must define a surface on the outer most circumference of the model, that is, the electrode / phantom contact region. The command to use is **ES** (Edit surface) and the surface should be given a name, for example **Boundary**, and surface type should be accepted as a default **TEST**. Mark nodes on circumference by clicking on **Z** (Mark nodes on circumference) and define a circle by typing co-ordinates of **0.0 0.0** for centre and **5e-2 0.0** for radius. To display boundary voltages, first type **dv** (developers mode), and then **NI** (Nodal Information). Click on **M** (Mark Elements) and chose **A** (Angle) to give out readings as a function of angular distance. Then from menu chose **S** (Defined Surface) for defined surface and type the id for displayed surface name, chose **Q** (Quit) and when prompted type **V** (Voltage) for voltage. The user can then define real, or imaginary (when problem is ac). To display graph chose window **0**, and type yes to save graph in a user defined name. The graph is saved as an ASCII file with two columns, one co-ordinates of nodes on circumference, and the other voltage values.

The electric fields and current densities can be view and saved in an ASCII file using **GV** (Gaussian Vector). For ac problems, the electric field is best viewed and saved using command **GS** (Gaussian Scalar).

# Appendix C

## C1 List of all Matlab files

In this Appendix, a number of typical files used in Matlab for the calculation of the sensitivity matrices and image reconstruction is given.

### Proj.m

%This file reads the electric field for the 16 projections. The files that are read, are ASCII files named E-Field\_1, . . . , E-Field\_16. Each file is then assigned a variable name corresponding to the projection it %is from, i.e. projection 1, . . . , projection 16.

```
format long E
fid=fopen('E-Field_1.gv','r');
proj_1=fscanf(fid,'%f %f',[2 640]);
proj_1=proj_1';
fid=fopen('E-Field_2.gv','r');
proj_2=fscanf(fid,'%f %f',[2 640]);
proj_2=proj_2';
fid=fopen('E-Field_3.gv','r');
proj_3=fscanf(fid,'%f %f',[2 640]);
proj_3=proj_3';
fid=fopen('E-Field_4.gv','r');
proj_4=fscanf(fid,'%f %f',[2 640]);
proj_4=proj_4';
fid=fopen('E-Field_5.gv','r');
proj_5=fscanf(fid,'%f %f',[2 640]);
proj_5=proj_5';
fid=fopen('E-Field_6.gv','r');
proj_6=fscanf(fid,'%f %f',[2 640]);
proj_6=proj_6';
fid=fopen('E-Field_7.gv','r');
proj_7=fscanf(fid,'%f %f',[2 640]);
proj_7=proj_7';
fid=fopen('E-Field_8.gv','r');
proj_8=fscanf(fid,'%f %f',[2 640]);
proj_8=proj_8';
fid=fopen('E-Field_9.gv','r');
proj_9=fscanf(fid,'%f %f',[2 640]);
proj_9=proj_9';
fid=fopen('E-Field_10.gv','r');
proj_10=fscanf(fid,'%f %f',[2 640]);
proj_10=proj_10';
fid=fopen('E-Field_11.gv','r');
proj_11=fscanf(fid,'%f %f',[2 640]);
proj_11=proj_11';
fid=fopen('E-Field_12.gv','r');
proj_12=fscanf(fid,'%f %f',[2 640]);
proj_12=proj_12';
fid=fopen('E-Field_13.gv','r');
proj_13=fscanf(fid,'%f %f',[2 640]);
proj_13=proj_13';
fid=fopen('E-Field_14.gv','r');
proj_14=fscanf(fid,'%f %f',[2 640]);
proj_14=proj_14';
fid=fopen('E-Field_15.gv','r');
proj_15=fscanf(fid,'%f %f',[2 640]);
proj_15=proj_15';
fid=fopen('E-Field_16.gv','r');
proj_16=fscanf(fid,'%f %f',[2 640]);
proj_16=proj_16';
```

## Dot e.m

%This file, calculated the sensitivity coefficient for each pixel for every drive/recieve combination. It %uses the variables (electric fields) obtained from file proj.m and uses the DOT PRODUCT operator to %calculate the sensitivity matrix, saved as the variable S..

```
for n=1:640
D1R1(n)=dot((proj_1(n,:)),(proj_3(n,:)));
end
for n=1:640
D1R2(n)=dot((proj_1(n,:)),(proj_4(n,:)));
end
for n=1:640
D1R3(n)=dot((proj_1(n,:)),(proj_5(n,:)));
end
for n=1:640
D1R4(n)=dot((proj_1(n,:)),(proj_6(n,:)));
end
for n=1:640
D1R5(n)=dot((proj_1(n,:)),(proj_7(n,:)));
end
for n=1:640
D1R6(n)=dot((proj_1(n,:)),(proj_8(n,:)));
end
for n=1:640
D1R7(n)=dot((proj_1(n,:)),(proj_9(n,:)));
end
for n=1:640
D1R8(n)=dot((proj_1(n,:)),(proj_10(n,:)));
end
for n=1:640
D1R9(n)=dot((proj_1(n,:)),(proj_11(n,:)));
end
for n=1:640
D1R10(n)=dot((proj_1(n,:)),(proj_12(n,:)));
end
for n=1:640
D1R11(n)=dot((proj_1(n,:)),(proj_13(n,:)));
end
for n=1:640
D1R12(n)=dot((proj_1(n,:)),(proj_14(n,:)));
end
for n=1:640
D1R13(n)=dot((proj_1(n,:)),(proj_15(n,:)));
end
%      Drive two
for n=1:640
D2R1(n)=dot((proj_2(n,:)),(proj_4(n,:)));
end
for n=1:640
D2R2(n)=dot((proj_2(n,:)),(proj_5(n,:)));
end
for n=1:640
D2R3(n)=dot((proj_2(n,:)),(proj_6(n,:)));
end
for n=1:640
D2R4(n)=dot((proj_2(n,:)),(proj_7(n,:)));
end
for n=1:640
D2R5(n)=dot((proj_2(n,:)),(proj_8(n,:)));
end
for n=1:640
D2R6(n)=dot((proj_2(n,:)),(proj_9(n,:)));
end
for n=1:640
D2R7(n)=dot((proj_2(n,:)),(proj_10(n,:)));
end
for n=1:640
D2R8(n)=dot((proj_2(n,:)),(proj_11(n,:)));
end
```

```

for n=1:640
D2R9(n)=dot((proj_2(n,:)),(proj_12(n,:)));
end
for n=1:640
D2R10(n)=dot((proj_2(n,:)),(proj_13(n,:)));
end
for n=1:640
D2R11(n)=dot((proj_2(n,:)),(proj_14(n,:)));
end
for n=1:640
D2R12(n)=dot((proj_2(n,:)),(proj_15(n,:)));
end
for n=1:640
D2R13(n)=dot((proj_2(n,:)),(proj_16(n,:)));
end
%           Drive three
for n=1:640
D3R1(n)=dot((proj_3(n,:)),(proj_5(n,:)));
end
for n=1:640
D3R2(n)=dot((proj_3(n,:)),(proj_6(n,:)));
end
for n=1:640
D3R3(n)=dot((proj_3(n,:)),(proj_7(n,:)));
end
for n=1:640
D3R4(n)=dot((proj_3(n,:)),(proj_8(n,:)));
end
for n=1:640
D3R5(n)=dot((proj_3(n,:)),(proj_9(n,:)));
end
for n=1:640
D3R6(n)=dot((proj_3(n,:)),(proj_10(n,:)));
end
for n=1:640
D3R7(n)=dot((proj_3(n,:)),(proj_11(n,:)));
end
for n=1:640
D3R8(n)=dot((proj_3(n,:)),(proj_12(n,:)));
end
for n=1:640
D3R9(n)=dot((proj_3(n,:)),(proj_13(n,:)));
end
for n=1:640
D3R10(n)=dot((proj_3(n,:)),(proj_14(n,:)));
end
for n=1:640
D3R11(n)=dot((proj_3(n,:)),(proj_15(n,:)));
end
for n=1:640
D3R12(n)=dot((proj_3(n,:)),(proj_16(n,:)));
end
for n=1:640
D3R13(n)=dot((proj_3(n,:)),(proj_1(n,:)));
end
%           Drive four
for n=1:640
D4R1(n)=dot((proj_4(n,:)),(proj_6(n,:)));
end
for n=1:640
D4R2(n)=dot((proj_4(n,:)),(proj_7(n,:)));
end
for n=1:640
D4R3(n)=dot((proj_4(n,:)),(proj_8(n,:)));
end
for n=1:640
D4R4(n)=dot((proj_4(n,:)),(proj_9(n,:)));
end
for n=1:640
D4R5(n)=dot((proj_4(n,:)),(proj_10(n,:)));

```

```

end
for n=1:640
D4R6(n)=dot((proj_4(n,:)),(proj_11(n,:)));
end
for n=1:640
D4R7(n)=dot((proj_4(n,:)),(proj_12(n,:)));
end
for n=1:640
D4R8(n)=dot((proj_4(n,:)),(proj_13(n,:)));
end
for n=1:640
D4R9(n)=dot((proj_4(n,:)),(proj_14(n,:)));
end
for n=1:640
D4R10(n)=dot((proj_4(n,:)),(proj_15(n,:)));
end
for n=1:640
D4R11(n)=dot((proj_4(n,:)),(proj_16(n,:)));
end
for n=1:640
D4R12(n)=dot((proj_4(n,:)),(proj_1(n,:)));
end
for n=1:640
D4R13(n)=dot((proj_4(n,:)),(proj_2(n,:)));
end
%           Drive five
for n=1:640
D5R1(n)=dot((proj_5(n,:)),(proj_7(n,:)));
end
for n=1:640
D5R2(n)=dot((proj_5(n,:)),(proj_8(n,:)));
end
for n=1:640
D5R3(n)=dot((proj_5(n,:)),(proj_9(n,:)));
end
for n=1:640
D5R4(n)=dot((proj_5(n,:)),(proj_10(n,:)));
end
for n=1:640
D5R5(n)=dot((proj_5(n,:)),(proj_11(n,:)));
end
for n=1:640
D5R6(n)=dot((proj_5(n,:)),(proj_12(n,:)));
end
for n=1:640
D5R7(n)=dot((proj_5(n,:)),(proj_13(n,:)));
end
for n=1:640
D5R8(n)=dot((proj_5(n,:)),(proj_14(n,:)));
end
for n=1:640
D5R9(n)=dot((proj_5(n,:)),(proj_15(n,:)));
end
for n=1:640
D5R10(n)=dot((proj_5(n,:)),(proj_16(n,:)));
end
for n=1:640
D5R11(n)=dot((proj_5(n,:)),(proj_1(n,:)));
end
for n=1:640
D5R12(n)=dot((proj_5(n,:)),(proj_2(n,:)));
end
for n=1:640
D5R13(n)=dot((proj_5(n,:)),(proj_3(n,:)));
end
%           Drive six
for n=1:640
D6R1(n)=dot((proj_6(n,:)),(proj_8(n,:)));
end
for n=1:640

```

```

D6R2(n)=dot((proj_6(n,:)),(proj_9(n,:)));
end
for n=1:640
D6R3(n)=dot((proj_6(n,:)),(proj_10(n,:)));
end
for n=1:640
D6R4(n)=dot((proj_6(n,:)),(proj_11(n,:)));
end
for n=1:640
D6R5(n)=dot((proj_6(n,:)),(proj_12(n,:)));
end
for n=1:640
D6R6(n)=dot((proj_6(n,:)),(proj_13(n,:)));
end
for n=1:640
D6R7(n)=dot((proj_6(n,:)),(proj_14(n,:)));
end
for n=1:640
D6R8(n)=dot((proj_6(n,:)),(proj_15(n,:)));
end
for n=1:640
D6R9(n)=dot((proj_6(n,:)),(proj_16(n,:)));
end
for n=1:640
D6R10(n)=dot((proj_6(n,:)),(proj_1(n,:)));
end
for n=1:640
D6R11(n)=dot((proj_6(n,:)),(proj_2(n,:)));
end
for n=1:640
D6R12(n)=dot((proj_6(n,:)),(proj_3(n,:)));
end
for n=1:640
D6R13(n)=dot((proj_6(n,:)),(proj_4(n,:)));
end
% Drive seven
for n=1:640
D7R1(n)=dot((proj_7(n,:)),(proj_9(n,:)));
end
for n=1:640
D7R2(n)=dot((proj_7(n,:)),(proj_10(n,:)));
end
for n=1:640
D7R3(n)=dot((proj_7(n,:)),(proj_11(n,:)));
end
for n=1:640
D7R4(n)=dot((proj_7(n,:)),(proj_12(n,:)));
end
for n=1:640
D7R5(n)=dot((proj_7(n,:)),(proj_13(n,:)));
end
for n=1:640
D7R6(n)=dot((proj_7(n,:)),(proj_14(n,:)));
end
for n=1:640
D7R7(n)=dot((proj_7(n,:)),(proj_15(n,:)));
end
for n=1:640
D7R8(n)=dot((proj_7(n,:)),(proj_16(n,:)));
end
for n=1:640
D7R9(n)=dot((proj_7(n,:)),(proj_1(n,:)));
end
for n=1:640
D7R10(n)=dot((proj_7(n,:)),(proj_2(n,:)));
end
for n=1:640
D7R11(n)=dot((proj_7(n,:)),(proj_3(n,:)));
end
for n=1:640

```

```

D7R12(n)=dot((proj_7(n,:),(proj_4(n,:)));
end
for n=1:640
D7R13(n)=dot((proj_7(n,:),(proj_5(n,:)));
end
%           Drive eight
for n=1:640
D8R1(n)=dot((proj_8(n,:),(proj_10(n,:)));
end
for n=1:640
D8R2(n)=dot((proj_8(n,:),(proj_11(n,:)));
end
for n=1:640
D8R3(n)=dot((proj_8(n,:),(proj_12(n,:)));
end
for n=1:640
D8R4(n)=dot((proj_8(n,:),(proj_13(n,:)));
end
for n=1:640
D8R5(n)=dot((proj_8(n,:),(proj_14(n,:)));
end
for n=1:640
D8R6(n)=dot((proj_8(n,:),(proj_15(n,:)));
end
for n=1:640
D8R7(n)=dot((proj_8(n,:),(proj_16(n,:)));
end
for n=1:640
D8R8(n)=dot((proj_8(n,:),(proj_1(n,:)));
end
for n=1:640
D8R9(n)=dot((proj_8(n,:),(proj_2(n,:)));
end
for n=1:640
D8R10(n)=dot((proj_8(n,:),(proj_3(n,:)));
end
for n=1:640
D8R11(n)=dot((proj_8(n,:),(proj_4(n,:)));
end
for n=1:640
D8R12(n)=dot((proj_8(n,:),(proj_5(n,:)));
end
for n=1:640
D8R13(n)=dot((proj_8(n,:),(proj_6(n,:)));
end
%           Drive nine
for n=1:640
D9R1(n)=dot((proj_9(n,:),(proj_11(n,:)));
end
for n=1:640
D9R2(n)=dot((proj_9(n,:),(proj_12(n,:)));
end
for n=1:640
D9R3(n)=dot((proj_9(n,:),(proj_13(n,:)));
end
for n=1:640
D9R4(n)=dot((proj_9(n,:),(proj_14(n,:)));
end
for n=1:640
D9R5(n)=dot((proj_9(n,:),(proj_15(n,:)));
end
for n=1:640
D9R6(n)=dot((proj_9(n,:),(proj_16(n,:)));
end
for n=1:640
D9R7(n)=dot((proj_9(n,:),(proj_1(n,:)));
end
for n=1:640
D9R8(n)=dot((proj_9(n,:),(proj_2(n,:)));
end

```

```

for n=1:640
D9R9(n)=dot((proj_9(n,:)),(proj_3(n,:)));
end
for n=1:640
D9R10(n)=dot((proj_9(n,:)),(proj_4(n,:)));
end
for n=1:640
D9R11(n)=dot((proj_9(n,:)),(proj_5(n,:)));
end
for n=1:640
D9R12(n)=dot((proj_9(n,:)),(proj_6(n,:)));
end
for n=1:640
D9R13(n)=dot((proj_9(n,:)),(proj_7(n,:)));
end
%           Drive ten
for n=1:640
D10R1(n)=dot((proj_10(n,:)),(proj_12(n,:)));
end
for n=1:640
D10R2(n)=dot((proj_10(n,:)),(proj_13(n,:)));
end
for n=1:640
D10R3(n)=dot((proj_10(n,:)),(proj_14(n,:)));
end
for n=1:640
D10R4(n)=dot((proj_10(n,:)),(proj_15(n,:)));
end
for n=1:640
D10R5(n)=dot((proj_10(n,:)),(proj_16(n,:)));
end
for n=1:640
D10R6(n)=dot((proj_10(n,:)),(proj_1(n,:)));
end
for n=1:640
D10R7(n)=dot((proj_10(n,:)),(proj_2(n,:)));
end
for n=1:640
D10R8(n)=dot((proj_10(n,:)),(proj_3(n,:)));
end
for n=1:640
D10R9(n)=dot((proj_10(n,:)),(proj_4(n,:)));
end
for n=1:640
D10R10(n)=dot((proj_10(n,:)),(proj_5(n,:)));
end
for n=1:640
D10R11(n)=dot((proj_10(n,:)),(proj_6(n,:)));
end
for n=1:640
D10R12(n)=dot((proj_10(n,:)),(proj_7(n,:)));
end
for n=1:640
D10R13(n)=dot((proj_10(n,:)),(proj_8(n,:)));
end
%           Drive eleven
for n=1:640
D11R1(n)=dot((proj_11(n,:)),(proj_13(n,:)));
end
for n=1:640
D11R2(n)=dot((proj_11(n,:)),(proj_14(n,:)));
end
for n=1:640
D11R3(n)=dot((proj_11(n,:)),(proj_15(n,:)));
end
for n=1:640
D11R4(n)=dot((proj_11(n,:)),(proj_16(n,:)));
end
for n=1:640
D11R5(n)=dot((proj_11(n,:)),(proj_1(n,:)));

```

```

end
for n=1:640
D11R6(n)=dot((proj_11(n,:)),(proj_2(n,:)));
end
for n=1:640
D11R7(n)=dot((proj_11(n,:)),(proj_3(n,:)));
end
for n=1:640
D11R8(n)=dot((proj_11(n,:)),(proj_4(n,:)));
end
for n=1:640
D11R9(n)=dot((proj_11(n,:)),(proj_5(n,:)));
end
for n=1:640
D11R10(n)=dot((proj_11(n,:)),(proj_6(n,:)));
end
for n=1:640
D11R11(n)=dot((proj_11(n,:)),(proj_7(n,:)));
end
for n=1:640
D11R12(n)=dot((proj_11(n,:)),(proj_8(n,:)));
end
for n=1:640
D11R13(n)=dot((proj_11(n,:)),(proj_9(n,:)));
end
%           Drive twelve
for n=1:640
D12R1(n)=dot((proj_12(n,:)),(proj_14(n,:)));
end
for n=1:640
D12R2(n)=dot((proj_12(n,:)),(proj_15(n,:)));
end
for n=1:640
D12R3(n)=dot((proj_12(n,:)),(proj_16(n,:)));
end
for n=1:640
D12R4(n)=dot((proj_12(n,:)),(proj_1(n,:)));
end
for n=1:640
D12R5(n)=dot((proj_12(n,:)),(proj_2(n,:)));
end
for n=1:640
D12R6(n)=dot((proj_12(n,:)),(proj_3(n,:)));
end
for n=1:640
D12R7(n)=dot((proj_12(n,:)),(proj_4(n,:)));
end
for n=1:640
D12R8(n)=dot((proj_12(n,:)),(proj_5(n,:)));
end
for n=1:640
D12R9(n)=dot((proj_12(n,:)),(proj_6(n,:)));
end
for n=1:640
D12R10(n)=dot((proj_12(n,:)),(proj_7(n,:)));
end
for n=1:640
D12R11(n)=dot((proj_12(n,:)),(proj_8(n,:)));
end
for n=1:640
D12R12(n)=dot((proj_12(n,:)),(proj_9(n,:)));
end
for n=1:640
D12R13(n)=dot((proj_12(n,:)),(proj_10(n,:)));
end
%           Drive thirteen
for n=1:640
D13R1(n)=dot((proj_13(n,:)),(proj_15(n,:)));
end
for n=1:640

```

```

D13R2(n)=dot((proj_13(n,:)),(proj_16(n,:)));
end
for n=1:640
D13R3(n)=dot((proj_13(n,:)),(proj_1(n,:)));
end
for n=1:640
D13R4(n)=dot((proj_13(n,:)),(proj_2(n,:)));
end
for n=1:640
D13R5(n)=dot((proj_13(n,:)),(proj_3(n,:)));
end
for n=1:640
D13R6(n)=dot((proj_13(n,:)),(proj_4(n,:)));
end
for n=1:640
D13R7(n)=dot((proj_13(n,:)),(proj_5(n,:)));
end
for n=1:640
D13R8(n)=dot((proj_13(n,:)),(proj_6(n,:)));
end
for n=1:640
D13R9(n)=dot((proj_13(n,:)),(proj_7(n,:)));
end
for n=1:640
D13R10(n)=dot((proj_13(n,:)),(proj_8(n,:)));
end
for n=1:640
D13R11(n)=dot((proj_13(n,:)),(proj_9(n,:)));
end
for n=1:640
D13R12(n)=dot((proj_13(n,:)),(proj_10(n,:)));
end
for n=1:640
D13R13(n)=dot((proj_13(n,:)),(proj_11(n,:)));
end
%      Drive fourteen
for n=1:640
D14R1(n)=dot((proj_14(n,:)),(proj_16(n,:)));
end
for n=1:640
D14R2(n)=dot((proj_14(n,:)),(proj_1(n,:)));
end
for n=1:640
D14R3(n)=dot((proj_14(n,:)),(proj_2(n,:)));
end
for n=1:640
D14R4(n)=dot((proj_14(n,:)),(proj_3(n,:)));
end
for n=1:640
D14R5(n)=dot((proj_14(n,:)),(proj_4(n,:)));
end
for n=1:640
D14R6(n)=dot((proj_14(n,:)),(proj_5(n,:)));
end
for n=1:640
D14R7(n)=dot((proj_14(n,:)),(proj_6(n,:)));
end
for n=1:640
D14R8(n)=dot((proj_14(n,:)),(proj_7(n,:)));
end
for n=1:640
D14R9(n)=dot((proj_14(n,:)),(proj_8(n,:)));
end
for n=1:640
D14R10(n)=dot((proj_14(n,:)),(proj_9(n,:)));
end
for n=1:640
D14R11(n)=dot((proj_14(n,:)),(proj_10(n,:)));
end
for n=1:640

```

```

D14R12(n)=dot((proj_14(n,:)),(proj_11(n,:)));
end
for n=1:640
D14R13(n)=dot((proj_14(n,:)),(proj_12(n,:)));
end
%           Drive fifteen
for n=1:640
D15R1(n)=dot((proj_15(n,:)),(proj_1(n,:)));
end
for n=1:640
D15R2(n)=dot((proj_15(n,:)),(proj_2(n,:)));
end
for n=1:640
D15R3(n)=dot((proj_15(n,:)),(proj_3(n,:)));
end
for n=1:640
D15R4(n)=dot((proj_15(n,:)),(proj_4(n,:)));
end
for n=1:640
D15R5(n)=dot((proj_15(n,:)),(proj_5(n,:)));
end
for n=1:640
D15R6(n)=dot((proj_15(n,:)),(proj_6(n,:)));
end
for n=1:640
D15R7(n)=dot((proj_15(n,:)),(proj_7(n,:)));
end
for n=1:640
D15R8(n)=dot((proj_15(n,:)),(proj_8(n,:)));
end
for n=1:640
D15R9(n)=dot((proj_15(n,:)),(proj_9(n,:)));
end
for n=1:640
D15R10(n)=dot((proj_15(n,:)),(proj_10(n,:)));
end
for n=1:640
D15R11(n)=dot((proj_15(n,:)),(proj_11(n,:)));
end
for n=1:640
D15R12(n)=dot((proj_15(n,:)),(proj_12(n,:)));
end
for n=1:640
D15R13(n)=dot((proj_15(n,:)),(proj_13(n,:)));
end
%           Drive sixteen
for n=1:640
D16R1(n)=dot((proj_16(n,:)),(proj_2(n,:)));
end
for n=1:640
D16R2(n)=dot((proj_16(n,:)),(proj_3(n,:)));
end
for n=1:640
D16R3(n)=dot((proj_16(n,:)),(proj_4(n,:)));
end
for n=1:640
D16R4(n)=dot((proj_16(n,:)),(proj_5(n,:)));
end
for n=1:640
D16R5(n)=dot((proj_16(n,:)),(proj_6(n,:)));
end
for n=1:640
D16R6(n)=dot((proj_16(n,:)),(proj_7(n,:)));
end
for n=1:640
D16R7(n)=dot((proj_16(n,:)),(proj_8(n,:)));
end
for n=1:640
D16R8(n)=dot((proj_16(n,:)),(proj_9(n,:)));
end

```

```

for n=1:640
D16R9(n)=dot((proj_16(n,:)),(proj_10(n,:)));
end
for n=1:640
D16R10(n)=dot((proj_16(n,:)),(proj_11(n,:)));
end
for n=1:640
D16R11(n)=dot((proj_16(n,:)),(proj_12(n,:)));
end
for n=1:640
D16R12(n)=dot((proj_16(n,:)),(proj_13(n,:)));
end
for n=1:640
D16R13(n)=dot((proj_16(n,:)),(proj_14(n,:)));
end
%constructing S matrix from all unweighted sensitivity coefficient values for all pixels for all %drive/recieve electrodes.
S=[D1R1;D1R2;D1R3;D1R4;D1R5;D1R6;D1R7;D1R8;D1R9;D1R10;D1R11;D1R12;D1R13;D2R1;D2R2;D2R3;D2R4;D2R5;D2R6;D2R7;D2R8;D2R9;D2R10;D2R11;D2R12;D2R13;D3R1;D3R2;D3R3;D3R4;D3R5;D3R6;D3R7;D3R8;D3R9;D3R10;D3R11;D3R12;D3R13;D4R1;D4R2;D4R3;D4R4;D4R5;D4R6;D4R7;D4R8;D4R9;D4R10;D4R11;D4R12;D4R13;D5R1;D5R2;D5R3;D5R4;D5R5;D5R6;D5R7;D5R8;D5R9;D5R10;D5R11;D5R12;D5R13;D6R1;D6R2;D6R3;D6R4;D6R5;D6R6;D6R7;D6R8;D6R9;D6R10;D6R11;D6R12;D6R13;D7R1;D7R2;D7R3;D7R4;D7R5;D7R6;D7R7;D7R8;D7R9;D7R10;D7R11;D7R12;D7R13;D8R1;D8R2;D8R3;D8R4;D8R5;D8R6;D8R7;D8R8;D8R9;D8R10;D8R11;D8R12;D8R13;D9R1;D9R2;D9R3;D9R4;D9R5;D9R6;D9R7;D9R8;D9R9;D9R10;D9R11;D9R12;D9R13;D10R1;D10R2;D10R3;D10R4;D10R5;D10R6;D10R7;D10R8;D10R9;D10R10;D10R11;D10R12;D10R13;D11R1;D11R2;D11R3;D11R4;D11R5;D11R6;D11R7;D11R8;D11R9;D11R10;D11R11;D11R12;D11R13;D12R1;D12R2;D12R3;D12R4;D12R5;D12R6;D12R7;D12R8;D12R9;D12R10;D12R11;D12R12;D12R13;D13R1;D13R2;D13R3;D13R4;D13R5;D13R6;D13R7;D13R8;D13R9;D13R10;D13R11;D13R12;D13R13;D14R1;D14R2;D14R3;D14R4;D14R5;D14R6;D14R7;D14R8;D14R9;D14R10;D14R11;D14R12;D14R13;D15R1;D15R2;D15R3;D15R4;D15R5;D15R6;D15R7;D15R8;D15R9;D15R10;D15R11;D15R12;D15R13;D16R1;D16R2;D16R3;D16R4;D16R5;D16R6;D16R7;D16R8;D16R9;D16R10;D16R11;D16R12;D16R13];
S=S';
%Taking the mean for sensitivity coefficient for every three adjacent pixel.
S=reshape(S,[3 133120]);
S=mean(S);
S=reshape(S,[640 208]);
S=S';
%Multiplying by the area of each element to give sensitivity coefficient
ele_area=[0.232791e-4 0.232791e-4 0.232791e-4 0.232791e-4 0.208286e-4 0.208286e-4 0.208286e-4 0.208286e-4 0.183782e-4 0.183782e-4 0.183782e-4 0.183782e-4 0.159278e-4 0.159278e-4 0.159278e-4 0.159278e-4 0.134774e-4 0.134774e-4 0.134774e-4 0.134774e-4 0.110269e-4 0.110269e-4 0.110269e-4 0.110269e-4 0.857650e-5 0.857650e-5 0.857650e-5 0.857650e-5 0.612607e-5 0.612607e-5 0.612607e-5 0.612607e-5 0.367564e-5 0.367564e-5 0.367564e-5 0.367564e-5 0.122521e-5 0.122521e-5];
ele_area=ele_area';
ele_area=reshape(ele_area,1,40);
ele_area=[ele_area ele_area ele_area];
for i=1:208
S(i,:)=S(i,:).*ele_area(1,:);
end
%Saving sensitivity coefficient as matlab file S.mat
save S.mat S;

```

## Invsvd.m

```

%Calculates the inverse of the sensitivity matrix S, using singular value decomposition.
load S.mat
sts=S*S';
[U,K,L]=svd(sts);
K=diag(K);
K=1./K;
newK=zeros(1,640);
%setting the truncation level, in this case 50
for n=1:50
    newK(1,n)=K(1,n);
end
K=diag(newK,0);
invsts=(U*K*L)';
invs=invsts*S';
%saving the inverse as svdinv.mat
save svdinv.mat invs

```



## References:

Alder A, Guardo R, Berthiaume Y 1994 **Impedance imaging of lung ventilation: Do we need to account for chest expansion?** Proc. IEEE/EMBS 534-535

Ansoft Manuals **User's reference** *Maxwell's 3D field simulator*

Avis NJ, Barber DC 1995 **Incorporating a priori information into the Sheffield filtered backprojection algorithm** *Physiol. Meas.* **16** A111-122

Blad B 1994 **An electrical impedance tomography system for complex impedance imaging** *Innovation et technologie en biologie et medicine* pp 80-88

Barber DC 1990 **Image reconstruction in applied potential tomography-electrical impedance tomography** *University of Sheffield, Department of Medical Physics and Clinical Engineering, Internal Report*

Barber DC, Brown BH and Freeston IL 1983 **Imaging spatial distribution of resistivity using applied potential tomography** *Electronics letters* Vol 19 pp 933-935

Barber DC and Brown BH 1990 **Reconstruction of impedance images using filtered back-projection** *Electrical impedance tomography Proceeding of conference in Copenhagen*

Basarab-Horwath I, Piotrowski J and McEwan P M 1995 **Calculated measures of performance in electrical impedance tomography using a finite-element model** *Physiol. Meas.* Vol 16, pp 263-271

Basarab-Horwath I and Dehghani H 1998 **Computer modelling in electrical impedance tomography** *Nondestructive testing and evaluation Vol 14 No. 3* pp 163-172

Binns K J, Lawrenson P J and Trowbridge C W 1992 **The analytical and numerical solution of electric and magnetic fields** *John Wiley & Sons*

Blad B 1994 **An electrical impedance tomography system for complex impedance imaging** *Innovation et technologie en biologie et medicine Vol 15, No Special 1*

Bland DR 1961 **Solutions of Laplace's equations** *Routledge Kegan and Paul, London.*

Boone K, Barber D, and Brown B 1997 **Review. Imaging with electricity: Report on the European Concerted Action on Impedance Tomography** *Journal of Medical Engineering & Technology*, Volume 21, Number 6, pages 201-232

Brown BH 1990 **Overview of clinical application** *Electrical Impedance Tomography Proceeding of Conference in Copenhagen* pp 29-35

Brown BH and Barber DC 1984 **Applied potential tomography** *Journal of Phys E: Scientific Instruments* **17** PP 723-733 An introductory review of reconstruction: primarily concerned with linear techniques

Brown BH and Barber DC 1987 **Electrical impedance tomography: the construction and application to physiological measurement of electrical impedance changes** *Med. Prog. Tech.* **13** pp 69-75

Brown BH, Barber DC, Wang W, Lu L, Leathard AD, Smallwood RH, Wilson AJ. 1994a **High frequency EIT data collection and parametric imaging.** *Innovation et technologie en biologie et medecine* Vol 15, No Special 1

Brown B H, Barber D C, Wang W, Lu L, Leathard A D, Smallwood R H, Hampshire A R, Mackay R and Hatzigalanis K 1994b **Multi-frequency imaging and modelling of respiratory related electrical impedance changes** *Physiol. Meas.* Vol 15, pp A1-A12

Chauveau N, Ayeva B, Rigaud B and Morucci JP 1996 **A multifrequency serial EIT system** *Physiol. Meas.* **17** (Supple. 4A) pp A7-A23

Conway J, Hawley M, Mangnall YF, Amasha H and Van Roon GC 1992 **Experimental assessment of electrical impedance imaging for hyperthermia monitoring** *Clin. Phys. and Physiol. Meas.* **13** (Supple. A) pp185-190

Erol R A, Smallwood R H, Brown B H, Cherian P and Bardhan K D 1995 **Detecting oesophageal-related changes using electrical impedance tomography.** *Phys. Meas.* Vol 16 Supp 3A

Fricke H and Morse M 1926 **The electrical capacity of tumour of the breast** *J Canver Res.* **10** pp 340-376

Geddes LA and Baker LE 1989 **Principles of applied biomedical instrumentation** 3rd edn. (New York: John Wiley)

Geselowitz DB 1971 **An application of electrocardiographic lead theory to impedance plethysmography** *IEEE. Trans. Biomed. Eng. BME* **18** 38-41

Griffiths H 1995 **Tissue spectroscopy with Electrical Impedance Tomography: Computer simulation** *IEEE Transaction on biomedical Engineering* VOL. 42 No. 9

Hammond and Sykulski 1994 **Engineering electromagnetism; Physical process and computation** *Oxford University Press*

Hampshire AR, Smallwood RH, Brown BH and Primhak RA 1995 **Multifrequency and parametric EIT images of neonatal lungs** *Physiological measurements* **16** (Suppl. 3A) pp175-189

Harris ND, Suggett AJ, Barber DC and Brown BH 1987 **Applied potential tomography: a new technique for monitoring pulmonary function** *Clinical physics and Physiological Measurements* **9** (suppl. A) pp 79 - 85

Holder DS (Ed) 1993 **Clinical and Physiological applications of Electrical Impedance Tomography**, UCL Press

Holder DS and Temple AJ 1993 **Effectiveness of the Sheffield EIT system in distinguishing patients with pulmonary pathology from a series of normal subjects.** In DS Holder *Clinical and Physiological Applications of Electrical Impedance Tomography* (UCL Press, London)

Hua P and Woo EJ 1990 **Reconstruction algorithms in Electrical Impedance Tomography** (Ed. JG Webster) *The Adam Hilger Series on Biomedical Engineering*

Hughes TAT, Liu P, Griffiths H, Lawrie BW and Wiles CM 1994 **An analysis of studies comparing electrical impedance tomography with X-ray videofluoroscopy in assessment of swallowing** *Physiol. Meas.* **15** (suppl. 2A) pp 199-209

- Jossinet J and Risacher F 1996 **The variability of resistivity in human breast tissue** *Medical and Biological Engineering and Computing* **34** pp346-350
- Kanai H, Haemo M and Sakamoto K. 1987 **Electrical measurement of fluid distribution in legs and arms.** *Med Prog Technol.* Vol 12 159-170
- Kim D W 1994 **Calculation of blood volume change in impedance cardiology by a 3-D finite element thoracic model** *Annual international conference of the IEEE engineering in Medicine and Biology Society-Proceedings Vol. 16, pt. 2, pp 888-889*
- Kolehmainen V, Vauhkonen M, Karjalainen PA and Kaipio JP 1997 **Assessment of errors in static electrical impedance tomography with adjacent and trigonometric current patterns** *Clin. Phys. Physiol. Meas.* **18** 289-303
- Kotre CJ 1993 **Studies of image reconstruction methods for electrical impedance tomography** *PhD Thesis* University of Newcastle-upon-Tyne, United Kingdom
- Kotre CJ 1995 **Sub-surface electrical impedance imaging: measurement strategy, image reconstruction and *in-vivo* results** *Proceedings of the 9th meeting of the ICEBI Heidelberg* September 1995, (Heidelberg University Press, Heidelberg), pp 522-523
- Kytomaa H K and Weselake K L 1994 **Current distribution and finite element mesh selection for electrical impedance tomography** *Computational Mathematics* **15**, pp161-172
- Lin J, Jones O C, Ovacik L and Shu H 1994 **Finite element modelling of impedance imaging in liquid/vapour system** *AMD-Vol. 186, Inverse Problems in Mechanics*, pp 71-84
- Lu L, Brown BH, Barber DC and Leathard AD 1995 **A fast parametric modelling algorithm with the Powell method** *Physiol. Meas.* Vol **16** Suppl. 3A pp39-48
- McArdle FJ, Turley A, Hussain A, Hawley K and Brown BH 1993 **An *in-vivo* examination of cardiac impedance changes imaged by cardiosynchronous averaging** In DS Holder (ed.) **Clinical and Physiological applications of Electrical Impedance Tomography**, UCL Press

Mangnall YF, Baxter AJ, Avill R, Bird NC, Brown BH, Barber DC, Seagar AD, Johnson AG and Read NW 1987 **Applied potential tomography: a new non-invasive technique for assessing gastric function** *Clin. Phys. Physiol. Meas.* **8** (Suppl. A) pp119-129

Meaney P M and Moskowitz M J 1993 **Finite element methods in impedance tomography and microwave imaging** *Bioengineering, Proceedings of the Northeast Conference*, pp 25-27

Metherall P, Barber DC, Smallwood RH and Brown BH 1996 **Three-dimensional electrical impedance tomography** *Nature* Vol 380 pp 509-512

Menke W 1989 **Geophysical data analysis: discrete inverse theory**. International geophysics series Volume 45 Academic Press, INC.

Möller PH, Tranberg KG, Blad B, Henriksson PH, Lindberg L, Webber L and Persson BRRR 1993 **EIT for measurement of temperature distribution in laser thermotherapy** In DS Holder (ed.) **Clinical and Physiological applications of Electrical Impedance Tomography**, UCL Press

Murphy D, Burton P, Coombs R, Tarassenko L and Rolpfe P 1987 **Impedance imaging in the newborn** *Clin. Phys. Physiol. Meas.* **9** (Suppl. A) pp5-14

Newell JC, Gisser DG and Isaacson D 1988 **An electric current tomograph** *IEEE Trans. Biomed. Eng.* **35** pp828-833

Osycka M and Gersing E 1995 **Tissue impedance spectra and the appropriate frequencies for EIT** *Physiol. Meas.* Vol 16 Suppl. 3A ppA49-56

Paulson K, Breckon W and Pidcock M 1992 **Electrode modelling in electrical impedance tomography** *SIAM J. Appl. MATH.* Vol. 52, No. 4, pp 1012-1022

Press WH, Teukolsky SA, Vetterling WT and Flanner BP 1992 **Numerical Recipes in C: The art of Scientific Computing** Second Edition. Cambridge University Press

Rigaud B, Hamzaoui L, Frikha M, Chauveau N and Morucci J 1995 **In vitro tissue characterisation and modelling using electrical impedance measurements in 100 Hz - 10 MHz frequency range** *Physiol. Meas.* **16** (Suppl. 3A) ppA15- 28

Rigaud B, Leila Hamzaoui, Nicholas Chauveau, Michel Granie, Jean-Philippe Scotto Di Rinaldi and Jean-Pierre Morucci. 1994 **Tissue characterisation by impedance: a multifrequency approach.** *Physiol. Meas.* **15**, A13-A20.

Ruan W, Guardo R, Adler A and Savoie G 1994 **Finite Element Modelling of Impedance Imaging Using Induced Currents** *Annual international conference of the IEEE Engineering in Medicine and Biology Society - Proceedings, Vol. 16 pt.1, pp536-537*

Rui PJ, Rosell J, Lozano A and Pallas-Areny RA 1992a **Broad band system for multi-frequency static imaging in EIT** *Clin. Phys. Physiol. Meas.* **13** Suppl. A pp 61-66

Rui PJ, Rosell J and Pallas-Areny RA 1992b **In-vivo static imaging for the real and the reactive parts in electrical impedance tomography using multi-frequency techniques** *Proc 14th Annual Int. Conf. IEEE Eng. Med. Biol. Soc. (Paris 1992)* (New York : IEEE) pp1706-1707

Schwab HP 1957 **Electrical properties of tissue and cell suspensions** *Adv. Biol. Med. Phys.* **5** pp 147-209

Seagar AD 1983 **Probing with low frequency electric currents** *PhD thesis University of Canterbury New Zealand*

Shahidi A V, Guardo R and Savard P 1995 **Impedance Tomography: Computational Analysis Based on Finite Element Models of a Cylinder and a Human Thorax** *Annals of Biomedical Engineering, Vol. 23, pp 61-69*

Shalof AM 1997 **Multi-frequency electrical impedance tomography for medical diagnostic imaging** *PhD Thesis University of Sheffield United Kingdom*

Shaw GR, Goussard Y, Guardo R 1993 **Linearization of the forward problem in Electrical impedance tomography** *Proc. IEEE/EMBS* 82-83

Silvester P P and Ferrari R L 1994 **Finite elements for Electrical Engineers** 2nd Edition *Cambridge University Press*

Smallwood RH, Nour S, Mangnall YF and Smythe A 1993 **Impedance imaging and gastric motility** In DS Holder (ed.) **Clinical and Physiological applications of Electrical Impedance Tomography**, UCL Press

Smallwood RH, Mangnall YF and Leathard AD 1994 **Transport of gastric contents** *Physiol. Meas.* **15** (Suppl. 2A) pp175-188

Surowiec A, Stuchly SS and Swarup A 1988 **Dielectric properties of breast carcinoma and the surrounding tissues** *IEEE Trans Biomed Eng.* **BME-35** pp 257-262

Weast RC **Handbook of Chemistry and Physics** 69th edition 1988-1989 Chemical Rubber Publishing Company

Webster JG 1989 **Electrical Impedance Tomography** Bristol: Adam Hilger

Yorkey TJ 1986 **Comparing reconstruction methods for Electrical Impedance Tomography** *PhD Thesis University of Wisconsin at Madison, USA*

Zadehkoochak M, Blott BH, Hames TK and George RF 1991 **The spectral expansion of a head model in electrical impedance tomography** *Clin. Phys. Physiol. Meas.* **12** A101-105

Zadehkoochak M, Blott BH and Hames TK 1993 **Dependence of thorax imaging on the reconstruction route** **Clinical and Physiological Applications of Electrical Impedance Tomography** ed D Holder (London: UCL Press) pp79-83

Zhang Z and Griffiths 1990 **Dual frequency electrical impedance tomography of the forearm** *Proc. 3rd Eur. Community (COMAC-BME) Workshop on Electrical Impedance Tomography (Copenhagen, 1990) (Brussels: CEC)* pp256-262